N° d'ordre NNT : 2016LYSEC007 *Année 2016*
ED n° 162 Mécanique, Energétique, Génie Civil et Acoustique

THESE

UNIVERSITE DE LYON

opérée au sein de

l'Ecole Centrale de Lyon en cotutelle avec l'Université d'Etat de Moscou

pour obtenir le titre de DOCTEUR
Spécialité ACOUSTIQUE

par

Maria KARZOVA

Focalisation nonlinéaire et réflexion d'ondes de choc acoustiques : applications aux ultrasons médicaux et à l'aéroacoustique

Nonlinear focusing and reflection of shock acoustic waves: applications in medical ultrasound and aeroacoustics

Soutenue le **10/03/2016** devant la Commission d'Examen

Président :	M. Daniel JUVÉ	
Examinateurs :	M. Robin CLEVELAND	Rapporteur
	M. Vladimir PREOBRAZHENSKY	Rapporteur
	M. Sergey KULICHKOV	
	M. Oleg SAPOZHNIKOV	
	M. Philippe BLANC-BENON	Co-directeur de thèse
	Mme Vera KHOKHLOVA	Co-directrice de thèse

Laboratoire de Mécanique des Fluides et d'Acoustique, UMR CNRS 5509 – ECL *et* Département d'Acoustique,
Faculté de Physique, Université d'Etat de Moscou

Acknowledgements

This PhD thesis was performed in co-tutelle program between Physics Faculty of Moscow State University (Russia) and Département de Mécanique des Fluides et d'Acoustique in École Centrale de Lyon (France). I address all my sincerest thanks to the Embassy of France in Russia which allowed me to get a scholarship from the French Government and to fulfill this co-supervised scientific work.

I express my deepest gratitude to Daniel Juvé, Director of Centre Acoustique in ECL, who was the chair of the French jury. My gratitude also goes to Professor Vladimir Preobrazhensky (Ecole Centrale de Lille) and Professor Robin Cleveland (Oxford University) who agreed to be rapporteurs of this work and members of the jury.

I extend my warmest acknowledgments to my supervisors in co-tutelle Professor Vera Khokhlova (Moscow State University) and Professor Philippe Blanc-Benon (Ecole Centrale de Lyon). They have greatly contributed to this thesis by their advices, by their comments and their support. They were always available for discussions and they always helped me to find a solution of both scientific and everyday problems.

Special thanks to Petr Yuldashev, Edouard Salze, and Sébastien Ollivier for working together. They always helped me to resolve all my scientific questions and contributed a lot to performing aeroacoustic experiments. I'm grateful to Jean-Michel Perrin for his help with the fabrication of the experimental setup, to Thomas Castelain for his help with the adjustment of the optical system, and to Emmanuel Jondeau for his help with the experiment automatization. I also would like to thank all other members of acoustic team in Centre Acoustique for welcoming me to their team.

I would like to acknowledge Professor David Blackstock for helpful comments on results of this study.

I wish to express my most sincere gratitude and appreciation to all members of LIMU team in Moscow State University. They have always been a constant source of encouragement during my studies. My warmest thanks go to Professor Oleg Sapozhnikov for fruitful discussions both in science and life, to Professor Valeriy Andreev for his helpful comments, to Mikhail Averyanov and Olga Bessonova for their great help on the beginning stage of my work.

I also owe my sincere thanks to people from the Center for Industrial and Medical Ultrasound in Seattle (University of Washington, USA). It was a great pleasure and honor to work with CIMU team. Special thanks to Camilo Perez and Bryan Cunitz who measured acoustic fields of medical devices investigated in the fourth chapter of this thesis.

Finally, I would like to thank my family and my friends who always supported me and helped a lot in many aspects.

Abstract

Nonlinear focusing and reflection of weak acoustic shocks are important problems both in medical ultrasound and in aeroacoustics. In aeroacoustics, studies of propagation and reflection from surfaces of high-amplitude N-wave are relevant to the sonic boom problem associated with jet noise and with the development of civilian supersonic aircraft. In medical applications, high-intensity focused ultrasonic acoustic fields are widely used for therapy and noninvasive surgery. In this context, investigation of nonlinear acoustic fields and their characterization are of great importance.

In this thesis, the problem of characterization of high-amplitude N-wave generated in air by an electric spark was studied by two optical methods: a Schlieren method and a Mach-Zehnder interferometry method. Pressure waveforms were reconstructed either from the light intensity patterns in the recorded images or from the signal of photodiode using an Abel-type transform. The temporal resolution of reconstructed N-waves is six time better than that of the current state-of-the-art microphones. Thus, proposed optical methods are perspective tools for calibration of broadband acoustic microphones.

Developed optical techniques were applied to study the irregular reflection of spark-generated N-wave from the plane rigid surface in air. The Schlieren optical system was used for visualization of reflection pattern while the Mach-Zehnder interferometry method was applied to reconstruct waveforms. It was shown that irregular reflection occurs in a dynamical way and the length of the Mach stem increases with the propagation distance. Moreover, the Mach stem formation was observed above the surface where the reflected front shock of the N-wave intersects with the incident rear shock.

Characterization of nonlinear focused acoustic fields of medical devices is important to predict and to control induced biological effects in tissue. In the thesis, nonlinear propagation effects were analyzed for two modern medical devices: Duolith SD1 used in extracorporeal shock wave therapy and Philips C5-2 array probe used in preliminary experiments to move kidney stones by acoustic radiation force. A combined measurement and modeling approach was used for field characterization of devices: the boundary condition for the modeling was set to match low power measurements of the acoustic pressure field. In addition to characterization of real medical transducers, the theoretical investigation of nonlinear focusing of pulsed and periodic ultrasonic beams was performed for Gaussian and piston sources using the KZK equation. The saturation mechanisms were found different for cases of periodic and pulsed fields.

The reflection from the rigid boundary is considered in the thesis as a process similar to focusing of axially symmetric beam since the normal derivative of the pressure on the axis of focused beam and at the rigid surface in reflection wave pattern is equal to zero. Under this light, the formation of spatial structures similar to Mach stem was observed at the focal area of medical transducers and was described in numerical simulations within the framework of KZK equation.

Keywords: Nonlinear acoustics, N-waves, sonic boom, ultrasound, irregular reflection, Mach stem, nonlinear focusing, extracorporeal shock-wave therapy, propulsion of kidney stones.

Contents

Acknowledgements **i**

Abstract **iii**

Table of contents **1**

Introduction **5**

1 Measurements of N-waves in air using optical methods: a schlieren method and a Mach-Zehnder interferometry method **13**

1.1 Introduction 13
1.2 Experimental setup for optical measurements using a schlieren system 16
  1.2.1 Visualization of shock fronts using a schlieren optical method 16
  1.2.2 Experimental setup 16
1.3 Theoretical background: reconstruction of an acoustic waveform from a schlieren image 18
  1.3.1 Algorithm for reconstructing dimensionless pressure signatures of N-wave using an Abel-type inversion method 18
  1.3.2 Estimation of the peak positive pressures from the pulse elongation 19
  1.3.3 Conditions for the applicability of an algorithm 20
  1.3.4 Effect of the finite exposure time of the high-speed camera on the waveforms 21
1.4 Results of optical measurements performed by the schlieren system 22
  1.4.1 Dimensionless waveforms generated by the spark-source 22
  1.4.2 Reconstructed pressure signatures of N-wave 24
1.5 Experimental setup for optical measurements using a Mach-Zehnder interferometer 26
1.6 Measurement of acoustical waveforms using a Mach-Zehnder interferometer 28
  1.6.1 Optical signal formation 28
  1.6.2 Optical phase induced by the acoustic wave 29
1.7 Results of optical experiments performed by the Mach-Zehnder interferometer . . . 30
1.8 Comparison of optical methods: benefits and limitations for acoustic field reconstruction 32
1.9 Conclusions 33

2 Irregular reflection of an N-wave from a rigid surface in air 35
2.1 Introduction 35
2.1.1 Experiments of E. Mach demonstrated the irregular reflection of shocks . . 35
2.1.2 Physical causes of the Mach stem formation 35
2.1.3 A three-shock theory of von Neumann 36
2.1.4 A review of researches devoted to an irregular reflection of shocks 37
2.2 Types of reflection of weak acoustic shocks from a rigid surface 39
2.3 Visualization of dynamic irregular reflection of a spherical N-wave using an optical schlieren method 41
2.4 Measurement of irregular reflection patterns using the Mach-Zehnder interferometry method 44
2.5 Nonlinear interaction between the reflected front shock of an N-wave and its incident rear shock 47
2.6 Conclusions 47

3 Saturation mechanisms of shock wave parameters in pulsed and periodic high-intensity focused ultrasound beams 51
3.1 Introduction 51
3.1.1 The saturation effect in the fields of periodic waves: a literature review . . 52
3.1.2 The saturation effect in pulsed fields: a literature review 56
3.1.3 The structure of wavefronts at the focal area 60
3.2 Numerical model based on the KZK equation 61
3.3 Effect of a signal waveform on limiting values of shock wave parameters in nonlinear focused beams 64
3.4 Effect of source apodization on spatial structure and limiting values of shock wave parameters in nonlinear focused beams 71
3.5 Interaction of shock fronts in nonlinear focused acoustic beams 76
3.6 Conclusions 78

4 Characterization of nonlinear focused ultrasound fields of new medical devices 81
4.1 Introduction 81
4.2 Nonlinear effects in acoustic field of a clinical shock wave therapy device Duolith SD1 85
4.2.1 Measurements of pressure waveforms by a fiber optic probe hydrophone in water 85
4.2.2 Setting a boundary condition in a model using a method of an equivalent source 85
4.2.3 Numerical modeling based on the KZK equation 88
4.2.4 Comparison of data obtained in measurements and nonlinear modeling . . 88

4.3 Nonlinear effects in ultrasound field of rectangular focused diagnostic-type transducer Philips C5-2 . . . 92
4.3.1 Low power measurements on the axis and in the focal plane of the transducer 92
4.3.2 Setting the boundary condition for numerical model using low-amplitude measurements of pressure waveforms . . . 94
4.3.3 Transfer of the boundary condition from cylindrical surface to the plane . . 97
4.3.4 Numerical model based on Westervelt equation to calculate the three-dimensional nonlinear field . . . 97
4.3.5 Results on numerical simulations of nonlinear propagation, comparison with measurements . . . 98
4.4 Conclusions . . . 103

A Numerical calculation of the inverse Abel transform from the light intensity pattern in the schlieren image 105

B Synthèse des résultats 107

References 111

Introduction

Nonlinear focusing of weak acoustic shocks and their reflection from different types of surfaces are important problems in atmospheric and medical acoustics (Rudenko & Soluyan, 1977, Vinogradova *et al.*, 1979, Hill *et al.*, 2002, Bailey *et al.*, 2003, Rudenko, 1995, Rudenko & Sapozhnikov, 2004, Rudenko, 2007). In medicine, high-energy focused shock pulses have been widely used for about 30 years for the destruction of kidney stones in lithotripsy procedure (Hill *et al.*, 2002, Bailey *et al.*, 2003). Currently, there are new medical applications using focused waves: extracorporeal shock wave therapy, stopping internal bleeding (hemostasis), treatment of tumors by high intensity focused ultrasound (Hill *et al.*, 2002, Bailey *et al.*, 2003, Rudenko, 2007). All these medical applications use intensive (up to 30 kW/cm^2 in the focal area of the beam) acoustic waves propagating in nonlinear media. Induced biological effects are strongly dependent on the amplitude of the shock front.

In aeroacoustics, nonlinear propagation and reflection of shock pulses are of special attention due to development of new civil supersonic aircrafts (Plotkin, 2002). Shock pulses of sonic boom, or N-waves, generated by supersonic motion of the airplane propagate through the atmosphere to the ground, reflect from it and form an acoustic field with non-uniform pressure distribution close to the ground. High peak positive and negative levels of acoustic pressure may be harmful to people and buildings. Weak acoustic shocks are also generated by explosions, thunders, earthquakes, collapse of cavitation bubbles, high-power electrical discharges, and even by loud playing on some wind musical instruments (Rudenko, 1995, Hirschberg *et al.*, 1996). Despite the difference of practical applications, all these problems of medical and aeroacoustics have much in common in terms of theoretical models since they are related to the propagation, nonlinear focusing and reflection from the boundaries of shock acoustic waves.

Theoretical models describing these problems are quite complex, and analytical solutions can be obtained only within the framework of simplified approximations. Numerical simulations combined with laboratory experiments are used to describe in detail spatial and temporal structures of acoustic fields of shock waves. It should be noted that the presence of shock in waveform complicates significantly both numerical simulations and measurements. In simulations, the difficulties are more of a technical nature and are caused by the need to use small time and spatial steps of the numerical grid that requires using powerful supercomputers with large RAM size. Numerical modeling of practical applications related to nonlinear focusing and propagation of shock waves became possible only recently due to the rapid development of supercomputers and parallel computing methods.

Measurements of shock waves by acoustic methods are difficult from fundamental point of view. First of all, a bandwidth of even modern broadband devices (condenser microphones and fiber optic hydrophones) is limited at high frequencies that in many cases does not allow measure the shock rise time (Loubeau *et al.*, 2006). Second, waveforms measured by microphones are distorted by wave diffracting on a surface of the microphone (Yuldashev *et al.*, 2010b). Third, the high-precision measurements of reflection pattern are impossible using a microphone since it distorts the field structure by additional waves reflected from the microphone. Therefore, using alternative methods, such as optical, is of great interest to measure shock acoustic waves without distortion of their profiles and with high time resolution. In the thesis, optical measurements of an N-wave during its propagation and reflection from the surface were performed by means of two optical methods: the schlieren method (Karzova *et al.*, 2015d, Karzova *et al.*, 2015e) and the Mach-Zehnder interferometry method (Yuldashev *et al.*, 2015, Karzova *et al.*, 2015c, Ollivier *et al.*, 2015, Karzova *et al.*, 2015b).

The presence of the shock in acoustic waveform leads to several features in manifestation of nonlinear effects in the processes of the focusing and reflection. One of the classic effects caused by the presence of the shock is the formation of a three-wave structure near the reflecting surface at small angles of incidence (Ben-Dor, 1992). This phenomenon was first experimentally observed by Ernst Mach in 1868 (Mach, 1878) and has been studied well for strong step shocks when the acoustic Mach number is close to one. While step shocks are typical for aerodynamics, acoustic shock waves usually have more complicated waveforms of an N-wave (sonic boom waves), blast waves, sawtooth waves, and others. In addition, in nonlinear acoustics the values of acoustic Mach number are on the order of 10^{-3}, which is at least one order smaller than in aerodynamics. The reflection of such very weak, but nonetheless strongly nonlinear acoustic waves has not been studied to the same extent. In the thesis, nonlinear reflection of an N-wave generated by a spark source in air is studied experimentally (Karzova *et al.*, 2015e, Karzova *et al.*, 2015c, Karzova *et al.*, 2015b).

Another classic phenomenon caused by the presence of the shock is the saturation of acoustic field parameters in nonlinear focused fields (Rudenko, 1995). The limitation of the acoustic pressure at the focus need to be taken into account in medical applications using high-intensity focused beams. Existing analytical solutions for estimation the saturation level of the pressure amplitude at the focus were obtained in (Naugolnykh K.A. & Romanenko E.V., 1959, Ostrovskii & Sutin, 1975, Bacon, 1984, Shooter *et al.*, 1974, Musatov *et al.*, 1992) and could be used to predict peak positive pressure at the focus of medical transducers. However, these estimates have been obtained under different approximations and therefore are inaccurate.

Numerical experiment provides an accurate and detailed study of the acoustic field structure. In the recent studies (Bessonova O.V. *et al.*, 2009, Khokhlova *et al.*, 2006, Bessonova O.V. *et al.*, 2010) nonlinear focusing of *periodic* waves in a saturation regime was investigated numerically taking into account combined nonlinear effects, diffraction and absorption. Until now, no numerical modeling has been performed yet to study saturation mechanisms in *pulsed* fields of weak acoustic shocks. In the thesis, the effect of wave temporal and spatial structure on parameters of focused acoustic field in a saturation regime is investigated numerically (Karzova *et al.*, 2012). In addition, the formation of spatial structures similar to the Mach stem on the beam axis at the focus is considered (Karzova *et al.*, 2015e).

As mentioned above, the study of nonlinear effects in focused fields of modern medical devices is an important problem of medical acoustics. Understanding the spatial and temporal structure of acoustic fields of medical transducers is necessary for planning induced therapeutic effect and development protocols ensuring the most effective treatment. Extracorporeal shock wave therapy (ESWT) has been actively used recently to treat several musculoskeletal disorders (Kudo *et al.*, 2006, Rompe *et al.*, 2003, Gerdesmeyer *et al.*, 2003, Furia, 2005, Rompe, 2004). Therapeutic bioeffects induced by ESWT include angiogenesis (blood vessel formation), osteogenesis (bone formation), and antinociceptive effects. Although ESWT has been already used in clinics, the actual physical mechanisms of ultrasound action on bones and surrounding tissues in ESWT remain unknown as well as a structure of the acoustic field of ESWT devices. Another new promising medical application of shock waves is the recently developed use of focused ultrasonic radiation force to move kidney stones and residual fragments out of the urinary collecting system (Shah *et al.*, 2010). A commercial diagnostic 2.3 MHz C5-2 array probe is used to deliver the acoustic pushing pulses. The probe works in regime of generating millisecond pulses at the very power operational output (Shah *et al.*, 2012). The optimization of array probe parameters and choosing the optimal treatment protocols require the study of nonlinear acoustic fields generated by the currently used probe at different regimes. In the thesis, nonlinear propagation effects were analyzed using a combined measurement and modeling approach (Kreider *et al.*, 2013, Canney *et al.*, 2008, Bessonova & Wilkens, 2013): the boundary condition for the modeling was set to match low power measurements of the acoustic pressure field (Perez *et al.*, 2013, Karzova *et al.*, 2013, Karzova *et al.*, 2015a).

Aims of the dissertation

The general aim of the dissertation is an experimental and theoretical study of nonlinear focusing and reflection of weak acoustic shocks in the context of aeroacoustic problems and problems of diagnostic and therapeutic medical ultrasound. According to this aim, the following challenges can be outlined:

1. Development of optical methods to measure profiles of the N-wave in the laboratory experiment in air. Investigation the applicability of the developed methods and their temporal resolution.
2. Experimental study of the nonlinear reflection of the N-wave from a flat rigid surface in air. Determination the criteria for observation the irregular reflection.
3. Numerical simulation of nonlinear pulsed and periodic focused acoustic beams generated by Gaussian transducers and piston ones. Study how wave temporal structure and source apodization effect on limited values of the acoustic pressure at the focus. Observation the Mach stem formation at the focus of medical transducers and its description within the framework of Khokhlov-Zabolotskaya-Kuznetsov (KZK) equation.

4. Numerical and experimental study of nonlinear effects in the fields of modern diagnostic and ESWT medical devices. Determination levels of acoustic pressures which provide shock front formation at the focus and saturation of acoustic field parameters.

Presentations and conferences

The results included into the dissertation have been presented at the following Russian and international conferences: at the 162nd, 166th, 168th, and 169th meetings of Acoustical Society of America (USA: San Diego, 2011, San Francisco, 2013, Indianapolis, 2014, Jacksonville, 2015), at XII Russian school-seminar ”Waves phenomena in nonhomogeneous mediums” (Zvenigorod, Russia, 2010), at the conference ”Waves-2013” (Krasnovidovo, Russia, 2013), at International Congress on Ultrasonics (Gdansk, Poland, 2011), at the XV and XV Sessions of Russian Acoustical Society (Saratov, 2011; Taganrog, 2012), at the joint meeting of Acoustical Society of France and European Association of Acoustics ”Acoustics 2012” (Nantes, France, 2012), at 21st International Congress on Acoustics (ISA21, Montréal, Canada, 2013), at 3rd, 4th, and 5th Winter School on Therapeutic Ultrasound (Les Houches, France, 2011, 2013, 2015), at the Summer School on Nonlinear Acoustics and Complex Media (Oleron, France, 2014), at the First Russian conference on Acoustics (Moscow, Russia, 2014), at the XXII International Conference of Students, Graduate Students and Young Scientists ”Lomonosov-2015” (Moscow, Russia, 2015), at 20th International Symposium on Nonlinear Acoustics and 2nd International Sonic Boom Forum (ISNA20, Lyon, France, 2015). All the obtained results have been also discussed at the scientific seminars of the Department of Acoustics of the Moscow State University and at the seminar of the N.N. Andreev Acoustical Institute.

This work was partially supported by the grants RFBR 12-02-31830-mol_a, 12-02-09249, and 12-02-16094, by the international student award of the Acoustical Society of America, by the Student stipend in theoretical physics from Dynasty Foundation, and by the special stipend of the French Government for the preparation of the dissertation under the co-supervision in the frame of the agreement between École Centrale de Lyon (France) and Physics Faculty of the Moscow State University (Russia). Aeroacoustical experiments were performed at École Centrale de Lyon, computational resources were provided by Supercomputer Center of MSU.

Publications

Main results of the dissertation are published in 24 papers, 6 of which are pre-reviewed articles in journals, 12 are articles in conference proceedings and 6 are abstracts of conferences.

Author’s personal contribution

The author took part in all the steps of the research presented in the dissertation. Aeroacoustical experimental data presented in the dissertation (Chapters 1 and 2) were obtained personally by the author in collaboration with the team of LMFA, École Centrale de Lyon (Petr Yuldashev, Edouard

Salze, Sébastien Ollivier, Emmanuel Jondeau, Jean-Michel Perrin). Measurements of acoustic fields of new medical devices Duolith SD1 and Philips C5-2 presented in Chapter 4 were performed by Camilo Perez and Bryan Cunitz (Center for Industrial and Medical Ultrasound, University of Washington, Seattle), correspondingly. The author participated in planning, discussion and data processing of these experiments.

Structure and volume of the dissertation

The dissertation consists of the introduction, four chapters, conclusions, appendix, and the list of references. Each chapter, in addition to the original material, contains an introduction with literature review and conclusions. The references list contains 128 articles on 8 pages; the total volume of the dissertation is 120 pages, including 74 figures and 2 tables.

Figures and formulas in the dissertation are referred as (1.3) where the first number is the chapter number and the second number is the number of the formula or the figure in this chapter.

Dissertation content

The first chapter is devoted to optical methods for measuring pressure profiles of N-wave generated by a spark source in air. In §1.1 a review of existing methods to measure acoustic shock waves is presented and limitations of measuring N-waves by condenser microphones are discussed. Optical methods are proposed to use as an alternative way for measurements of acoustic shock pulses. In §1.2 the experimental setup designed for optical schlieren measurements of spark-generated acoustic waves in homogeneous air is presented. A procedure of reconstruction of the acoustic pressure waveforms from schlieren images is described in §1.3. Pressure waveforms were reconstructed from the light intensity patterns in the recorded images using an Abel-type inversion method. Absolute pressure levels were determined by analyzing at different propagation distances the duration of the compression phase of pulses, which changed due to nonlinear propagation effects. Examples of the reconstructed pressure signatures at different distances from the source are presented in §1.4. The time resolution of the method (3 μs) was restricted by the exposure time of the high-speed camera. Another optical method proposed in the thesis for measurements of spherically diverging N-waves is based on the Mach-Zehnder interferometry technique. The experimental setup is described in §1.5. In §1.6 the reconstruction method to restore pressure waveforms from optical phase signals is described. The reconstruction is based on an Abel-type inversion. In contrast to the schlieren optical method, the Mach-Zehnder interferometery method provides quantitative reconstruction of N-wave pressure waveforms and therefore it is a broadband laser microphone. The results of optical measurements obtained by using the Mach-Zehnder interferometer are given in §1.7. The time resolution of interferometric method (0.4 μs) is mainly determined by the finite beam width (about 0.1 mm). In §1.8 advantages and limitations of both optical methods (schlieren method and the Mach-Zehnder interferometery method) for measurements of acoustic shock waves in air are discussed. In §1.9 conclusions of the first chapter are given.

The second chapter of the thesis is devoted to experimental study of an irregular reflection of an N-wave from a rigid surface in air. In §2.1 a review of existing theoretical and experimental studies of shock wave reflection is presented, as well as reflection of weak shocks under von Neumann paradox is considered. The classification of different reflection regimes of weak acoustic shocks from the rigid surface is given in §2.2. The special attention is paid on the differences between reflection of step-shocks and more complicated waveforms typical for acoustics. In §2.3 the experimental setup designed for schlieren optical visualization of shock wave reflection from a rigid surface is presented. Schlieren images obtained in the experiment are shown and demonstrate the dynamical irregular reflection of the N-wave with increasing length of the Mach stem when the pulse propagated along the surface. Schlieren optical system provides visualization of reflection pattern for the front shock of the N-wave. The Mach-Zehnder interferometery method was used to measure pressure waveforms of the N-wave close to reflecting surface. In §2.4 experimentally measured pressure waveforms are presented. The nonlinear interaction between reflected front shock and incident rear shock of the N-wave is discussed in §2.5. The interaction leads the Mach stem formation above the surface where these shocks intersect and overpressure area is formed above the surface. In §2.6 conclusions of the second chapter are given.

In the third chapter mechanisms of nonlinear saturation in focused acoustic fields of periodic waves and single pulses are considered. In §3.1 a review of analytical approaches providing estimation of limiting values of peak positive pressure in periodic and pulsed focused fields are presented. The possibility to observe the Mach stem formation in the axial focal area is discussed. In §3.2 a numerical model based on the KZK equation is described. The model was used to characterize nonlinear focused fields of pulsed and periodic acoustic beams generated by a piston source and a Gaussian source. In §3.3 the effect of the signal temporal structure on the limiting values of peak pressures are discussed. It is shown that in periodic beams higher peak positive pressures could be achieved than in pulsed beams. §3.4 is devoted to study the effect of source pressure distribution on the spatial structure and limiting values of peak pressures in focused fields. The Gaussian sources were found more appropriate for achieving high peak pressures at the small focal area than piston sources. In §3.5 the interaction between shock fronts of the axially symmetric focused periodic and pulsed fields is considered as a process similar to reflection from the rigid surface. It is shown that the KZK equation allows describing the Mach stem formation in the focal area of the piston source. The structure of the front patterns in the focal region of the beam resembled to the von Neumann reflection as the result of interaction between the edge and the central waves coming from the source. In §3.6 conclusions of the third chapter are given.

The fourth chapter is devoted to the characterization of nonlinear focused acoustic fields of new medical devices used in extracorporeal shock wave therapy (ESWT) and in diagnostic ultrasound. In §4.1 a review of perspectives to use ESWT for several muscular skeletal disorders is presented as well as parameters of ESWT devices. Using of diagnostic probes to create focused ultrasonic radiation force for moving kidney stones out of the urinary collecting system is discussed. The numerical modeling is an important tool for characterization of acoustic fields of these medical devices. In §4.2 the nonlinear effects in focused acoustic field of electromagnetic device Duolith SD1 of ESWT is studied using a combined measurement and modeling approach. The boundary condition for nonlinear modeling of KZK equation was obtained from the experiment by applying the method of the equivalent source. The method uses measurements to obtain parameters of equivalent source, i.e., the source with the same acoustic field on the axis of the beam as the real one. It was shown that in ESWT fields the shock front formation did not occur for the currently machine settings. A true shock formation could be reached if the maximum initial pressure output of the device is doubled. In §4.3 the combined measurement and modeling approach was used to characterize the nonlinear ultrasonic field of the standard diagnostic probe Philips C5-2 used in clinical experiments to push kidney stones. The measurements were done in two steps. The first one was the measurements of low-amplitude pressure waveforms along the axis of the probe and at its focal plane. These measurements were performed at low power output and were used to set boundary condition to the numerical model. The second series of measurements were performed at different output levels and were conducted for further comparison with the results of nonlinear simulations. A 3D numerical model based on the Westervelt equation was used to simulate the nonlinear acoustic field generated in water by the diagnostic probe at different output levels and for different number of operating elements. It was shown that the pushing of kidney stones occurs in a saturation regime. In §4.4 conclusions of the forth chapter are given.

In the general conclusions, the main results are briefly summarized.

Chapter 1

Measurements of N-waves in air using optical methods: a schlieren method and a Mach-Zehnder interferometry method

§1.1 Introduction

High-amplitude (>1 kPa) and short duration (tens of microseconds) acoustic pulses are widely used in downscaled laboratory experiments to simulate sonic boom propagation through atmospheric inhomogeneities (Lipkens & Blackstock, 1998a, Lipkens & Blackstock, 1998b, Lipkens, 2002, Davy & Blackstock, 1971, Blanc-Benon *et al.*, 2005, Averiyanov *et al.*, 2011b, Salze *et al.*, 2014), problems of architectural acoustics (Grillon *et al.*, 1996), urban acoustics (Picaut & Simon, 2001, Picaut *et al.*, 2005) and outdoor sound propagation (Almgren, 1986). The most common ways to generate such pulses in air are to use various spark sources: electrical sparks (Wright, 1983, Yuldashev *et al.*, 2010b, Orenstein, 1982), focused laser beams (Qin & Attenborough, 2004), or explosive-type materials (Loubeau *et al.*, 2006). The waveform of pulses produced in such ways is not always known, but it is expected that due to the prevalence of nonlinear effects the initial pulse becomes an N-wave quite soon. Following the current terminology, let us to call spark-generated pulses as ”N-waves” (DuMond *et al.*, 1946) because of their shape.

The study of the N-wave propagation in atmosphere is important due to high interest to development of civil supersonic aircrafts and inherent sonic boom problem. Outdoor experiments of sonic booms are not numerous because they are complex and expensive projects (Lee & Downing, 1991, Maglieri *et al.*, 1992). In addition, it is not possible to control all parameters of the atmosphere along the propagation path of the N-wave (Elmer & Joshi, 1994, Willshire & Devilbiss, 1992). Alternatively, laboratory-scaled model experiments could be performed instead of outdoor measurements. In model experiments, parameters of an acoustic source and a propagation medium are well controlled. Despite the fact that model experiments do not reproduce the tapered geometry of a wavefront they are of great importance for understanding fundamental properties of nonlinear propagation of N-waves.

Before studying the propagation of N-waves in complex cases of turbulent atmosphere, high-precision measurements of N-waves should be performed first in a homogeneous medium. It turns out that the actual waveform of spark-generated pulses, particularly their rarefaction phase, can be very different from the symmetric shape of an N-wave. Nevertheless, the N-wave model is widespread to describe pressure signatures of shock pulses during their propagation in air (Wright, 1983, Yuldashev *et al.*, 2010b, Averiyanov *et al.*, 2011a). Even if the waveform is not restricted to have the N-wave shape in simulations of pulse propagation through homogeneous (Yuldashev *et al.*, 2010b) and turbulent media (Averiyanov *et al.*, 2011a), the N-wave assumption is still often used to set a boundary condition to the model. This simplified assumption may introduce errors, for example, in the simulation of pulse propagation through a caustic, in which the resulting waveform resembles the derivative of an initial wave (Lipkens & Blackstock, 1998a, Averiyanov *et al.*, 2011a). Accurate measurement of high-amplitude and short-duration acoustic waveforms at distances close to the source is therefore critical to accurately determine the boundary condition for the modeling. Also it is important for studying the environmental impact of sonic boom as our perception of a noise is largely determined by the rise time of the shock fronts, their amplitude and duration of the N-wave (Fidell *et al.*, 2002, Leatherwood & Sullivan, 1992).

Propagation of spark-generated acoustic pulses in homogeneous air has been studied experimentally by several teams, particularly by Wright with co-workers (Wright, 1983, Wright & McKittrick, 1967, Wright & Medendorp, 1968) and Yuldashev with co-workers (Yuldashev *et al.*, 2010b, Yuldashev *et al.*, 2008b). Although several methods have been proposed to characterize acoustic fields produced by sparks, certain measurement limitations still exist. The most common approach is to measure pressure signatures of N-waves using acoustic microphones. However, the bandwidth of commercially available high-frequency condenser microphones does not typically exceed 150 kHz at -3 dB level, while the spectrum of shock pulses extends up to 1MHz; in addition, calibration of microphones at high frequencies is often not accurate. A microphone response and the resulting waveform distortions are also dependent on the microphone mounting. This results in significant distortions of the measured waveforms and steep shock fronts (Yuldashev *et al.*, 2010b, Yuldashev *et al.*, 2008b). In most cases there is no possibility to theoretically estimate these distortions. Moreover, waveform measurements are impossible close to a spark source because maximum pressure is out of a condenser microphone linear range. In addition, the pressure level is so high that it can damage microphones. Note also that acoustic measurements could be performed using piezoelectric dynamic pressure sensors, which are appropriate in the case of very high amplitude pressure waves (>100 kPa), but their main disadvantage is low sensitivity (14.5 mV/kPa) and resolution (for example, 3.4 Pa for the model 113B28 PCB Piezotronics).

An alternative method to measure shock pulses produced by sparks is to use optical methods instead of microphones. The basic principle of these methods is that the acoustic wave introduces variations of air density and corresponding variations of optical refractive index; as a result, the light beam deflects from its initial direction when passing through an acoustic signal.

Measurements of shock waves using optical methods have been widely treated in literature (Mach & Salcher, 1887, Settles, 2001, Merzkirch, 1974, Yuldashev *et al.*, 2008a, Yuldashev *et al.*, 2010a, Cowan & Hornig, 1950, Greene *et al.*, 1951, Panda & Adamovsky, 1995, Panda, 1995). They can be divided into three types: shadowgraphy, schlieren, and interferometry methods. However, although weak shocks have been addressed (Settles, 2001), most of the effort was generally focused on measuring strong shocks created by supersonic flows; the thickness of strong shocks was usually estimated using indirect methods based on the shock speed measurements. For weak shocks optical methods are usually used only for visualization of the field structure but not for quantitative measurements of pressure waveforms.

In a recent work (Yuldashev *et al.*, 2010b), an optical focused shadowgraphy technique was used to visualize the front shock of spark-generated N-waves. An estimation of the front shock width and rise time was then obtained, thanks to numerical simulation of optical beam propagation through the shock. A good agreement with the measurements was shown (Yuldashev *et al.*, 2010b). Although the shadowgraphy technique provided a good temporal resolution of the high amplitude front shock of the pulse, it was not sufficiently sensitive to restore the whole waveform or even the rear shock of the pulse. The reason is that shadowgraphy method is sensitive to the second derivative of pressure, i.e., it captures sharp changes of pressure at the front shock, while smooth variations of pressure in the pulse are missed.

Holographic interferometry (Mizukaki, 2010) has been used to visualize explosion-type waves, but the resolution and the accuracy of the restored waveforms were significantly lower than in the microphone measurements. Laser interferometry can also be used to measure high-amplitude and short duration acoustic pulses in air, however, to our knowledge, no quantitative analysis has been performed to this day for shock waves (Smeets, 1977).

The goal of this chapter is to demonstrate that optical methods (the schlieren method and the Mach-Zehnder interferometry method) are capable to reconstruct absolute pressure signatures of spark-generated acoustic pulses in homogenous air (Karzova *et al.*, 2015d, Yuldashev *et al.*, 2015). Both optical methods are based on the fact that the distribution of light intensity in the measured schlieren images or in interference pattern is associated with the acoustic wave by the Abel-type transform. In the case of the schlieren method Abel-type transform contains an unknown normalization constant which does not permit to determine absolute pressure values, only the shape of an acoustic signal can be reconstructed. Absolute pressure levels were obtained by analyzing lengthening of the compression phase of the pulse with distance caused by amplitude-dependent nonlinear propagation effects. The Mach-Zehnder interferometry method provides quantitative accurate measurements of pressure signatures of N-waves. The time resolution in measured by the Mach-Zehnder interferometer waveforms is six time better than the bandwidth of 1/8-inch condenser microphones (Brüel&Kjær, B&K and G.R.A.S., Denmark); thus the Mach-Zehnder interferometer is a reliable tool to calibrate broadband acoustical microphones.

§1.2 Experimental setup for optical measurements using a schlieren system

1.2.1 Visualization of shock fronts using a schlieren optical method

Optical schlieren method is widely used for a visualization of optical inhomogeneities in transparent refracting media (Settles, 2001, Vasil'ev, 1964). The conventional schlieren system was realized by German physicist August Toepler in 1867. The basic idea of the method is illustrated in Fig. 1.1. A light beam from a point light source or a slit (1) is directed by lens or by system of lenses and mirrors (2-2′) through the test object (3). After propagating through optical inhomogeneities (4) the light is focused on a sharp edge of an opaque screen (5) called a Foucault knife. If there are no optical inhomogeneities light is blocked by the screen. In the presence of the optical inhomogeneity (4) a part of rays is deflected and passes above the screen edge. A lens (6) is placed behind the screen to project deflected light rays on a projection screen (7) and to obtain an image (8) of optical inhomogeneities which scatter light. An optical knife (5) provides a dark background on the screen (7) since it blocks undeflected rays and the schlieren image is bright. If the optical knife (5) is removed the image is not contrast.

The propagation of acoustic waves in a medium introduces variations of air density and corresponding variations of optical refractive index. If the acoustic wave contains a shock front then a large gradient of the refractive index will be created in the location of a shock. This allows to use the schlieren method for optical visualization of shocks. The brightest parts of the schlieren image correspond to the maximum values of pressure derivatives (Settles, 2001), i.e., demonstrate the location of the shock front.

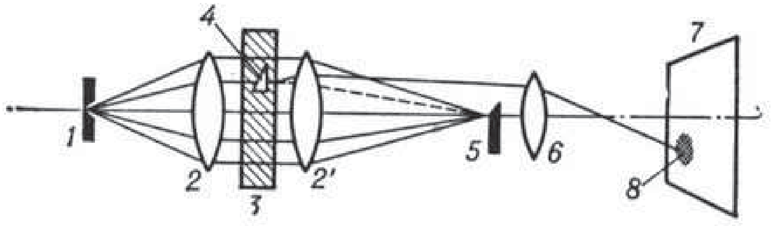

Figure 1.1: The scheme of the schlieren system. 1 – a point light sorce, 2-2′ – a system of lenses and mirrors, 3 – test object, 4 – an optical inhomogeneity, 5 – an optical knife, 6 - a lens, 7 - a projection screen, 8 - a schlieren image. The figure is taken from the Internet: dic.academic.ru/dic.nsf/enc_physics/2531/.

1.2.2 Experimental setup

A top view of the experimental setup designed for optical schlieren measurements of spark-generated acoustic waves in homogeneous air is shown in Fig. 1.2. A spark source (Fig. 1.3 (a)) with a 21 mm gap between tungsten electrodes and with an applied voltage of 15 kV produced high amplitude pressure pulses that readily turned to a shock waveform when propagating from the spark. The

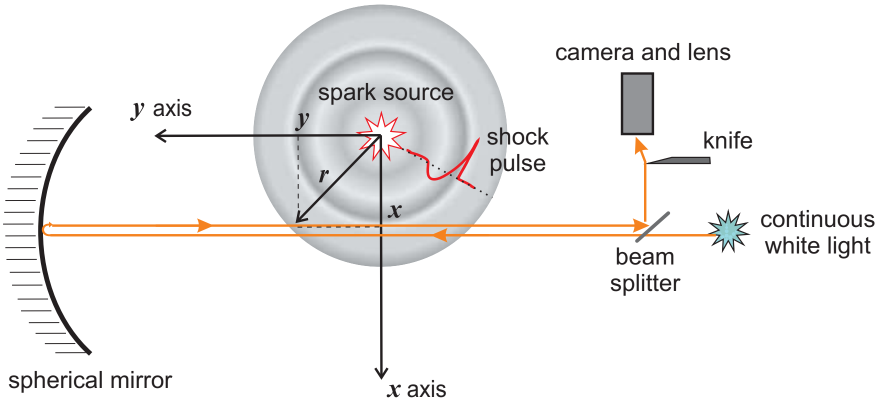

Figure 1.2: Illustration of the experimental setup, the view is from the top along the z axis. Acoustic pulses are produced by a 15 kV spark source located at $r = 0$. Corresponding variations of the optical refractive index are schematically shown by gradients of the gray color. A schlieren optical system used to visualize the pressure wave consists of QTH continuous light source, a beam splitter, a spherical mirror, an optical knife, and a high-speed camera (Phantom V12 CMOS). Solid lines with arrows illustrate the trajectory of the light beam in the absence of acoustic wave.

repetition rate of the pulses was 1 Hz; the wavefront was assumed to have a spherical geometry. Acoustic pulses introduced variations of air density and, as a result, variations of the optical refractive index which are schematically shown in Fig. 1.2 by gradients of the gray color. These variations were visualized using the schlieren method. The schlieren system was composed of a quartz tungsten halogen (QTH) continuous white light source mounted in the geometrical focus of a spherical mirror with 1 m radius of curvature, a beam splitter, an optical knife (a razor edge), and a high-speed Phantom V12 CMOS camera. A metal plate with a circular hole of 2 mm in diameter was glued to the light source in order to have a point light source (Fig. 1.3 (b)). Light beam was transmitted through the beam splitter and through the test zone of the acoustic pulse propagation. Then, the light reflected from the mirror, intersected the test zone once again, and propagated back to the beam splitter (solid lines with arrows in Fig. 1.2).

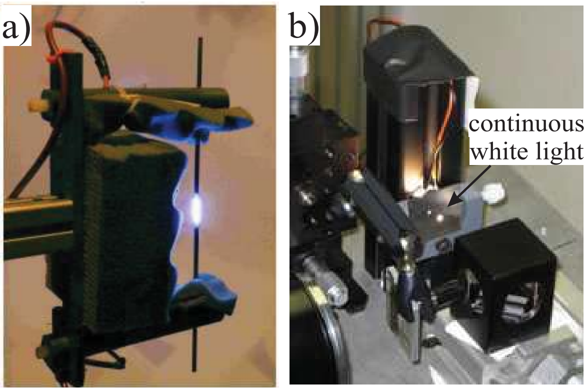

Figure 1.3: (a) A spark source, (b) a light source and a beam splitter.

Spatial variations of the light refractive index n caused by the acoustic wave led to deviation of a part of light rays from the initial propagation direction. Light rays that were not deflected by acoustic pressure inhomogeneities were blocked by the optical knife located in the focal point of the beam. Deflected rays bent around the razor edge were captured by a high-speed camera to form a schlieren image. Double passing of the light beam through the test zone provided better contrast of the image. The brightness of these images corresponds to modulation of the light intensity and is proportional to the gradient of acoustic pressure (Settles, 2001).

§1.3 Theoretical background: reconstruction of an acoustic waveform from a schlieren image

In this paragraph, the algorithm for reconstructing pressure signatures from schlieren images and corresponding assumptions for its correct interpretation are presented. The proposed method includes two steps. First, the waveforms of acoustic pulses were obtained from schlieren images. Then, the absolute pressure values were determined by analyzing the change in duration of the compression phase of the pulses at different distances from the source.

1.3.1 Algorithm for reconstructing dimensionless pressure signatures of N-wave using an Abel-type inversion method

Acoustic pressure p can be related to the perturbation of the optical refractive index n. The refractive index n is related to the air density ρ via the Gladstone-Dale constant K (Merzkirch, 1974): $n + n_0 = 1 + K(\rho_0 + \rho)$, where ρ_0 is the ambient density, and ρ is the density perturbation caused by the acoustic wave, n_0 is the ambient refractive index. Under experimental condition, the density perturbation can be regarded as a linear function of acoustic pressure p: $\rho = p/c_0^2$, where c_0 is the ambient sound speed; higher order terms can be neglected as the acoustic pressure is small compared to the ambient atmospheric pressure p_{atm}: $p/p_{\text{atm}} \sim 0.01$. The refractive index therefore can be expressed as

$$n = K\frac{p}{c_0^2}. \tag{1.1}$$

Variation of the refractive index n produces a phase shift φ_{opt} of the light beam. In the xy plane, shown in Fig. 1.2, the phase shift accumulates while the light propagates along the y axis. Since the phenomenon is symmetrical with respect to the plane $z = 0$, the light rays are assumed not to deviate from the xy plane. Neglecting light reflection by acoustic inhomogeneities and taking into account double crossing through the test zone, one can write the phase as $\varphi_{opt}(x) = 2 \cdot (2\pi/\lambda) \int\limits_{-\infty}^{+\infty} n(x,y)dy$, where λ is the optical wavelength. Radial symmetry of the wavefront allows us to rewrite the expression for the phase as

$$\varphi_{opt}(x) = 2 \cdot \frac{2\pi}{\lambda} \int\limits_0^{+\infty} 2n(r = \sqrt{x^2+y^2})dy = 2 \cdot \frac{2\pi}{\lambda} \int\limits_x^{+\infty} \frac{2n(r)rdr}{\sqrt{r^2-x^2}}. \tag{1.2}$$

Equation (1.2) is the direct Abel transform of the function $n(r)$ (Bracewell, reprint 2000). Inversion of the Abel transform (1.2)and the relationship $s = \lambda\varphi_{opt}/2\pi$ between the optical path length s and the phase φ_{opt} gives

$$n(r) = -\frac{1}{2\pi} \int\limits_r^{+\infty} \frac{ds}{dx} \frac{dx}{\sqrt{x^2-r^2}}. \tag{1.3}$$

In the experiments, the light intensity distribution I is the quantity measured in the perpendicular image xz plane of the schlieren arrangement. For a schlieren system, the light intensity of the image formed behind the optical knife is proportional to the angle of deviation of rays (Settles, 2001). Taking into account the spherical symmetry of the wavefront, the angle of light deviation in the test zone can be written as $\varepsilon = \partial \mathrm{s}/\partial r_1$, where $r_1 = \sqrt{x^2+z^2}$ is the radial coordinate in the image plane xz. Thus, the light intensity $I(r_1)$ in the schlieren image is

$$I(r_1) = -C\frac{\partial s}{\partial r_1}, \tag{1.4}$$

where C is an unknown constant and the sign minus is introduced to account for the knife orientation. For example, if the knife blocks the light from the opposite side of the beam, the same schlieren image is formed but the bright areas of the image are replaced by the dark ones and vice versa. Integrating the intensity in Eq. (1.4), one can obtain the optical path length s as

$$s(r_1) = \frac{1}{C}\int\limits_{r_1}^{+\infty} I(r')dr', \tag{1.5}$$

where r' is a dummy integration variable. Due to the radial symmetry of the optical path length s in the plane xz, one could write Eq. (1.5) in the one dimensional (1D) case of $z = 0$

$$s(x) = \frac{1}{C}\int\limits_{x}^{+\infty} I(r')dr'. \tag{1.6}$$

Combining Eqs. (1.1), (1.3), and (1.6), one obtains the following relation between the pressure signature p and the schlieren image intensity I:

$$p(r) = -\frac{c_0^2}{2\pi KC}\int\limits_{r}^{+\infty}\frac{d}{dx}\left(\int\limits_{x}^{+\infty} I(r')dr'\right)\frac{dx}{\sqrt{x^2-r^2}}. \tag{1.7}$$

Equation (1.7) contains the unknown constant C, which makes it impossible to reconstruct absolute pressure levels directly from the images. Nonetheless, dimensionless pressure waveforms can be reconstructed by calculating the integral

$$p(r) \sim \int\limits_{r}^{+\infty}\frac{d}{dx}\left(\int\limits_{x}^{+\infty} I(r')dr'\right)\frac{dx}{\sqrt{x^2-r^2}}. \tag{1.8}$$

1.3.2 Estimation of the peak positive pressures from the pulse elongation

In order to determine the absolute pressure values in the reconstructed waveforms, the lengthening of the N-wave with distance caused by nonlinear propagation effects was analyzed. The analytic solution of the 1D simple wave equation generalized for spherically divergent waves was used (Pierce, 1981). The duration of the compression phase T at a distance r of a shock wave having an amplitude p_0 and a compression phase duration T_0 (Fig. 1.4a) at the distance r_0 is given by

$$T(r)/T_0 = \sqrt{1 + \sigma_0 \ln(r/r_0)}, \tag{1.9}$$

where $\sigma_0 = (\gamma + 1)r_0 p_0 / 2\gamma p_{\mathrm{atm}} c_0 T_0$.

Here γ is the heat capacity ratio equal to 1.4 for air. In acoustics, Eq. (1.9) is associated with nonlinear propagation of an ideal spherically divergent N-wave, but it also remains valid for non-symmetrical shock waves if only the compression phase is considered. Equation (1.9) therefore, can be applied to determine the pressure amplitude p_0 from the duration of the compression phase in the waveforms measured at different distances from the spark source. In the schlieren experiment, the spatial extent d of the compression phase of the wave was measured instead of the duration. However, since the acoustic wave does not change greatly over a propagation distance equal to its wavelength, the duration of the compression phase can be related to its spatial extention via the sound speed: $d = Tc_0$.

1.3.3 Conditions for the applicability of an algorithm

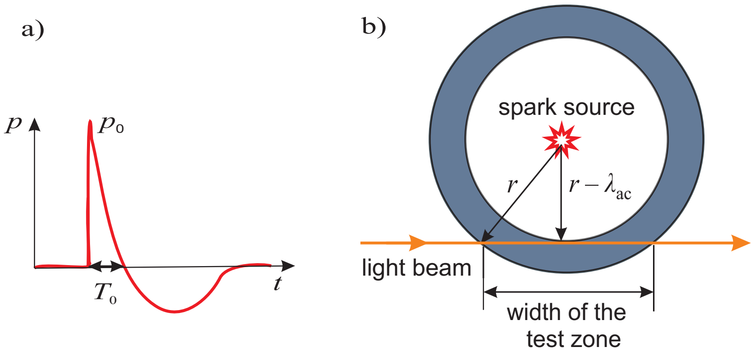

Figure 1.4: (a) Typical waveform produced by the spark source; p_0 and $T_0$are the peak positive pressure and the duration of the compression phase, correspondingly. (b) Sketch illustrating the calculation of the width of the test zone. Location of the acoustic pulse is shown in gray.

The reconstruction algorithm described above is valid under several assumptions. First, it is assumed that the method is valid despite the optical beam not being collimated as in classical schlieren systems (Settles, 2001). However, this assumption is valid, since the width of the test zone, i.e., the zone where the light beam actually interacts with the refractive index inhomogeneities, is much smaller than the total beam length, which is equal to twice the radius of curvature of the mirror. Quantitatively, the width of the test zone is estimated as $2 \cdot \sqrt{2\lambda_{ac} r - \lambda_{ac}^2}$, where λ_{ac} is the wavelength of the acoustic wave (Fig. 1.4b). For a maximum propagation distance of 50 cm and a wavelength of 2 cm, the width of the test zone is 28 cm, which is small in comparison to 2 m of the beam length.

The second assumption is that the wave has a spherical wavefront in the xy plane, thus the refractive index $n(r)$ is a function of only the radial distance r. In the experimental conditions, generally it is true; however, for large electrode gaps or small distances this assumption may be slightly violated.

The third assumption is that optical beam propagation is considered in the framework of geometrical optics [Eqs. (1.2) and (1.4)]. Moreover, it is assumed that optical rays passing through the test zone remain straight lines [Eq. (1.2]. These assumptions may be violated near strong shocks where diffraction effects are important (Panda & Adamovsky, 1995, Yuldashev *et al.*, 2010b). In experiment, variations of refractive index n were less than 5% of its value in undisturbed medium and the rise time of shock was about two orders smaller than the pulse duration, thus the framework of geometrical optics is applicable.

1.3.4 Effect of the finite exposure time of the high-speed camera on the waveforms

Accurate estimation of the compression phase duration is a critical point of the method, since this parameter is used to determine the peak positive pressure. However, the duration of the compression phase in the reconstructed dimensionless waveforms was distorted because of a finite exposure time (3 μs) of the high-speed camera, i.e., the shock front was smeared. To simulate the averaging effect induced by the camera, numerical simulations based on the Burgers equation generalized for relaxing homogeneous atmosphere were performed. Numerical model is described in detail in (Yuldashev *et al.*, 2010b). The high-speed camera was assumed to perform a uniform temporal averaging of acoustic pressures arriving at this distance during the exposure time. An ideal spherically diverging N-wave was numerically propagated from the source. Then, for each distance where the measurements were taken, the pressure was averaged over all waveforms (100 waveforms total) which passed through this point during the exposure time. The parameters of the initial N-wave in the numerical model were: the peak pressure $p_0 = 2500$ Pa at a distance from the spark source r_0 =105,6 mm; the shock rise time, defined as the time during which the acoustic pressure increased from 10% to 90% of the peak positive pressure (Lipkens & Blackstock, 1998a), was chosen according to the quasi-stationary solution of the Burgers equation as 0.07 μs; the duration of the compression phase T_0 (or the half duration) of the initial N-wave, defined as the time between the points of the positive half peak at the front shock and zero pressure values, was chosen $T_0 = 17$ μs. Finally, for each distance, the averaged waveform was compared with the original ideal N-wave at the same distance.

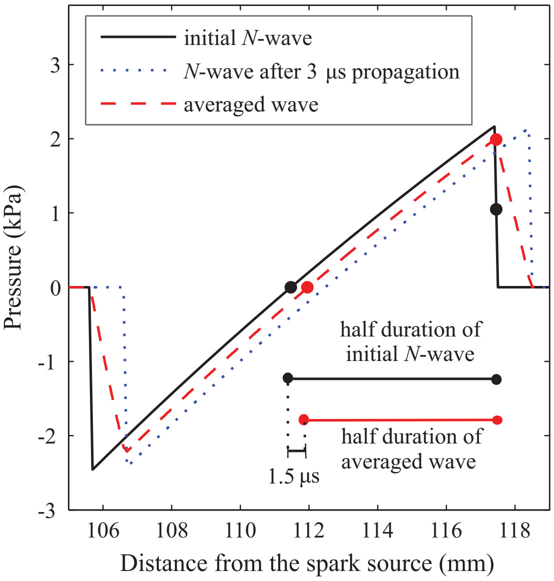

Figure 1.5: Effect of a 3 μs exposure time of the camera on the reconstructed waveform. Solid curve is the initial N-wave that was numerically propagated during 3 μs; dotted curve is the wave after propagation; dashed curve is the averaged wave, which imitates the measured waveform. The half duration of the initial wave can be calculated as the half duration of the averaged wave plus the half of the exposure time (1.5 μs).

A summary of the results of N-wave propagation modeling is presented in Fig. 1.5. The initial N-wave (solid curve) is supposed to imitate a ”real” wave, while the averaged wave (dashed curve) is a ”measured” wave. Note that in the space representation, the N-wave is no longer symmetric: there is a small difference between values of the peak positive and negative pressures. This is caused by the fact that the front shock is located farther from the source than the rear shock and thus has smaller amplitude because of the spherical divergence of the field. The distance between the propagated (dotted curve) and initial pulses corresponds to 3 μs and is about 1 mm.

The finite exposure time leads to the following effects. First, the coordinate of the peak positive pressure and the angles of smooth slopes (more than 3 μs in time or 1 mm in space) of the real and measured waveforms are unchanged. Second, the zero pressure position is shifted by a distance that corresponds to half of the exposure time (see markers at zero pressure level in Fig. 1.5). Finally, the whole duration of the measured wave becomes longer than the real one for a time interval equal to the exposure time. Note also that the shock width (spatial equivalent of the rise time) obtained from the averaged waveform (1 mm) is determined by the exposure time (3 μs). To evaluate the duration of the compression phase correctly using the averaged wave, one should calculate the duration between the peak positive and zero pressure levels and add half of the exposure time, i.e., 1.5 μs in our case (lower right corner of Fig. 1.5). This method to properly evaluate the duration of the compression phase of the pulse is found to be applicable for all distances where the measurements were taken. Note that nonlinear distortions of the propagated wave (dotted curve) are not significant and the correction to the half duration of the measured wave can be obtained based on the assumption of linear plane wave propagation.

§1.4 Results of optical measurements performed by the schlieren system

1.4.1 Dimensionless waveforms generated by the spark-source

An example of a schlieren image recorded with the high-speed camera is shown in Fig. 1.6. Since the brightness of the schlieren image is proportional to the derivative of the pressure the bright areas and the dark ones correspond to different signs of the derivative. One can clearly observe the front shock of the pulse displayed as a bright stripe. The dark area following the front shock

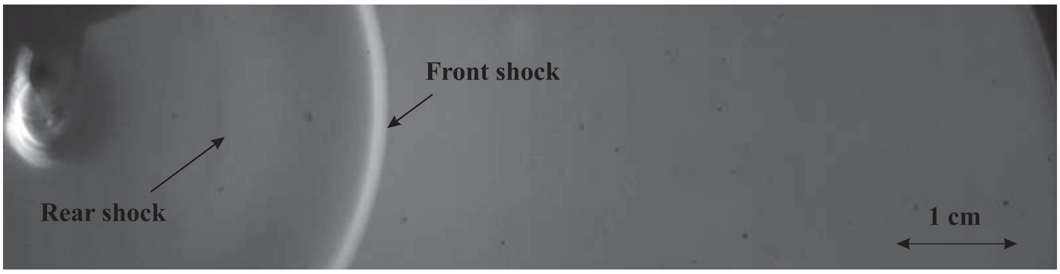

Figure 1.6: A typical schlieren image recorded with the high-speed camera.

corresponds to negative derivative, i.e., the pressure decreases. Finally there is second bright stripe which is less contrast and wider than the first stripe. This area corresponds to the rear front of the pulse. These features of the image demonstrate that the front shock of the spark-generated pulse is sharper and shorter than the rear shock.

A typical schlieren image of the spark-generated pulse measured in the xz plane and processed in Matlab is shown in Fig. 1.6. Here the averaged background image was extracted to handle only the acoustical contribution to the inhomogeneities of the refractive index n. The radial symmetry of the wavefront was used to average the intensity signal and to greatly increase the signal to noise ratio. For this purpose the individual distributions of light intensity were calculated along 500 radial lines as shown in Fig. 1.7(a). A two dimensional (2D) interpolation was used for this calculation. Finally, these 1D distributions were averaged to obtain the resulting signal I [Fig. 1.7(b)]. The inverse Abel transform is then applied to the signal [Eq. 1.8] to calculate the waveform [Fig. 1.7(c)]. Details about numerical calculation of the integral in Eq. 1.8 are discussed in the Appendix A.

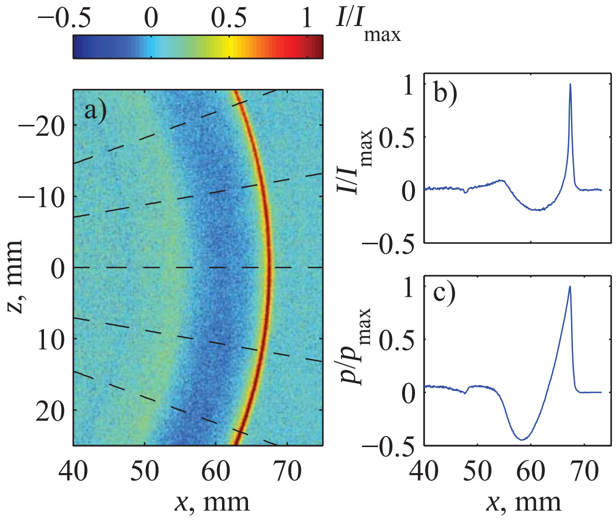

Figure 1.7: Illustration of the pressure signature reconstruction from the schlieren image. The light intensity with extracted background is shown in (a). Individual distributions of light intensity were calculated along 500 radial lines (examples are shown by dashed lines). The intensity signal averaged over 500 radial lines is shown in (b). Reconstructed waveform is presented in (c). All data shown in the figure are normalized by the corresponding maximum values.

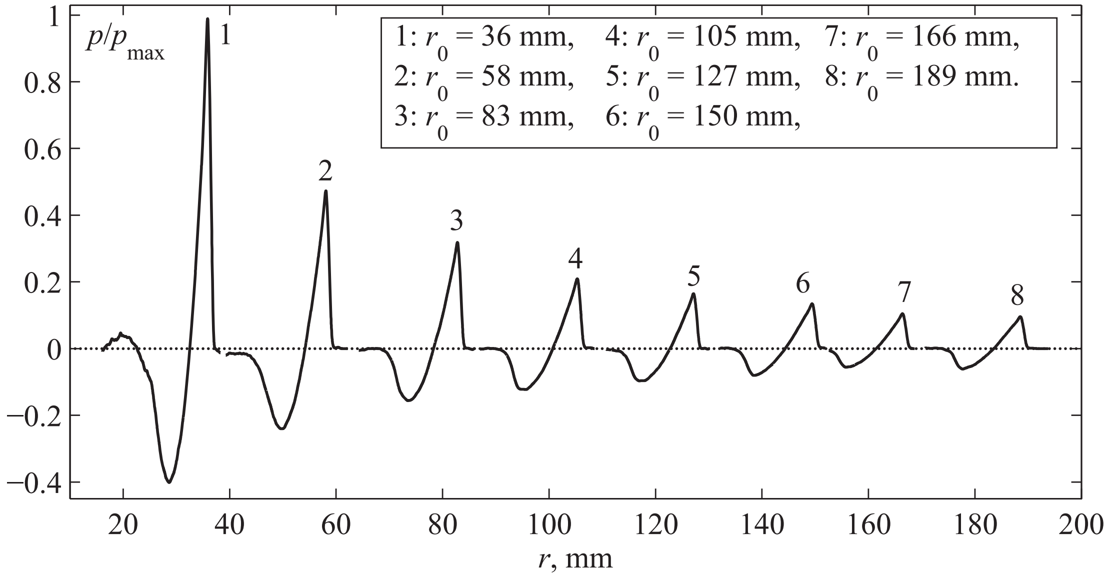

Figure 1.8: Dimensionless waveforms reconstructed from the schlieren images at different distances from the spark source. For every pulse, the distance r_0 is defined as the coordinate of the peak positive pressure.

Examples of waveforms, reconstructed at different distances from the spark source, are shown in Fig. 1.8. The analysis of optical data gives waveforms as functions of the distance from the source. Conversion of waveforms in time domain was done using the ambient sound speed c_0 which was equal to 343 m/s for the experimental conditions (relative humidity 49%, temperature 292 K). The coordinate of the peak positive pressure is considered to be the propagation distance r_0 of the wave. Analyzing dimensionless waveforms plotted in Fig. 1.8, one can conclude that close to the source the acoustic wave is very asymmetric: the negative peak is significantly lower than the positive peak (waveform number 1 in Fig. 1.8) and the rear shock is very smooth and has a long rise time (about 15 μs in time which corresponds to 5 mm in space) in comparison to the front shock. These features are typical for the near field of blast waves (Brode, 1959). The front shock is smeared to 3 μs due to the finite exposure time of the camera.

1.4.2 Reconstructed pressure signatures of N-wave

The duration of the compression phase was calculated as a function of the propagation distance for reconstructed dimensionless waveforms. The smearing of the schlieren image during the exposure time of the high-speed camera was took into account (see paragraph1.3.4). To estimate the coefficient σ_0 in Eq. (1.9), experimental data for $(T/T_0)^2 - 1$ were linearly fitted as a function of ln(r/r_0) using the least squares method (Fig. 1.9). The origin of the graph in Fig. 1.9 corresponds to $T_0 = 13.5$ μs and $r_0 = 70.5$ mm. Fifteen sparks were used to obtain the data presented in Fig. 1.9. The value of 0.486 was obtained for the coefficient σ_0 with a standard deviation of 0.013. The corresponding peak positive pressure was $p_0 = 2\gamma p_{\mathrm{atm}} c_0 T \sigma_0 / (\gamma + 1) r = 3.72$ kPa.

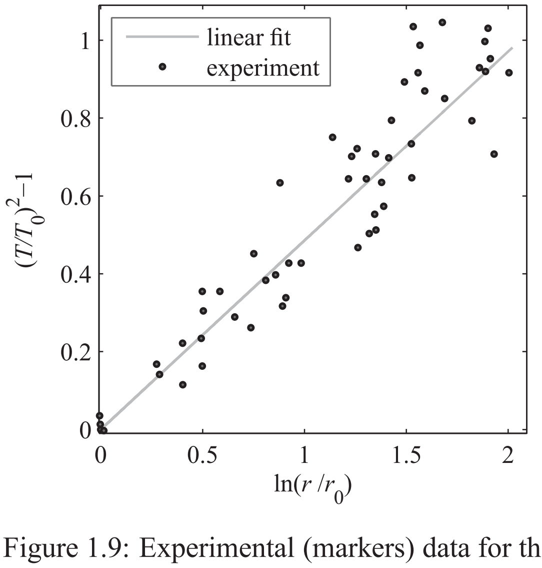

Figure 1.9: Experimental (markers) data for the duration of the compression phase T as a function of propagation distance r. The origin of the graph corresponds to T_0 = 13,5 μs and r_0 = 70,5 mm. Solid line is obtained by linear fitting the experimental values using the method of least squares, the coefficient of proportionality equals 0.486 with standard deviation of 0.013.

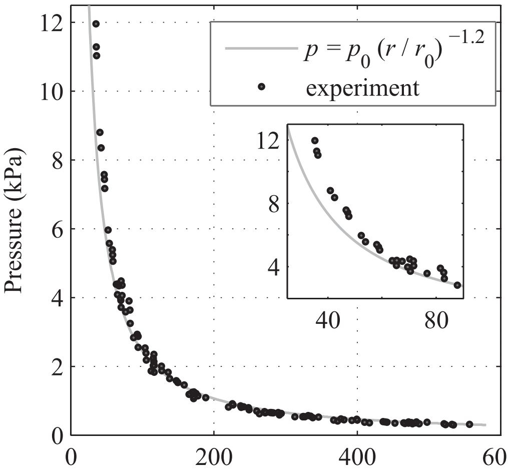

Figure 1.10: Experimental (markers) values of the peak positive pressure at different radial distances from the spark source. Solid curve corresponds to the Reed formula $p = p_0(r/r_0)^{-1.2}$ dependence, where $p_0 = 3.72$ kPa at the distance $r_0 = 70.5$ mm. A zoom view of the data at small propagation distances is given in the inset.

Finally, pressure amplitudes were found for all distances and thus pressure signatures were fully reconstructed. Note that the temporal correction of 1.5 μs to the duration of the compression phase was quite substantialŮwithout taking into account the reconstructed pressure amplitudes would be up to 10% higher.

Reconstructed peak positive pressures at different distances from the spark source are shown in Fig. 1.10 (markers). The power law $p = p_0(r/r_0)^{-1.2}$ provides a good approximation of the peak pressure as a function of distance. Reed proposed (Reed, 1977) this relation for blast waves and it is in good agreement with experimental values starting from about 100 mm from the source. The discrepancy between the Reed relation and experimental values closer to the spark source could be explained by less applicability of either the data processing method or the Reed relation. Nevertheless, both dependencies predict extremely high peak positive pressure close to the spark (about 12 kPa at the distance of 30 mm).

Examples of the reconstructed pressure signatures at different distances from the source are shown in Fig. 1.11. One can observe that close to the source the duration of the compression phase of the wave is about two times smaller than the duration of the rarefaction one (waveform at $r_0 = 36$ mm). As the acoustic wave propagates further from the source, it becomes more symmetric and the rear shock becomes steeper, the rise time reaches 3 μs, which is equal to the resolution time. The durations of compression and rarefaction phases of the wave equalize. Waveforms start to resemble an N-wave only starting from the distances of about $r_0 = 500 - 600$ mm, but even at the distance of $r_0 = 532$ mm (last subfigure) the wave is still not fully symmetric, the peak positive pressure being 1.2 times higher than the peak negative pressure. The measured front shock rise time is limited by the exposure time of the camera and equals to 3 μs which corresponds to a 1 mm shock thickness for all measured waveforms. Note that modern high-speed cameras can provide images at lower exposure times ($0.1 - 0.5$ μs), so the time resolution of reconstructed waveforms can be improved.

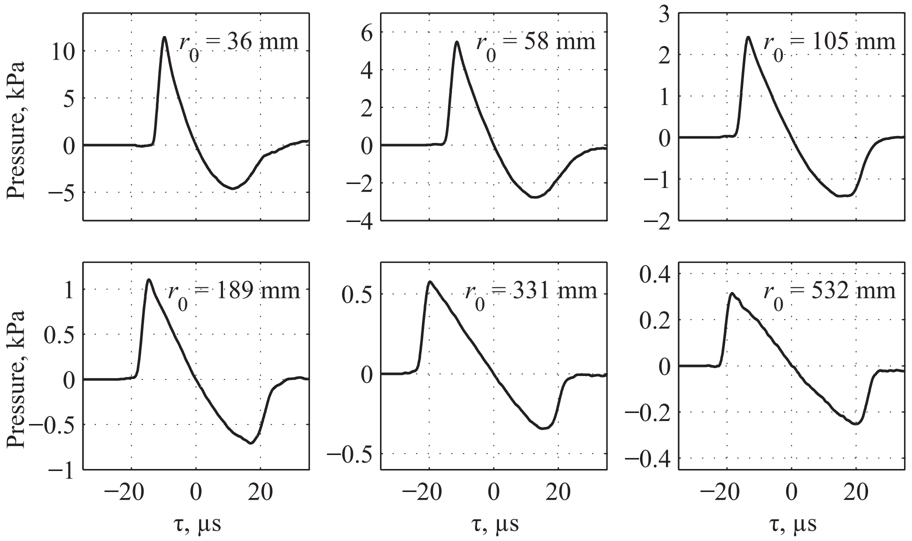

Figure 1.11: Reconstructed temporal waveforms generated by the spark source. The radial position r_0 of the positive peak is noted in each subfigure.

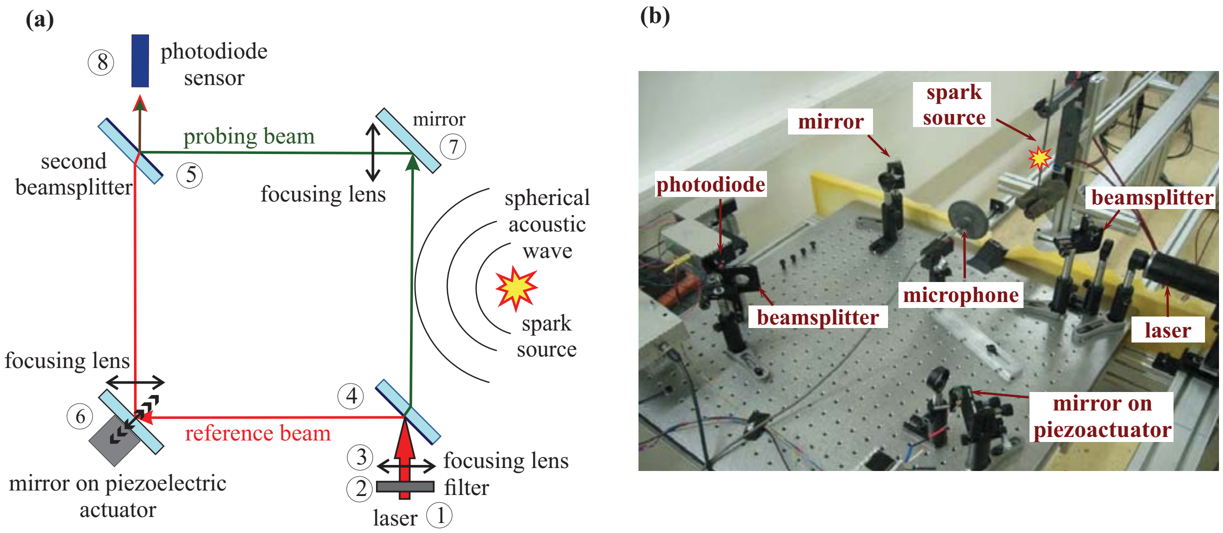

Figure 1.12: (a) Illustration of the experimental setup based on the Mach-Zehnder interferometer. (b) A photo of the experimental setup.

§1.5 Experimental setup for optical measurements using a Mach-Zehnder interferometer

The experimental setup designed for measurements of weak acoustic shock waves using the Mach-Zehnder interferometer is presented in Fig. 1.12 and includes optical and acoustical parts. In the acoustic part the electrical spark source (Fig. 1.3 (a)) described above was used to generate N-waves. The gap between two tungsten electrodes was set to 20 mm and supplied voltage was about 16-20 kV. The Mach-Zehnder interferometer was mounted on a 60×60 cm optical breadboard (PBH51505, ThorLabs, Inc.) and was composed of a laser source ①, two beam splitters (④ and ⑤, 50/50 reflection/transmission), two flat mirrors ⑥ and ⑦, three lenses ③ and a photodiode sensor ⑧ (see Fig. 1.12 (a)). A He-Ne laser (wavelength $\lambda = 632.8$ nm) with a nominal power of 10 mW was used as a coherent light source. Neutral filters were used to attenuate the light beam power down to 1.3 mW to fit requirements of the photodiode sensor ②. All optical elements (beamsplitters, mirrors, filters and lenses) were 25 mm in diameter. A first beamsplitter ④ divides the incident laser beam into a *reference beam* and a *probing beam*. A second beamsplitter sums these two beams to produce an interference intensity pattern at the photodiode surface. The beamsplitters only approximately fitted the declared 50/50 reflection and transmission coefficients. However, in the chosen propagation scheme the probing beam is first transmitted and then reflected while the reference beam is reflected and then transmitted. Thus, deviation of reflection and transmission coefficients from 50/50 ratio is compensated and beams had almost equal intensities at the exit. Propagation paths of the reference and the probing beams formed a square with 35 cm side.

A focusing lens with 20 cm focal length was mounted between the laser and the first beam splitter in order to reduce the probing beam thickness in the zone where the interaction with the acoustic wave occurs ⑨. Thinner probing beam provides better time resolution of the measurement method. Two other focusing lenses (15 cm focal length) were placed a few centimeters after each of the two mirrors. These lenses compensate the divergence of the laser beam and reduce the beam cross-section in order to collect its total optical power on the surface of the photodiode. The beams were aligned in such a way that the output optical field contained only one interferometric fringe. Thus, functioning of the interferometer in the infinite-fringe mode was realized (Merzkirch, 1974)

Light intensity at the exit of the interferometer was captured by a photodiode (NT53-372, Edmund Optics) which has responsivity $r_p = 0.35$ A/W at 632.8 nm optical wavelength, surface of $3.2\ \mathrm{mm}^2$ and 45 pF of electric capacitance at zero bias voltage. The photodiode was connected to a transimpedance amplifier to provide a linear relation between the light intensity and the output voltage. The transimpedance amplifier was designed according to the guidelines given in the Ref. (Graeme, 1996), figure. 3.14. The transmission impedance of the amplifier was $R = 2.2k\Omega$. Thus, the output voltage u_{ph} of the photodiode amplifier is related to the beam power P as $u_{ph} = r_pRP$. A low noise constant reverse bias (2.5 V) was applied to the photodiode to reduce its capacitance and to increase bandwidth of the amplifier up to 16 MHz (at -3 dB).

The output voltage of the photodiode amplifier u_{ph} was fed to the first input of a fully differential amplifier with unit gain and 26 MHz bandwidth. An adjustable low noise reference voltage source was connected to the second input of the differential amplifier to provide necessary bias to the resulting output signal. The optical signal was measured at the first output of the differential amplifier. Inverted signal from the second output of the differential amplifier (u_{fb}) was applied to an input of the feedback loop of a stabilization system.

In the stabilization system the input voltage u_{fb} was filtered by a first-order low-pass filter with $\tau_f = 20$ ms time constant. The output of the filter was connected to a low frequency amplifier (25 kHz bandwidth, gain 10) which was loaded to a piezoactuator. One mirror was glued to the piezoactuator; thus its small displacement provided control on the optical phase difference between the reference and the probing beams (Fig. 1.12 (a),⑥). The piezoactuator (AE0505D08F, ThorLabs) lengthening coefficient was equal to $\varkappa = 9.1 \cdot 10^{-8}$ m/V. The piezoactuator produces the optical phase shift which is proportional to the applied voltage u_{pz}:

$$\varphi_{pz}(t) = 2\sqrt{2}k_0\varkappa u_{pz}(t) = \alpha u_{pz}(t) \tag{1.10}$$

where $k_0 = 2\pi/\lambda$ is the optical wavenumber. The numeric coefficient $2\sqrt{2}$ in the equation (1.10) appears due to the fact that the piezoactuator moves the mirror along a diagonal between the incident and the reflected light beams forming a right angle (Fig. 1.12). The parameter $\alpha = 2\sqrt{2}k_0\varkappa$ in the given experimental conditions was equal to $2.56\ \mathrm{V}^{-1}$.

§1.6 Measurement of acoustical waveforms using a Mach-Zehnder interferometer

1.6.1 Optical signal formation

Light intensity I formed by the interference of the reference and the probing beams at the surface of the photodiode is described by the following equation (Born & Wolf, 1999):

$$I = I_A + I_B + 2\sqrt{I_A I_B}\cos\varphi, \tag{1.11}$$

where I_A and I_B are the intensities of the probing and the reference beams after the second beam-splitter, respectively, and φ is the optical phase difference between them. The measurement protocol was organized as follows. At the fist stage the laser source was disabled and the input bias to the differential amplifier was adjusted in the way to produce zero output signal. Thus, light intensity I is proportional to the output voltage signal and the same equation is applied:

$$u_D = u_A + u_B + 2\sqrt{u_A u_B}\cos\varphi. \tag{1.12}$$

Here u_A is the voltage measured when the reference beam is shaded, and u_B when the probing beam is shaded. Excitation of low frequency mechanical oscillations of the experimental setup produced corresponding variations of the optical phase difference. These low frequency phase variations were used to check the quality of the interference. It was verified that the minimal value of the measured voltage is equal to $u_{D\min} = u_A + u_B - 2\sqrt{u_A u_B}$, and the maximal value is equal to $u_{D\max} = u_A + u_B + 2\sqrt{u_A u_B}$. At the second stage, the bias voltage was moved to the position where the output voltage is equal to $u_C = -(u_A + u_B)$ in the absence of the optical signal from the photodiode. In this case, when the optical signal is turned on, the output voltage of the differential amplifier is proportional to the cosine function of the phase argument φ:

$$u = u_D + u_C = 2\sqrt{u_A u_B}\cos\varphi = u_0\cos\varphi, \tag{1.13}$$

where $u_0 = 2\sqrt{u_A u_B}$ is the amplitude of voltage variations.

The total phase difference φ is the sum of the following items given by:

$$\varphi(t) = \varphi_0 + \varphi_{pz}(t) + \varphi_{ac}(t) + \varphi_n(t). \tag{1.14}$$

Here φ_0 is a constant phase difference related to initial adjustment of the interferometer, $\varphi_{ac}(t)$ is a phase difference produced by the measured acoustic wave, and $\varphi_n(t)$ is a phase related to mechanical perturbations: ground vibrations, acoustic noise, air flows. For example, the interferometer was sensitive even to voice and clapping hands.

The stabilization system was designed to keep the output voltage at zero level in the absence of acoustic wave by compensating low frequency noise and forcing the phase φ to remain close to the $\pi/2$ value. The functioning of the system is described in detail in (Yuldashev *et al.*, 2015). As a result, the output voltage is related to the phase difference associated with the measured acoustic wave as:

$$u = u_0 \sin(\varphi_{ac}(t) + \varphi_r(t)), \tag{1.15}$$

where $\varphi_r(t)$ is a fraction of the noise that was not completely compensated by the stabilization system. Some uncompensated constant offsets also could be present in the function $\varphi_r(t)$. However, as the spectrum of the acoustic phase $\varphi_{ac}(t)$ is concentrated at high frequencies above several kHz and the noise phase $\varphi_r(t)$ is generally a low frequency function (from zero to hundred Hertz), it was always possible to subtract this component, which appeared as an almost constant bias during the acquisition time window.

1.6.2 Optical phase induced by the acoustic wave

A radially symmetric acoustic wave traveling through the probing beam is schematically drawn in Fig. 1.13. The probing beam is located at the distance $x = r_1$ from the spark source. At any time t, the refraction index distribution $n(x, y, t)$ induced by the acoustic wave leads to a phase difference:

$$\varphi_{ac}(t) = k_0 \int\limits_{-\infty}^{+\infty} n(x = r_1, y, t)dy. \tag{1.16}$$

Since the distribution $n(x, y, t) = n(r, t)$ is a radially symmetric function, equation (1.16) can be written as:

$$\varphi_{ac}(t) = 2k_0 \int\limits_{r_1}^{+\infty} \frac{n(r, t)rdr}{\sqrt{r^2 - r_1^2}}. \tag{1.17}$$

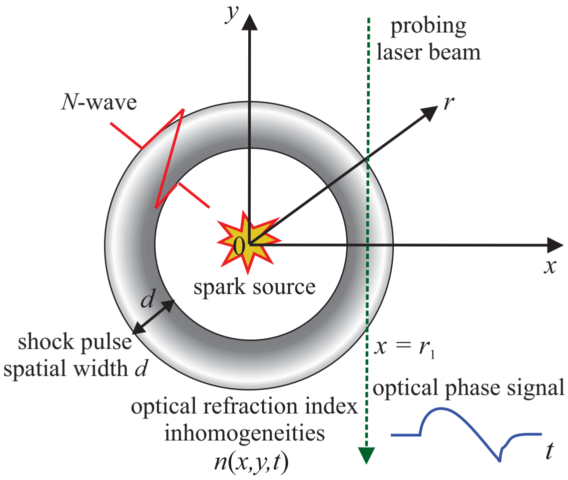

Figure 1.13: Illustration of the optical phase integration along the probing laser beam propagating through a radial distribution of the refraction index inhomogeneities induced be the acoustic wave.

The analytical inversion of equation (1.17) to obtain $n(r, t)$ is not known. However, as functions $n(r, t)$ at different times t are not independent and belong to the same traveling acoustic wave, an approximate method to reconstruct the function $n(r = r_1, t)$ from the phase signal $\varphi_{ac}(t)$ can be used. Since the acoustic wave does not change too much over a propagation distance equal to its wavelength (for the N-wave it is the distance between front and rear shocks), the moving object $n(r, t)$ can be treated as a stationary function at some fixed time t, while the laser beam is supposed to move along the x axis with the sound speed c_0. Thus, using the Abel transform (1.17), and Eqs. (1.1), (1.15), one obtain an expression for pressure waveforms:

$$p(t) = -\frac{c_0^2\lambda}{2\pi^2 K}\int_r^{+\infty}\frac{d}{dr_1}\left(\arcsin\frac{u}{2\sqrt{u_A u_B}}\right)\frac{dr_1}{\sqrt{r_1^2-r^2}}. \tag{1.18}$$

Note that Eq. (1.18) was obtained under following assumptions: (1) the wavefront was supposed to be spherical, (2) diffraction effects were neglected, (3) refraction of the laser beam on the optical heterogeneity was not taken into account, and (4) function $n(r = r_1, t)$ was supposed to be stationary while the laser beam passes optical inhomogeneities. As it was shown by numerical methods in (Yuldashev *et al.*, 2015), these approximations do not introduce significant errors in the reconstructed signal and the error of the of Mach-Zehnder interferometry method is only 2 %.

§1.7 Results of optical experiments performed by the Mach-Zehnder interferometer

Measurements were performed at distances from 10 cm up to 100 cm between the spark source and the probing laser beam. At each distance 140 waveforms were recorded in order to allow statistical analysis of the data.

An example of the reconstructed waveform with corresponding measured optical phase signal at the distance $r = 20$ cm are presented in Fig. 1.14. Here, the phase signal is a result of post-processing: low-frequency and high-frequency noise filtering, background phase correction (subtraction of a constant phase level which is present in the signal before arrival of the N-wave), application of a time window to remove reflected waveforms arriving after the direct wave. The order of the magnitude of the optical phase signal is about 1 radian for an N-wave with 1250 Pa positive peak pressure.

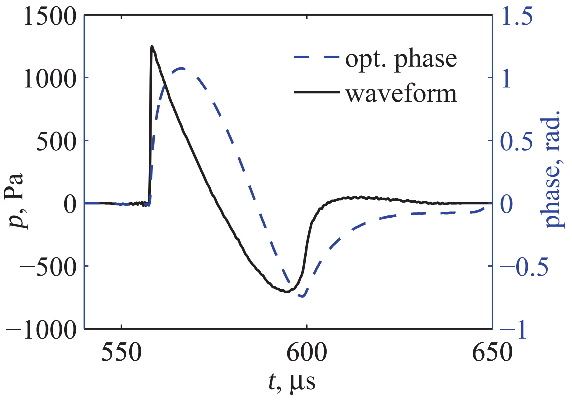

Figure 1.14: An example of measured by the Mach-Zehnder interferometer waveform at the distance $r = 20$ cm (black line) and corresponding optical phase signal (blue line).

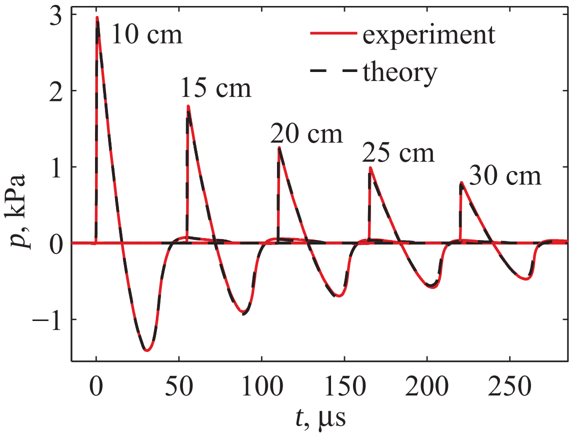

Figure 1.15: Measured (solid line) and simulated (dashed line) waveforms at the propagation distances 10, 15, 20, 25 and 30 cm.

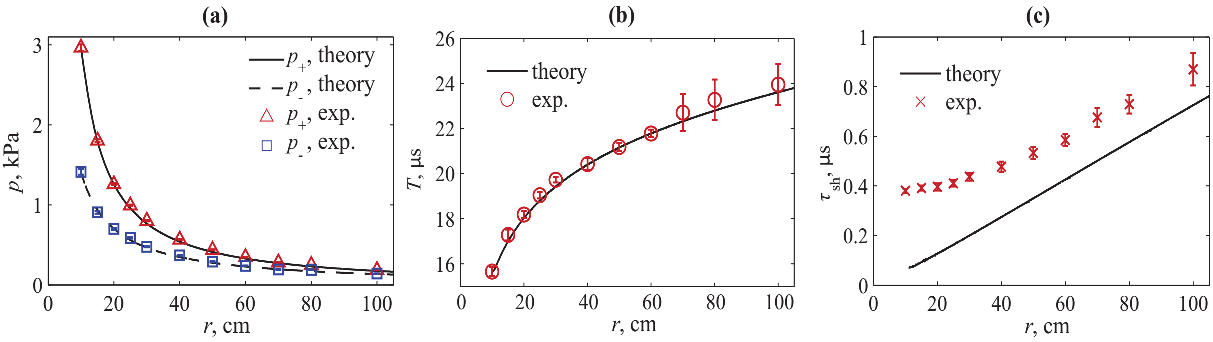

Figure 1.16: Theoretical (solid line) and experimental (markers) data obtained for N-wave parameters: the peak positive and peak negative pressures (a), the half duration (b), and the shock rise time (c).

Waveforms at several different distances r are shown in Fig. 1.15. At each distance r, an experimental waveform (solid line) was obtained by averaging 140 individual waveforms, appropriately shifted in time to fit an average arrival time. The main features of nonlinear propagation of N-wave have been already discussed previously in results of the schlieren measurements. However note one more time that close to the source the acoustic wave rather resembles a blast wave than a symmetric N-wave.

An experimental waveform at $r = 10$ cm was set as an initial waveform for the Burgers equation to perform numerical simulations, whose results were used to validate measurements. The same numerical model was used earlier for evaluation of the effect of the finite exposure time on duration of the compression phase (subsection 1.3.4). The simulated waveforms are shown in Fig. 1.15 by black dashed lines. An excellent agreement between the experimental and theoretical waveforms is observed, which confirms the Mach-Zehnder interferometer method.

Measured and modeled propagation curves of (a) the peak positive (p_+) and peak negative (p_-) pressure, (b) the duration of the compression phase of the waveform (also called half duration (Wright, 1983, Yuldashev *et al.*, 2010b)), and (c) the shock rise time τ_{sh} are compared in Figs. 1.16(a)-1.16(c). The error bars in Fig. 1.16 are obtained from statistical processing of 140 measured waveforms. The experimental and theoretical values of the positive peak pressure match to within an interval of 8% (maximal relative difference is noted). Negative peak pressure – in 10%.

Half duration data are also in good agreement within an interval of 2% [Fig. 1.16(b)]. The increase of the half duration for larger propagation distances is a classical nonlinear effect (Rudenko & Soluyan, 1977). Since this effect is amplitude-dependent, it was used to deduce the amplitude of the N-wave (Wright, 1983, Lipkens & Blackstock, 1998a, Yuldashev *et al.*, 2008b, Yuldashev *et al.*, 2010b). However, with this method it is difficult to achieve an accuracy better than 10% (Yuldashev *et al.*, 2010b).

Experimental results for the shock rise time are less consistent with theory [Fig. 1.16(c)]. The rise time is defined as the time for the pressure on the front shock to increase from $0.1p_+$ to $0.9p_+$. Experimental values of the rise time are always higher than theoretical values. With the experimental conditions in this work, the time resolution is mainly determined by the laser beam width and focal distance of the focusing lens (Yuldashev *et al.*, 2010a). It follows from Fig. 1.16(c) that the experimental value of the time resolution is about 0.4 μs. This value is more than 6 times better than that of standard condenser microphones (2.5-2.9 μs in the case of the Brüel & Kjær, type 4138) and corresponds to 2.5 MHz bandwidth. Using a better quality laser beam, thinner time resolution can be achieved. However, in the case of strong shocks (tens of kPa or more) or very thin laser beams, diffraction of the optical field on the shock front can lead to degradation of performance of the measurement method (Panda & Adamovsky, 1995).

§1.8 Comparison of optical methods: benefits and limitations for acoustic field reconstruction

Optical methods presented in this chapter provide the attractive possibility to obtain quantitative information about characteristics of the high-amplitude and short duration acoustic pulses generated by a spark in a homogeneous atmosphere. Let us discuss benefits and limitations of both schlieren optical method and the Mach-Zehnder interferometry method for acoustic field reconstruction.

The optical schlieren method described in §1.2 and §1.3 has the time resolution limited by the exposure time of the high-speed camera which was 3 μs in our case. Modern high-frequency condenser microphones (for example Brüel & Kjær, type 4138) have the same time resolution, but microphone measurements usually start from 150 to 200 mm away from the source where the pressure levels are not very high and the response of the microphone is linear. In contrast, there is no restriction on the minimal distance from the spark in the schlieren method: one can obtain a schlieren image even at 30 mm from the spark and the corresponding waveform could be reconstructed. Possibly, the data processing methodology is not highly accurate at distances very close to the spark, but nonetheless one can obtain an approximate waveform that could not be measured using microphones. Note also that in microphone measurements it is impossible to estimate distortions induced by the wave diffraction on the microphone, microphone mounting and its frequency response. Smearing of the schlieren image during the exposure time of the high-speed camera is the main cause of distortion. This distortion is quite predictable quantitatively (as discussed in §1.3.4).

The schlieren method has also some advantages with respect to the focused shadowgraphy technique described in (Yuldashev *et al.*, 2010b). The contrast of shadowgrams (images obtained using the focused shadowgraphy technique) is proportional to the second spatial derivative of pressure, while the contrast of schlieren images is proportional to the gradient of pressure. The focused shadowgraphy technique allowed visualizing the front shock of the pulse with a time resolution better than 0.5 μs, which permitted to describe its fine structure. However, if this method is well suited to measure shocks, it is not sufficiently sensitive to measure the pressure decrease following the peak pressure nor the rear shock. The schlieren method is more sensitive to low amplitude pressure variations, and therefore makes it possible to estimate the whole waveform except the fine structure of the front shock (limitation due to the resolution of the camera). However, the exposure time of modern high-speed camera could reach 0.5 μs and the time resolution of the method could be improved.

The accuracy of the schlieren method was found about 10-15%. Four main sources of error are identified. First, the distortion due to the exposure time of the camera; second, assumptions of geometrical optics and spherical symmetry in data processing; third, the low frequency noise associated with slow variations of background intensity between snapshots, which is substantial at large distances from the spark. Finally, although the spark source produces pulses with a good repeatability, their initial amplitude and duration changes from pulse to pulse. This leads to dispersion in experimental data (Fig. 1.9).

The Mach-Zehnder interferometry method is the most promising among all optical methods since it allows to restore pressure waveforms with the best time resolution (0.4 μs in the experiment) and with the best accuracy (2%). The time resolution of the method is determined by the width of the laser beam and could be improved by using a focusing lens. A common disadvantage of the both optical methods (schlieren and interferometry) is their applicability only for waves which have spherical or cylindrical geometry of the wavefront. Thus there is a limitation on geometry of measured acoustic fields. The high accuracy of the Mach-Zehnder interferometry method and its high time resolution allow to use it for calibration of high-frequency condenser microphones.

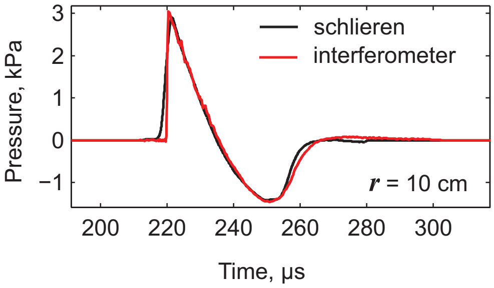

Figure 1.17: Comparison of pressure waveforms obtained using the optical schlieren method (black line) and the Mach-Zehnder interferometry method (red line) at distance $r = 10$ cm from the spark source.

The measurements of N-waves using the schlieren method and the Mach-Zehnder interferometry method were performed by author with the time delay about two years, so a direct comparison between obtained results was difficult. The atmospheric experimental conditions were changed and electrodes of the spark source were replaced. Nevertheless a comparison between pressure waveforms measured by the schlieren system and the Mach-Zehnder interferometer at the same distance $r = 10$ cm show that results are in a very good agreement (Fig. 1.17). To obtain these waveforms a dimensionless waveform measured in schlieren experiment was multiplied by peak positive pressure level of waveform measured using the interferometer. The main difference between waveforms is in structure of the front shock, which is resolved better in the case of the Mach-Zehnder interferometry method.

§1.9 Conclusions

The propagation of nonlinear spark-generated acoustic pulses in homogenous air was studied experimentally using two optical methods: the schlieren method and the Mach-Zehnder interferometry method.

The schlieren method allowed reconstructing dimensionless waveforms at distances from 30 mm to 600 mm from the source. Analysis of schlieren images was based on the assumption of spherical geometry of the acoustic field and the geometrical optics approximations. The reconstruction of dimensionless acoustic waveforms was performed using the Abel-inversion transform. To evaluate the smearing of the waveform during exposure time of the camera, the propagation of a spherical diverging N-wave was simulated using the generalized Burgers equation. A method to evaluate the duration of the compression phase taking into account exposure time of the camera was proposed. The analysis of the elongation of the compression phase duration as a function of the propagation distance allowed to reconstruct the absolute pressure values. The time resolution of the method (3 μs) was restricted by the exposure time of the camera and thus the fine structure of the front shock could not be resolved using the method. The schlieren method has two main advantages: first, it allows reconstruction of the pressure signatures at distances close to the spark source (about 30 mm), where measurements using condenser microphones are impossible; second, it provides the reconstruction of the whole waveform with the good accuracy that has not been achieved using the focused shadowgraphy method.

The optical measurement method based on a Mach-Zehnder interferometer is most suitable method to measure spherically diverging N-waves in homogeneous air. Pressure waveforms are reconstructed from optical phase signal of interferometer using an Abel-type inversion. The interferometric method allows one to reach 0.4 μs of time resolution, which is 6 times better than the time resolution of a 1/8-inch condenser microphone (2.5 μs). The Mach-Zehnder interferometry method is a perspective tool for calibration of broadband condenser microphones.

Chapter 2

Irregular reflection of an N-wave from a rigid surface in air

§2.1 Introduction

2.1.1 Experiments of E. Mach demonstrated the irregular reflection of shocks

Austrian physicist Ernst Mach (Fig. 2.1a) was the first scientist who experimentally observed the phenomenon of shock wave reflection (Mach, 1878, Krehl & van der Geest, 1991). In 1875 he performed very simple and outstanding experiments: he took a soot covered glass plate and put two spark sources above the plate. These sparks were triggered and produced shock pulses simultaneously. Two spherical divergent waves propagated above the plate and marked the soot in their intersection location (Fig 2.1 (b)). After experiment, E. Mach noticed a well-marked trace in the soot. It was a segment which was divided into two lines on its ends (schematically shown as a solid curve in. Fig 2.1 (b)). Ernst Mach demonstrated a great intuition for physical interpretation of observed phenomenon when he concluded that the classical law of reflection was no more valid for shock waves. Moreover, he proposed that the one-line trajectory in a soot indicated a new, irregular type of reflection, consisting of three shocks: the incident and the reflected shocks which intersected above the surface, and a third one, later named the Mach stem, which connected the intersection point with the surface.

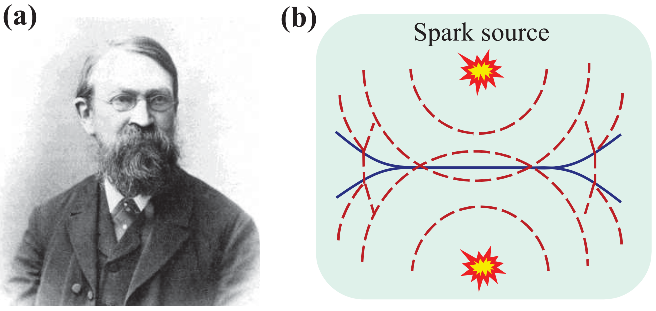

Ernst Mach

1878: Experiments by E. Mach

Figure 2.1: (a) Ernst Mach, (b) scheme of an experiment performed by E. Mach to study shock wave reflection, the view is from the top.

2.1.2 Physical causes of the Mach stem formation

In aerodynamics, there is a well-known relation between the shock velocity u in undisturbed medium and a pressure jump p on the shock front (Uizem, 1977): $u(p) = c_0 + \varepsilon p/\rho_0 c_0$. It means that the shock of greater amplitude propagates faster than the shock of less amplitude. In reflection, the pressure perturbation caused by reflected wave is superimposed on one already caused by the incident wave. It leads to different velocities of incident and reflected shocks. The reflected shock with greater speed starts to overtake the incident shock. If the nonlinear effects are strong or the incident angle is small then the reflected shock could superimpose on the incident one and form the united single shock front - the Mach stem. Thus, the Mach stem formation caused by different speeds of two shock fronts because of nonlinear effects.

2.1.3 A three-shock theory of von Neumann

Theoretical investigation of the shock wave reflection was first carried out almost 70 years later by von Neumann (Fig. 2.2a) in 1943 (Neumann, 1974). He described the irregular reflection by a three-shock theory based on the assumption that all the waves in the flow are shaped as shocks of negligible curvature and thickness, and obey the Rankine-Hugoniot jump conditions (Pierce, 1981, Ben-Dor, 1992), i.e., laws of mass, energy, and momentum conservation:

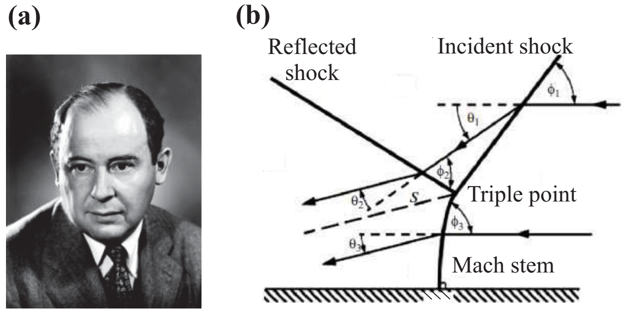

John von Neumann

Mach reflection effect

Figure 2.2: (a) John von Neumann. (b) Description of Mach reflection in a three-shock theory developed by J. von Neumann in 1942. The figure is taken from (Ben-Dor, 1992).

$$\rho_1 u_1 \sin\varphi_1 = \rho_2 u_2 \sin(\varphi_1 - \theta_1), \tag{2.1}$$

$$p_1 + \rho_1 u_1^2 \sin^2\varphi_1 = p_2 + \rho_2 u_2^2 \sin^2(\varphi_1 - \theta_1), \tag{2.2}$$

$$\frac{\gamma}{\gamma - 1}\frac{p_1}{\rho_1} + \frac{1}{2}u_1^2 \sin^2\varphi_1 = \frac{\gamma}{\gamma - 1}\frac{p_2}{\rho_2} + \frac{1}{2}u_2^2 \sin^2(\varphi_1 - \theta_1), \tag{2.3}$$

$$\rho_2 u_2 \sin\varphi_2 = \rho_3 u_3 \sin(\varphi_2 - \theta_2), \tag{2.4}$$

$$p_2 + \rho_2 u_2^2 \sin^2\varphi_2 = p_3 + \rho_3 u_3^2 \sin^2(\varphi_2 - \theta_2), \tag{2.5}$$

$$\frac{\gamma}{\gamma - 1}\frac{p_2}{\rho_2} + \frac{1}{2}u_2^2 \sin^2\varphi_2 = \frac{\gamma}{\gamma - 1}\frac{p_3}{\rho_3} + \frac{1}{2}u_3^2 \sin^2(\varphi_2 - \theta_2), \tag{2.6}$$

$$\rho_1 u_1 \sin\varphi_3 = \rho_4 u_4 \sin(\varphi_3 - \theta_3), \tag{2.7}$$

$$p_1 + \rho_1 u_1^2 \sin^2\varphi_3 = p_4 + \rho_4 u_4^2 \sin^2(\varphi_3 - \theta_3), \tag{2.8}$$

$$\frac{\gamma}{\gamma - 1}\frac{p_1}{\rho_1} + \frac{1}{2}u_1^2 \sin^2\varphi_3 = \frac{\gamma}{\gamma - 1}\frac{p_4}{\rho_4} + \frac{1}{2}u_4^2 \sin^2(\varphi_3 - \theta_3). \tag{2.9}$$

Equations (2.1)–(2.9) are written in the coordinate system in which fronts are fixed, φ_i are incident angles, θ_i are angles of a flow deflection from its initial propagation direction, u_i are speeds of flows (Fig. 2.2). Solution of Rankine-Hugoniot jump conditions Eqs. (2.1)–(2.9) is:

$$\tan\theta_3 = \operatorname{ctg}\varphi_3 \frac{M_1^2\sin^2\varphi_3 - 1}{2 + M_1^2(\gamma + \cos 2\varphi_3)}, \tag{2.10}$$

$$\tan\theta_2 = \operatorname{ctg}\varphi_2 \frac{M_2^2\sin^2\varphi_2 - 1}{2 + M_2^2(\gamma + \cos 2\varphi_2)}, \tag{2.11}$$

$$\tan\theta_1 = \operatorname{ctg}\varphi_1 \frac{M_1^2\sin^2\varphi_3 - 1}{2 + M_1^2(\gamma + \cos 2\varphi_1)}, \tag{2.12}$$

and pressure ratios near the shock front are:

$$\frac{p_2}{p_1} = 1 + \frac{2\gamma}{\gamma+1}(M_1^2\sin^2\varphi_1 - 1), \tag{2.13}$$

$$\frac{p_3}{p_2} = 1 + \frac{2\gamma}{\gamma+1}(M_2^2\sin^2\varphi_2 - 1), \tag{2.14}$$

$$\frac{p_4}{p_1} = 1 + \frac{2\gamma}{\gamma+1}(M_1^2\sin^2\varphi_3 - 1). \tag{2.15}$$

Here M_i are Mach numbers which exceed the values of acoustic Mach number M_a by one. A perpendicularity of the Mach stem to the surface is also proposed: $\theta_3 = \theta_1 - \theta_2 = 0$ and $p_3 = p_4$.

According to Eqs. (2.13)–(2.15), the transition from irregular reflection to regular one occurs at $\varphi_3 = 0°$, i.e., then mathematically the Mach stem becomes parallel to the surface. This ratio is known as the von Neumann criteria and written as:

$$\frac{p_4}{p_1} = 1 + \frac{2\gamma}{\gamma+1}(M_1^2 - 1). \tag{2.16}$$

The three-shock theory was found to be in good agreement with experiments only for strong shocks when the acoustic Mach number M_a was greater than 0.47. For weaker shocks ($0.1 < M_a < 0.47$) the three-shock theory was strongly disagreed with experimental observations supported by numerical simulations. For $M_a < 0.1$ the theory has no physically acceptable solutions and predicts fundamental impossibility of irregular reflection, while the experimental data clearly show that irregular type of reflection for such weak shocks does, in fact, exist. The conflict between three-shock theory and experimental results is known as the von Neumann paradox which was first formulated by Bikhoff in 1950 (Birkhoff, 1950), and irregular reflection pattern in this case is called the von Neumann reflection.

2.1.4 A review of researches devoted to an irregular reflection of shocks

Attempts to resolve the von Neumann paradox were undertaken by several authors in (Skews & Ashworth, 2005, Colella & Henderson, 1990, Brio & Hunter, 1992, Guderley, 1962, Zakharian *et al.*, 2000, Vasil'ev & Kraiko, 1999). Although the von Neumann paradox is still considered to be unresolved, performed experimental studies have revealed many new interesting features of shock front interactions.

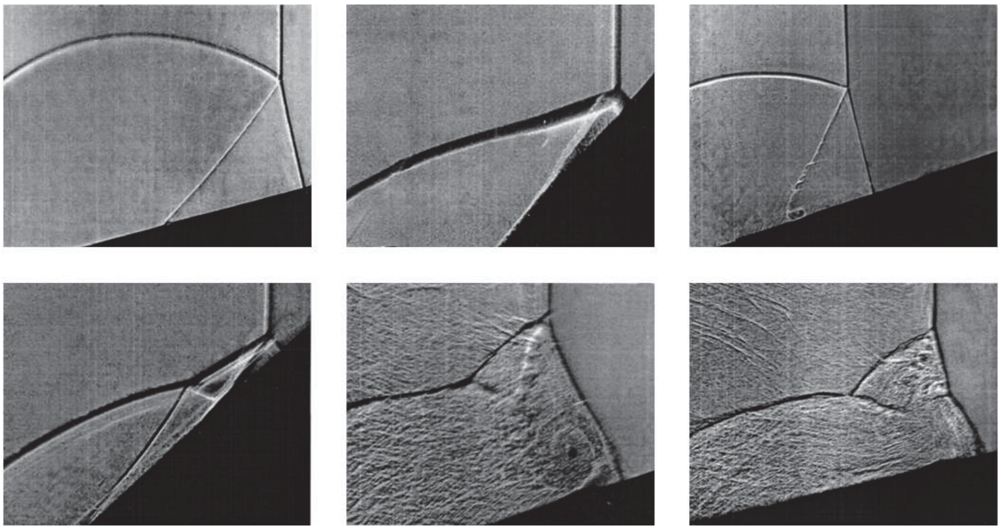

Figure 2.3: Reflection patterns obtained in a shock tube for strong step shocks. The figure is taken from (Semenov $et\ al.$, 2012).

Most of the experiments to study the Mach reflection effect were performed in shock tubes using methods of optical visualization (Semenov *et al.*, 2012, Skews & Ashworth, 2005, Colella & Henderson, 1990). In a shock tube, step shocks with plane front are produced. A wedge is placed in a tube to observe the reflection of the flow by optical methods. Usually shadowgraphy or schlieren methods are used for visualization of reflection pattern. In (Semenov *et al.*, 2012) the complicated spatial structures close to triple point were observed for Mach reflection (see Fig. 2.3) and studied in detail (Semenov *et al.*, 2012, Ben-Dor, 1992).

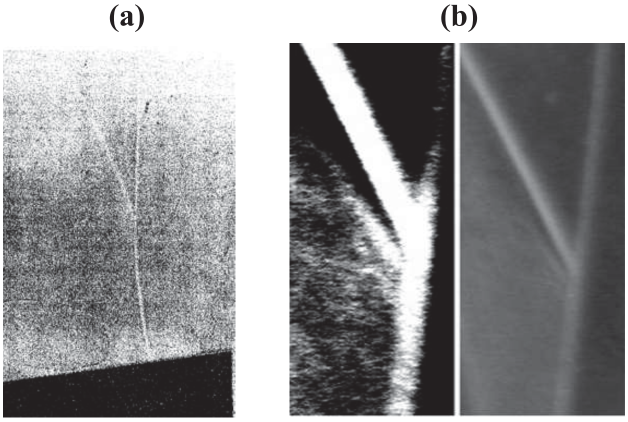

Figure 2.4: (a) The von Neumann reflection of step shock observed in experiments in (Colella & Henderson, 1990). (b) A sequence of triple points observed in experiments in (Skews & Ashworth, 2005). The image on the right is a raw shadowgram while the left image is in enhanced contrast.

In 1990 Colella and Henderson were the first who experimentally and numerically observed a new type of reflection of weak shocks ($M_a = 0.05$) from a rigid boundary - the von Neumann reflection (Colella & Henderson, 1990). In this new reflection type they saw no discontinuity of the slope angle in transition from the incident front to the Mach stem (see Fig. 2.4a).

In addition to experimental studies of weak shock reflection from surfaces, theoretical and numerical efforts were performed in (Tesdall & Hunter, 2002, Brio & Hunter, 1992, Zakharian *et al.*, 2000, Vasil'ev & Kraiko, 1999). In (Brio & Hunter, 1992) numerical modeling is used to study reflection of step shocks from a rigid boundary; the model is based on a two-dimensional (2D) Burgers equation. This model allowed authors to observe the formation of a supersonic jet in a small region behind the Mach stem. Also the numerical model allowed to demonstrate a low-pressure area just behind the triple point, that has been predicted previously only theoretically in (Guderley, 1962). These features were also observed in numerical experiments in (Vasil'ev & Kraiko, 1999, Zakharian *et al.*, 2000) based on Euler's equation.

In 2002 Tesdall and Hunter (Tesdall & Hunter, 2002) used methods of numerical simulations to find a more complex configuration in reflection pattern with a sequence of triple points in the Mach stem. They showed that this spatial structure was located in a very small region below the main triple point, its size was only 2% of the length of the Mach stem. Later Skews and Ashworth (Skews & Ashworth, 2005) constructed a shock tube with diameter of 1.1 m and were able to observe the Mach stem with an extremely large length of about 80 cm. The sequence of triple points was indeed occurred on the Mach stem. Fig. 2.4b demonstrates images obtained in (Skews & Ashworth, 2005) with one more triple point located below the main one (experiments were performed in air, $M_a = 0.04$).

Note that all works mentioned above, both theoretical and experimental, are mainly in the framework of aerodynamics and consider only plane step shocks with acoustic Mach numbers M_a greater than 0.035 While step shocks are typical for aerodynamics, acoustic shock waves usually have more complicated waveforms of an N-wave, blast waves, sawtooth waves, and others. In addition, in nonlinear acoustics the values of acoustic Mach number M_a are on the order of $10^{-2} - 10^{-3}$, which is at least one order smaller than in aerodynamics. The reflection of such very weak, but nonetheless strongly nonlinear acoustic waves has not been studied to the same extent. Moreover, the reflection of acoustic shock waves occurs within the von Neumann paradox and thus is not described by the three-shock theory. It is interesting to refer to historical background and remember that von Neumann by himself considered acoustics and aerodynamics as two fundamentally differing fields. In his opinion, small values of Mach number in acoustics lead to physical impossibility to observe such nonlinear phenomena as irregular reflection (Neumann, 1974).

§2.2 Types of reflection of weak acoustic shocks from a rigid surface

Nonlinear reflection of acoustic shock waves (M_a about $10^{-2} - 10^{-3}$) from a rigid surface was investigated in recent works of Marchiano and co-authors (Marchiano *et al.*, 2007, Baskar *et al.*, 2007). In work (Marchiano *et al.*, 2007) reflection of periodic sawtooth waves ($M_a = 2.3 \times 10^{-4}$) from rigid boundary was studied experimentally in water. Different reflection regimes were observed and then studied in detail using methods of numerical simulations (Baskar *et al.*, 2007). It was shown that the type of reflection depends on the critical parameter a, defined by the shock amplitude p, the grazing angle φ of the incident wave, and a coefficient of nonlinearity β of the propagation medium:

$$a = \frac{\sin\varphi}{\sqrt{2\beta M_a}}. \tag{2.17}$$

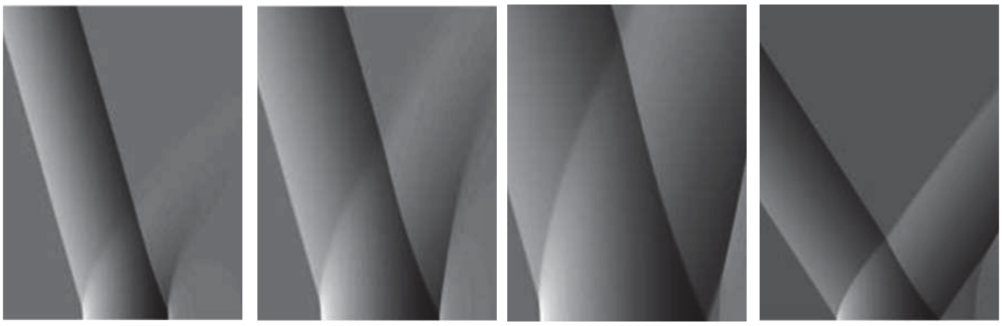

Figure 2.5: Consecutive reflection patterns of the N-wave obtained for different points on the surface. On each pattern reflection of the front shock of the N-wave correspond to the left part of the image while reflection of its rear shock - to the right one. The gradients of a color correspond to the pressure level: white color corresponds to positive pressure, black color - to negative pressure. Figures were taken from (Baskar $et\ al.$, 2007).

Numerical simulations based on the KZ equation were used in (Baskar *et al.*, 2007) to define values of the critical parameter a corresponding to each reflection regime. For plane step shocks four reflection regimes exist. Initially for $0 \leq a \leq 0.4$ weak von Neumann reflection was observed. The term "weak von Neumann reflection" was introduced by the authors of (Baskar *et al.*, 2007) to describe the reflection pattern for almost grazing incidence when the reflected shock does not exist, but the initial plane incident shock has a curvature close to the surface. The range of values $0.4 \leq a \leq \sqrt{2}$ corresponds to the von Neumann reflection, i.e., an irregular reflection regime characterized mainly by the continuous slope of the shock front along the incident shock and the Mach stem. For $\sqrt{2} \leq a \leq 5$ the reflection occurs in a regular regime, but angles of the incident and reflected waves are not equal. Finally, at $a > 5$ classical law of reflection is valid.

In work (Baskar *et al.*, 2007) cases of an ideal plane N-wave and periodic sawtooth wave were also studied in comparison with a step shock reflection. In contrast to step shocks, N-waves and sawtooth waves were found reflected in a dynamical way: the length of the Mach stem was changing while the wave propagated along the surface. This is due to the fact that both the amplitude of nonlinear wave and the incident angle are changed. Thus, current value of the critical parameter a depends on location of reflection point on the surface. In addition, the evolution of the reflection pattern for the front and the rear shocks of the N-wave was different.

Figure 2.5 presents the results on numerical simulation performed in (Baskar *et al.*, 2007) for initial current value of the critical parameter $a = 0.5$. Reflection patterns correspond to different location of reflection point on the surface, from left to right the distance from the first point of the shock wave reflection to the observed region increases. For the front shock of the N-wave authors of (Baskar *et al.*, 2007) obtained following values of the critical parameter a corresponding to different types of reflection: for $0 \leq a \leq 0.4$ weak von Neumann reflection occurred. This range of values coincides with the corresponding one for a plane step shock case. Values $0.4 \leq a \leq 0.8$ correspond to dynamical irregular reflection, when the length of the Mach stem first increases and then decreases; for $a > 0.8$ reflection is regular. Thus, while the N-wave propagates along the surface values of the critical parameter a are gradually increasing due to reducing the amplitude of the incident wave, as a result, the type of reflection varies from weak von Neumann reflection to von Neumann reflection and finally to a regular reflection. Transition from one type of reflection to the another one occurs differently for the rear shock of the N-wave. It is clearly seen (Fig. 2.5) that there is secondary reflected shock behind the rear shock which is formed when irregular reflection becomes regular, and then increases with increasing of the current value of a. Formation of the secondary reflected shock was observed only in reflection of rear shock of the N-wave; there was no such effect in the case of the periodic wave.

In this thesis, reflection of N-waves from rigid boundaries was investigated experimentally using optical methods: the schlieren method and the Mach-Zehnder interferometry method. The goals are to demonstrate experimentally how irregular reflection occurs in air for very weak spherically diverging spark-generated pulses and to evaluate the values of the critical parameter a for different types of reflection. This complements earlier experimental observations on irregular reflections of plane periodic waves in water (Marchiano *et al.*, 2007) since spherical divergent waves, single pulses, propagation in air, and variation in acoustic Mach number were considered.

The experiments were performed by the author of the dissertation in the LMFA at Ecole Centrale de Lyon (France).

§2.3 Visualization of dynamic irregular reflection of a spherical N-wave using an optical schlieren method

The experimental setup designed for optical visualization of shock wave reflection from a rigid surface is shown in Fig. 2.6. Acoustic shock waves (1) were produced by a 15kV electric spark source (2) with 21 mm gap between tungsten electrodes (its calibration is described in detail in a previous chapter). Spherically divergent N-waves reflect from the rigid surface (3), located at a

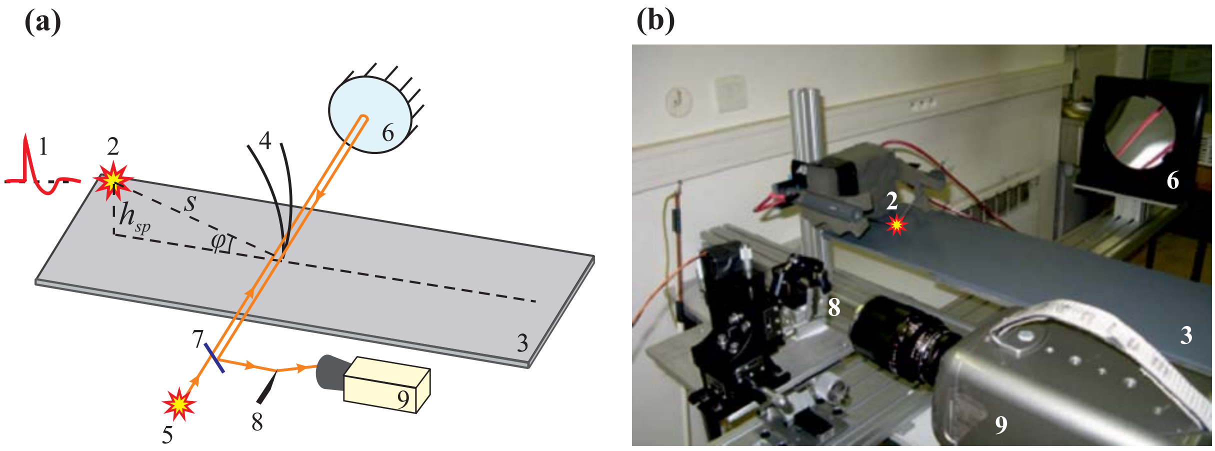

Figure 2.6: Illustration (a) and a photo (b) of the experimental setup: 1 – shock acoustic pulse, 2 – a spark source, 3 – a rigid surface, 4 – reflection pattern consisting of incident and reflected fronts, 5 – QTH continuous light source, 6 – a spherical mirror, 7 – a beam splitter, 8 – an optical knife, and 9 – a high-speed camera (Phantom V12 CMOS). Solid lines with arrows illustrate the trajectory of the light beam in the absence of acoustic wave.

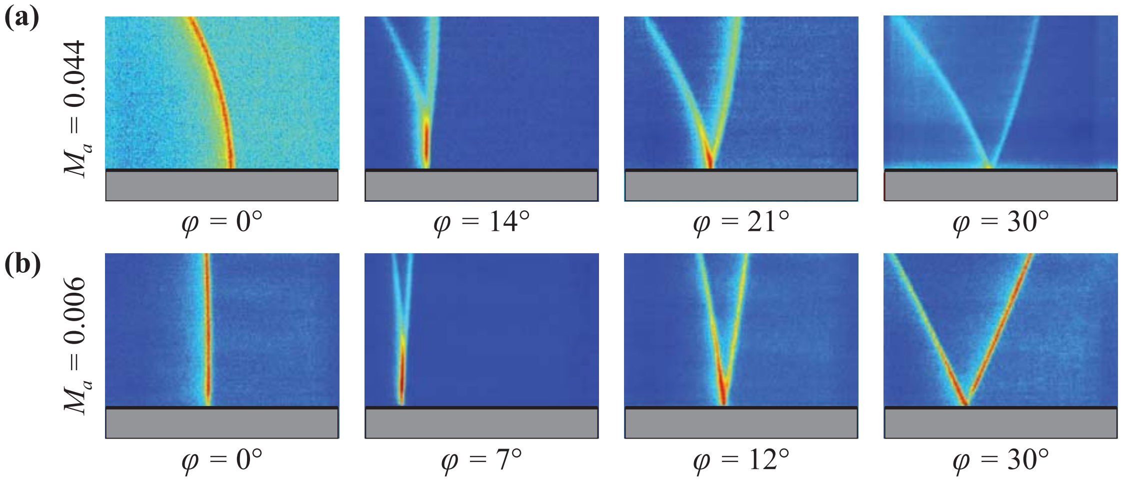

Figure 2.7: Optical visualization of a front shock reflection from a rigid surface. Reflection point is positioned $s = 4.6$ cm (a) and $s = 20.7$ cm (b) away from the spark source. The rigid surface is located in the bottom of each image; the wave propagates from left to right.

distance h under the spark. The emerging reflection pattern (4) was visualized using a schlieren method. The schlieren system was composed of a quartz tungsten halogen (QTH) continuous white light source (5) mounted in the geometrical focus of a spherical mirror (6) with 1m radius of curvature, a beam splitter (7), an optical knife (a razor edge, 8), and a high-speed Phantom V12 CMOS camera (9) with exposure time set to 1 μs. Light beam was transmitted through the beam splitter (7) and through the test zone of the acoustic pulse reflection. Then, the light reflected from the mirror (6), intersected the test zone once again, and propagated back to the beam splitter [orange solid lines with arrows in Fig. 2.6a]. Double passing of the light beam through the test zone provided better contrast of the image. Since the brightness of these images is proportional to the gradient of the acoustic pressure, they depict qualitatively the reflection pattern of the front shock of the pulse.

For visualizing the reflection pattern, an initial series of schlieren images was recorded without acoustic wave to obtain the averaged background image. A second series of images was recorded with the presence of acoustic wave. Raw images in the second series were dark and the front structure was not clearly seen without additional data processing. The averaged background image was subtracted from every recorded image of the reflection pattern; this subtraction resulted in reduction of noise and enhancement of the image contrast. An additional processing was the averaging of twenty images obtained from different sparks for a fixed source and reflection point configuration at the same h_{sp}, s, and φ (see Fig. 2.6a). In these images, the position of the reflection point varied by less than 5 mm and the reflection patterns were juxtaposed before averaging. Schlieren images [(19.5 ± 0.2) mm width × (12.2 ± 0.2) mm height] of the reflection patterns obtained in this way are presented in Fig. 2.7.

In order to investigate independently the effect of the pressure level and the incident angle φ on the reflection pattern, the position of the spark source was chosen so that the distance s between the source and the reflection point was the same for each angle φ considered in the study [Fig. 2.6a]. The results are given in Fig. 2.7 for two values of acoustic Mach number M_a (i.e., two distances s

Table 2.1: Experimental values of the critical parameter a for different types of reflection. Data were obtained for two distances from the spark source.

Experimental parameters		Weak von Neumann reflection	von Neumann reflection	Regular reflection
$M_a \times 10^{-2}$	4.4 ± 0.4	Probably occurs for $a \leq (0.38 \pm 0.05)$	$(0.38 \pm 0.05) < a < (1.05 \pm 0.15)$	$a \geq (1.05 \pm 0.15)$
$M_a \times 10^{-3}$	6.0 ± 0.3	Probably occurs for $a \leq (0.58 \pm 0.2)$	$(0.58 \pm 0.2) < a < (1.1 \pm 0.3)$	$a \geq (1.1 \pm 0.3)$

between the source and the reflection point) and different values of the incident angle φ. The series of frames in Fig. 2.7a was obtained at a distance $s = (46 \pm 4)$ mm away from the spark source, which corresponded to an acoustic pressure amplitude for the incident wave $p_0 = (6.2 \pm 0.5)$ kPa and a value of the acoustic Mach number $M_a = (0.044 \pm 0.004)$. To estimate the value of the acoustic Mach number its definition for the plane wave was used: $M_a = p_0/(\gamma p_{atm})$, where $\gamma = 1.4$ is the adiabatic index for air and $p_{atm} = 100$ kPa is the atmospheric pressure. For the series of frames in Fig. 2.7b, experimental parameters were $s = (207 \pm 7)$ mm, $p_0 = (0.84 \pm 0.04)$ kPa, and $M_a = (0.0060 \pm 0.0003)$. The coefficient of nonlinearity β was equal to 1.2 for the experimental conditions of the relative humidity of 49% and temperature of 292 K.

For the grazing angle ($\varphi = 0°$) the spark source was located right at the reflecting surface ($h = 0$). In this case no reflected shock was observed for both values of acoustic Mach number M_a (cases $\varphi = 0°$ in Fig. 2.7). The same pattern was achieved also for the angles $\varphi \geq 7°$ when $M_a = 0,044$ and for $\varphi \geq 5°$ when $M_a = 0,006$ (not shown here). Whether the absence of visible reflected shock is a confirmation of the weak von Neumann reflection regime or is the result of not enough sensitivity of the schlieren system still remains an open question. With further increasing the incident angle φ, one can clearly observe the irregular type of reflection with Mach stem formed close to the surface ($\varphi = 14°$ for $M_a = 0,044$ and $\varphi = 7°$ for $M_a = 0.006$). There were no visible slopes discontinuities between Mach stem and the incident shock which is a feature characteristic for von Neumann reflection. Then for $\varphi \geq 20°$ ($M_a = 0,044$) and $\varphi \geq 8°$ ($M_a = 0.006$) the regime of reflection is modified into regular reflection with incident and reflected shocks merged right at the surface [cases $\varphi = 21°$ and 30° in Fig. 2.7a; $\varphi \geq 12°$ and 30° in Fig. 2.7b]. Experimental values of the critical parameter $a = \sin\varphi/\sqrt{2\beta M_a}$ corresponding to each observed reflection regime are given in Table 2.1. Note that within experimental error the transition between the different reflection regimes occurs for similar values of the critical parameter a.

Both amplitude p_0 and grazing angle φ of the acoustic pulse change while the pulse propagates along the surface that leads to the change of the current value of the critical parameter a. As a result, the reflection pattern has a dynamic character changing with the propagation distance. This was confirmed in the experiment: the length of the Mach stem increased when the pulse propagated along the surface. For three consecutive schlieren images obtained at different distances from the spark along the surface (Fig. 2.8), both parameters M_a and φ were decreasing and therefore had different effect on the value of a. Increasing of the Mach stem length means that the value of a

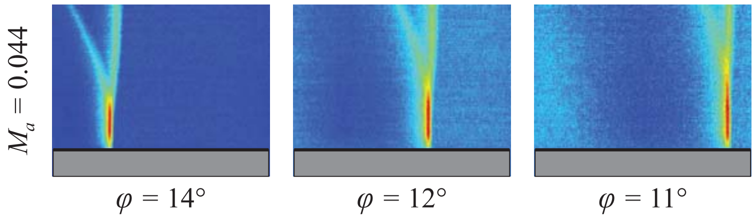

Figure 2.8: Three consecutive schlieren images from the high-speed camera obtained for the same position of the spark source ($\varphi = 14°$ and $M_a = 0.044$ for the first frame).

was decreasing and the variation of the grazing angle φ had stronger effect on a than the variation of the Mach number M_a.

Thus, the optical schlieren method provides visualization of the N-wave front shock reflection from the rigid boundary.Regular and irregular types of reflection were observed, and corresponding values of the critical parameter a for each reflection regime were determined. The rear shock of the spark-generated wave is less steep than the front shock, therefor it is more difficult to visualize it using the schlieren system.

Obtained in the experiment value $a = 1.1 \pm 0.3$ of the critical parameter corresponded to transition from regular reflection to irregular one is in agreement with the theoretical value $a = 0.8$ obtained in (Baskar *et al.*, 2007) by numerical modeling. Note that in (Baskar *et al.*, 2007) reflection of a plane N-wave was studied while in this experiment the wavefront was spherical and the waveform was asymmetrical in contrast to an ideal N-wave; thus the discrepancy between theory and experiment was supposed.

§2.4 Measurement of irregular reflection patterns using the Mach-Zehnder interferometry method

A Mach-Zehnder interferometer was used for quantitative measurements of reflection patterns formed in reflection of the N-wave from the rigid surface in air. The description of the experimental setup is given earlier in §1.5, where the Mach-Zehnder interferometry method is applied to measure N-waves in homogeneous air. The rigid surface made of plastic was located at distance $h_{sp} = 21$ mm below the spark source (Fig. 2.9). The reflection from the rigid boundary does not change radial symmetry of the wavefront in the plane parallel to the surface. Thus, the Abel inversion transform (1.18), required the spherical or cylindrical symmetry of the wavefront, remains applicable.

A reflection pattern measured using the Mach-Zehnder interferometer is shown in Fig. 2.10a for the case $l = 25$ cm, where l is a distance along the surface between a projection of a spark source on a surface and a reflection point (see Fig. 2.9b). This pattern represents the results of measured waveforms obtained at distances h from the rigid surface in the range from 2 mm up to 30 mm with increments of 2 mm. Pressure levels are indicated by colors. The abscissa is a time, thus a front shock of the N-wave coming earlier in time is left and the rear front is right. At each height h above the surface, 140 waveforms were recorded in order to allow statistical analysis

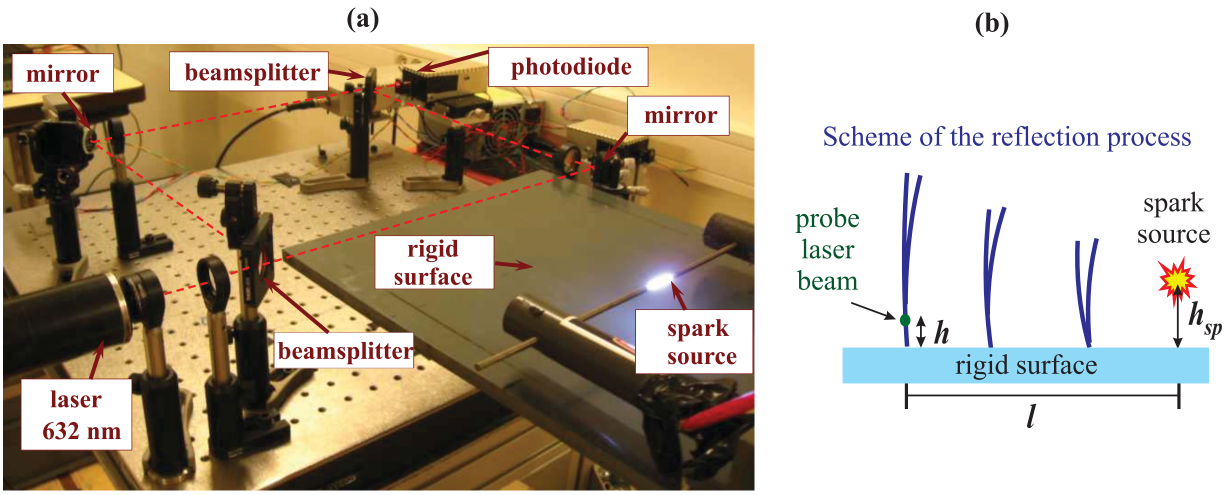

Figure 2.9: (a) Photo of the experimental setup based on the Mach-Zehnder interferometer. (b) The scheme of the side view on the reflecting surface.

of the data. "Average" waveform was selected from these 140 waveforms as a waveform with the arrival time, duration, and peak positive and peak negative pressures closest to their averaged values over all waveforms. It is clearly seen that the front shock of the N-wave is reflected from the surface in an irregular way. Only one front (the Mach stem) forms at distances $h \leq 6$ mm; starting at $h = 8$ mm, it splits into two fronts (of incident and reflected waves). The structure of the front shock in the vicinity of the triple point is shown in Fig.2.10b, where the Mach stem separation into two fronts is observed. It is clearly seen that the rear "shock" of the pulse is smoother than

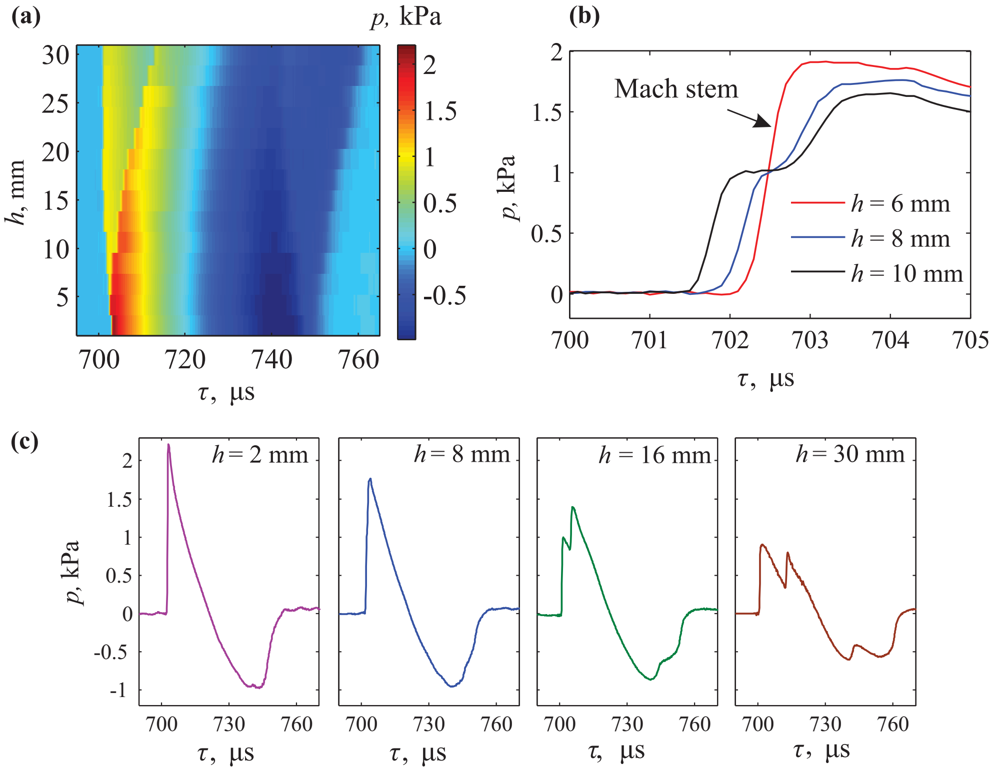

Figure 2.10: (a) Irregular reflection pattern obtained at distance $l = 25$ cm. (b) The zoom of the front shock structure for waveforms measured at different height h above the surface. (c) Waveforms at different height h from the surface.

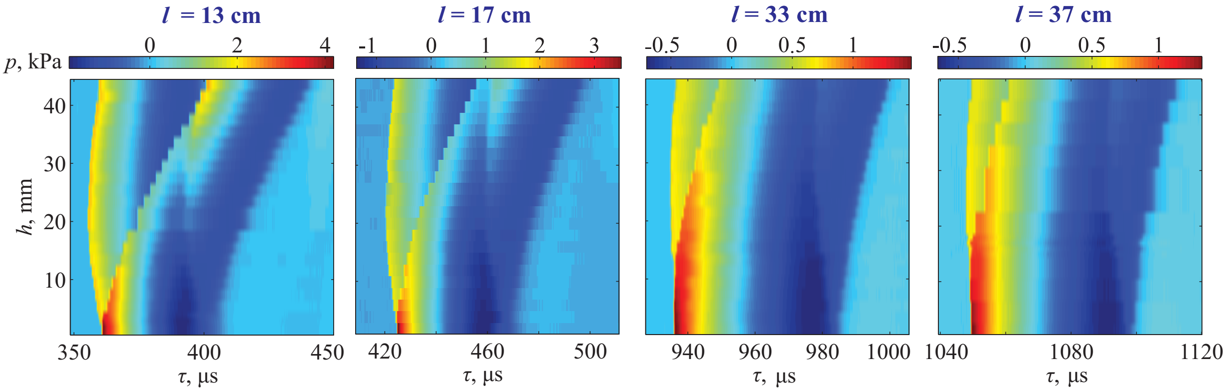

Figure 2.11: Irregular reflection pattern obtained at different distances l in irregular reflection of the N-wave form the rigid surface.

the front shock. This fact is crucial for the nonlinear effects and the reflection of the rear shock occurs in a regular regime (area $740 \leq \tau \leq 760$ in Fig. 2.10a). Pressure waveforms presented in Fig. 2.10c for different heights h above the surface show that the rear front of the pulse initially contains fronts of the incident and reflected waves (waveform at $h = 2$ mm) which subsequently diverge from each other (waveforms at $h = 16$ and 30 mm).

The pressure level close to the surface exceeds more than twice the amplitude of the incident shock front. In the case of linear reflection, the pressure is exactly doubled. Here, the pressure amplitude of the incident front is 1 kPa, which is clearly seen on waveforms at $h = 16$ and 30 mm when the incident front is already separated from the reflected one. The peak positive pressure close to surface is 2.3 kPa (waveform at $h = 2$ mm), i.e., pressure increases in 2.3 times.

Consider how reflection pattern changes while the N-wave reflects from the surface at its different points (Fig. 2.11). In schlieren experiments (Fig. 2.8), the structure of the front shock of the N-wave was visualized while measurements using the Mach-Zehnder interferometry method provides quantitative information about the entire structure of the field. In Fig. 2.11 one can see that the Mach stem is perpendicular to the surface and grows with the wave propagation along the surface. The reflection of the rear shock is regular.

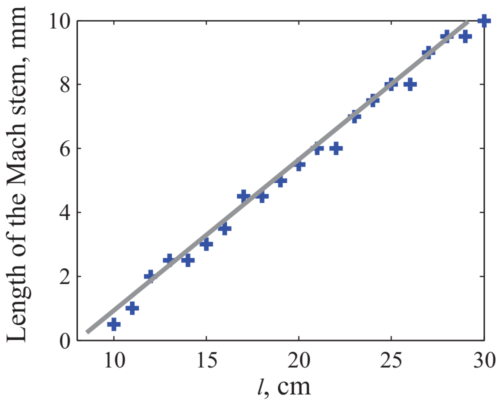

Figure 2.12: The trajectory of the triple point. Experimental points are shown by marker and a linear fit is shown by a solid line.

The using of the Mach-Zehnder interferometry method allows also measurements of the trajectory of the triple point (Fig. 2.12). One of the main features distinguishing the step shock reflection from the reflection of acoustic waves is a dynamical character of the irregular reflection for the last case (Baskar *et al.*, 2007). In experiment, irregular reflection of the pulse did occur in a dynamic way and the length of the Mach stem was increased linearly while the pulse propagated along the surface (Fig. 2.12). The linear interpolation of the triple point trajectory to the surface predicts that for current geometry configuration the transition between regular and irregular reflection occurs at $l = 8$ cm. Note that theoretical investigation of the plane N-wave reflection from the rigid boundary (Baskar *et al.*, 2007) predicts complicated nonlinear trajectory of the triple point. Here one could suppose that this linear dependence is a result of the wavefront sphericity and thus of a faster decrease of the energy on the front shock. Nevertheless, this linear dependance could be the initial region of more complicated nonlinear dependance.

§2.5 Nonlinear interaction between the reflected front shock of an N-wave and its incident rear shock

In reflection of the N-wave from the rigid surface nonlinear interaction between the incident and reflected shocks of the wave leads to the Mach stem formation near the surface. The spatial structure like a Mach stem can also be formed above the surface in the region where reflected front shock of the N-wave interacts with its incident rear front. Consider the reflection pattern obtained in the experiment in the case of $l = 13$ cm (Fig. 2.11). The overpressure area above the surface is clearly observed at hight $h \approx 4$ cm and $\tau \approx 400$ μs (yellow area in the figure). The structure of the fonts here is similar to the three-shock structure in irregular reflection; the difference is only in the Mach stem orientation. In order to understand the reason of overpressure area formation here, let one consider an evolution of waveforms with increasing height h above the surface (Fig. 2.13). Near the surface at the height $h = 2$ mm the waveform is a single pulse; shock front corresponds to the Mach stem and increasing of pressure in rarefaction phase corresponds to the incident and reflected rear fronts of the N-wave. With increasing of the height h the Mach stem divides into two fronts with the reflected front shock moving to the right on the waveform. At the same time parts of waveform correspond to the incident and reflected rear fronts of the N-wave become farther from each other. Incident rear front is moving contrary to the left. It is clearly seen how smooth rear front comes on the reflected front shock on waveform at $h = 36$ mm. Then there is their nonlinear interaction and merge into a single shock front (waveform at $h = 44$ mm) that is in fact the Mach stem. Note that the peak positive pressure of this front (2.1 kPa) is about the amplitude of the incident front shock and the waveform becomes similar to the two periods of the sawtooth wave.

Thus, the formation of the Mach stem in reflection of the N-wave from rigid surfaces can occur both near the surface and above the surface in the area where the incident rear shock intersect reflected front shock of the N-wave. In the case of the ideal N-wave there are two shock fronts in contrast to smooth rear front of spark-generated wave, therefore such interaction will be more pronounced.

§2.6 Conclusions

In this chapter, reflection of spherically divergent spark-generated pulses from the rigid surface in air was studied both by optical schlieren method and the Mach-Zehnder interferometry method.

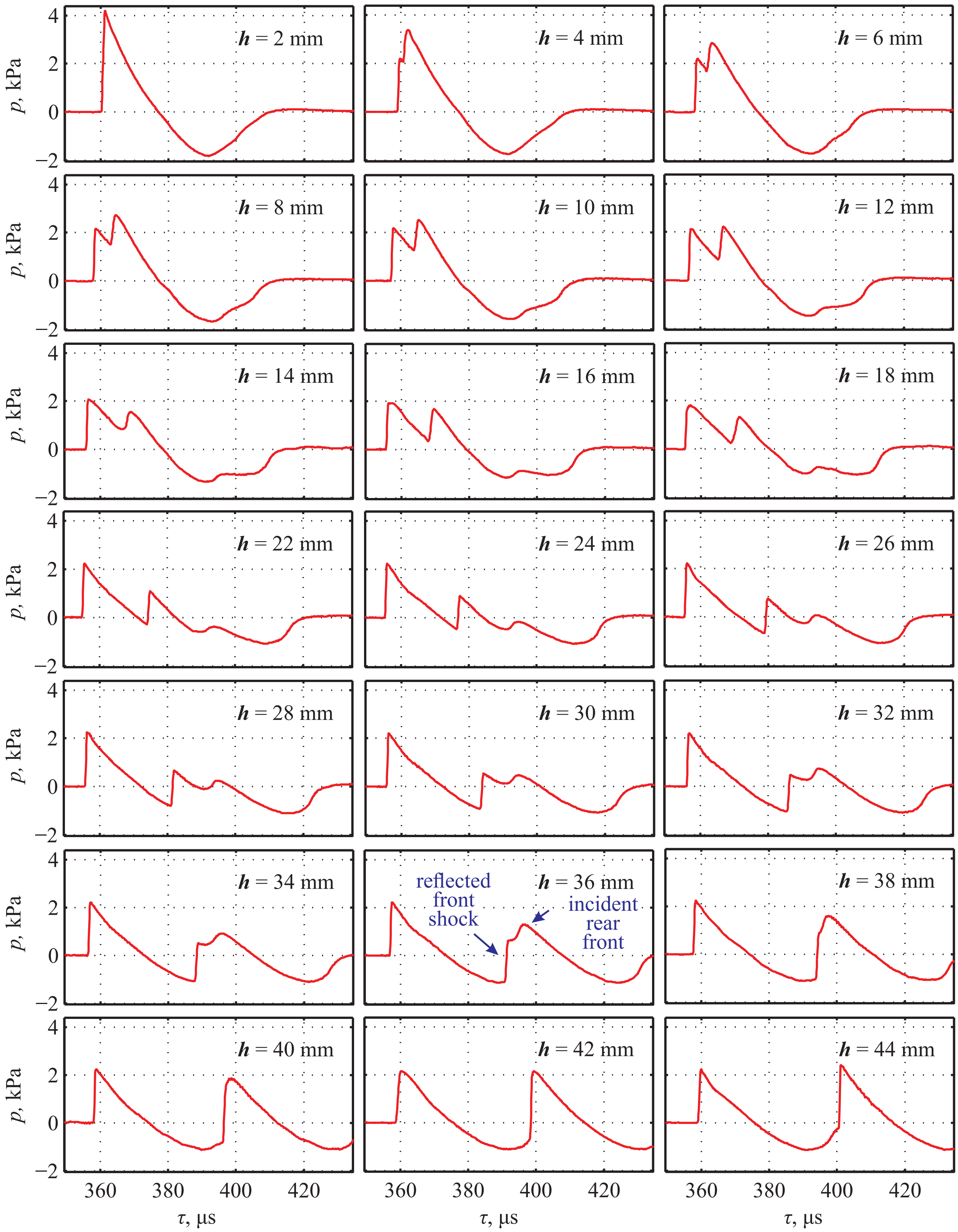

Figure 2.13: Pressure waveforms of N-waves measured by the Mach-Zehnder interferometer at different distances h above the rigid surface at distance $l = 13$ cm.

The optical schlieren method provides only visualization of reflection pattern structure while the Mach-Zehnder interferometry method allows to reconstruct pressure waveforms in the pattern by applying the inverse Abel transform to the phase of the measured signal. In experiments, dynamical irregular reflection was observed and the values of critical parameter correspond to different reflection regimes were found. It was shown that irregular reflection of pulses occurred in a dynamic way and that the trajectory of the triple point could be linearly interpolated within distances available in the experiment.

Chapter 3

Saturation mechanisms of shock wave parameters in pulsed and periodic high-intensity focused ultrasound beams

§3.1 Introduction

Focusing of high-intensity pulses and periodic waves is an important problem of nonlinear acoustics (Rudenko & Soluyan, 1977, Bailey *et al.*, 2003). The interest to this subject, in particular, is associated with a variety of medical applications of high-intensity ultrasound. Focused shock pulses are used, for example, in lithotripsy (Averkiou & Cleveland, 1999) for destruction of kidney stones while periodic sawtooth waves are used in noninvasive surgery to cause necrosis of soft tissue tumors (Hill *et al.*, 2002, Bailey *et al.*, 2003). The efficiency of these procedures is strongly dependent on the operational mode of a transducer, i.e., the number of generated pulses, their waveforms, amplitude, and duration. To select the most optimal operational mode it is necessary to be able to predict the parameters of generated fields and the biological effects caused by them. Also, formation of shock fronts occurred due to nonlinear effects should be taken into account. In the case of strong manifestation of nonlinear effects, the effect of saturation is observed: the acoustic field parameters at the focus of the transducer become not depending on the initial pressure amplitude (Rudenko, 1995, Rudenko & Sapozhnikov, 2004).

The mechanisms causing the saturation effect are different for periodic and pulsed fields. This leads to the fact that the limiting values of the acoustic field parameters are also different for periodic and pulsed modes of focusing. In medical applications often it is necessary to obtain a high value of the peak positive or negative pressure at the focus of the transducer. In a weak nonlinear case, it is enough to increase the pressure amplitude at the transducer. However, if the nonlinear effects are significant the increase of pressure amplitude at the source does not provide pressure increase at its focus due to the saturation effect. In this case, higher pressure amplitude can be obtained by using a signal with another temporal waveform.

In this chapter, a comparison of focusing efficiency for pulsed and periodic waves is performed as well as a comparison with existing analytical solutions. Nonlinear propagation of focused acoustic waves was studied using numerical simulations based on the Khokhlov-Zabolotskaya-

Kuznetsov (KZK) equation. In simulations, cases of a piston and Gaussian sources were considered. Physical mechanisms causing saturation effects in focused acoustic fields are determined.

Also in this chapter the qualitative analogy between physical processes occurring in the focusing of an axially symmetric beam and in reflection from plate rigid boundary is discussed. The spatial structure of wavefront in the focal area is considered similarly to the Mach stem formation in reflection of weak shocks considered in the previous chapter.

In this section, existing analytical approaches to evaluate the limiting pressure level at the focus are considered in cases of periodic and pulsed ultrasonic beams. Then, experimental results obtained by Kulkarny (Kulkarny, 1975) showing different spatial structures of waveforms at the focus are presented.

3.1.1 The saturation effect in the fields of periodic waves: a literature review

The saturation effect of the peak positive pressure in periodic fields exists already in the case of nonlinear propagation of a plane wave (Vinogradova *et al.*, 1979). Due to nonlinear effects, an initially harmonic wave becomes a sawtooth wave. Dependence of the peak positive pressure p_+ of a periodic wave at distance x from the source is given by a solution of simple wave equation

$$\frac{\partial p}{\partial x} = \frac{\varepsilon}{\rho_0 c_0^3} p \frac{\partial p}{\partial \tau} \tag{3.1}$$

and can be written analytically as

$$\frac{p_+}{p_0} = (1 + \frac{\varepsilon}{\rho_0 c_0^3} \omega x p_0)^{-1}. \tag{3.2}$$

Here ε is the coefficient of the nonlinearity of the medium , ρ_0 is the medium density, c_0 is the sound speed in an undisturbed medium, $\tau = t - x/c_0$ is the retarded time, and ω is a circular frequency of the periodic wave.

Infinity increase of the initial pressure amplitude $p_0 \to \infty$ leads to the saturation effect when the pressure amplitude p_{sat} at fixed distance x does not depend on p_0

$$p_{sat} = \frac{\rho_0 c_0^3}{\varepsilon \omega x}. \tag{3.3}$$

Here, the saturation effect of the peak positive pressure is occurred due to energy attenuation on formed shock front (Vinogradova *et al.*, 1979).

In focusing, the amplitude of the wave is increased, thus, nonlinear effects become more significant. Nonlinear effects can be pronounced differently depending on the frequency of the wave, its shape and amplitude and geometry of the transducer (Bessonova *et al.*, 2009). Combined effects of nonlinearity and diffraction can lead to different features of the acoustic field structure depending on manifestation of nonlinear effects. When the nonlinear effects are moderate and shock front formation doesn't occur or occurs close to focal area, the nonlinear enhance of peak positive pressure and intensity is observed at the focus (Naugolnykh K.A. & Romanenko E.V., 1959, Ostrovskii

& Sutin, 1975). This occurs due to the better focusing of higher harmonics and their relative phase shift caused by diffraction. In this case the peak negative pressure is less than it is predicted by the linear theory (Bessonova *et al.*, 2009). When nonlinear effects are strongly pronounced and the shock formation occurs close to the transducer, the nonlinear attenuation of the shock front becomes significant and leads to the saturation effect (Ostrovskii & Sutin, 1975,Bacon, 1984,Shooter *et al.*, 1974).

There are different analytical approaches to evaluate limiting values of the acoustic field parameters at the focus. The first approach was proposed by Naugolnykh and Romanenko in 1959 (Naugolnykh K.A. & Romanenko E.V., 1959). It is supposed that the spherical converging wave is propagating from the piston source to the sphere of radius r_F (Fig. 3.1). This wave is described by the generalized simple wave equation:

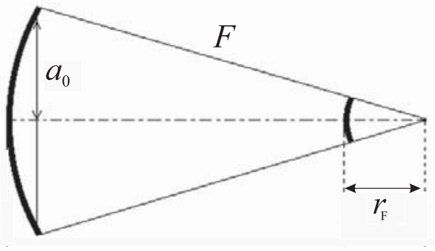

Figure 3.1: Geometry of the focusing.

$$\frac{\partial p}{\partial r} + \frac{p}{r} - \frac{\varepsilon}{\rho_0 c_0^3} p \frac{\partial p}{\partial \tau} = 0. \tag{3.4}$$

Here r is a coordinate and $\tau = t - r/c_0$ is a retarded time. Distance r_F is found in such way that the pressure amplitude of one-dimensional linear spherical converging wave at this point r_F will be equal to the pressure amplitude of linear focused beam at focus F (Fig. 3.2), described by a parabolic approximation of diffraction theory:

$$2ik\frac{\partial A}{\partial r} + \Delta_\perp A = 0, \tag{3.5}$$

where $p(r) = A(r)\exp(-i(\omega t - kr))$, $\Delta_\perp = \partial^2/\partial r^2 + \partial/r\partial r$ is a Laplace operator in the cylindrical coordinate system, $k = \omega/c_0$ is a wavenumber (Vinogradova *et al.*, 1979). The exact solution of Eq. (3.5) on the beam axis of the piston source is

$$A(r) = \frac{2A_0}{1 - r/F}\sin\left(G\frac{1 - r/F}{2r/F}\right), \tag{3.6}$$

while for Gaussian source it is

$$A(r) = \frac{A_0}{\sqrt{(1 - r/F)^2 + (r/F)^2/G^2}}, \tag{3.7}$$

where $G = ka_0^2/2F$ is linear enhance coefficient and a_0 is a transducer radius. In according to solutions of Eqs. (3.6) and (3.7), the amplitude at the geometrical focus is $A(r = F) = A_0 k a_0^2/2F = A_0 G$ (Fig. 3.2). Substituting this in equation describing linear propagation of spherical converging wave $\partial A/\partial r + A/r = 0$, for which $A(r) = G/r$, one obtains $r_F = F/G$. At this distance from the focus, the acoustic field is calculated for the one-dimensional nonlinear case (Eq. 3.4). For this variable substitutions $\tilde{P} = pr/p_0 F$, $\Theta = \omega\tau$ and $\sigma = (\varepsilon\omega p_0 F/\rho_0 c_0^3)\ln(F/r)$ are used to obtain

Eq. (3.4) in dimensionless form:

$$\frac{\partial \tilde{P}}{\partial \sigma} - \tilde{P}\frac{\partial \tilde{P}}{\partial \Theta} = 0. \tag{3.8}$$

This is a simple wave equation. The amplitude of sawtooth wave is given from this equation for regime of developed shock $\tilde{P} \approx \pi/(1+\sigma) \approx \pi/\sigma$ (Vinogradova *et al.*, 1979). Returning to the dimensional variables one obtains a dependence of sawtooth wave amplitude on distance r:

$$p = \frac{\pi \rho_0 c_0^3}{\omega \varepsilon r}\frac{1}{\ln(F/r)}. \tag{3.9}$$

Then for $r_F = F/G$ the pressure amplitude, i.e., the pressure in a saturation regime is

$$p_{sat} = \frac{\pi \rho_0 c_0^3}{\varepsilon \omega F}\frac{G}{\ln G} = \frac{\pi \rho_0 c_0^2}{2\varepsilon}\left(\frac{a_0}{F}\right)^2 \frac{1}{\ln\left(\omega a_0^2/2c_0 F\right)}. \tag{3.10}$$

One can see that the limiting pressure value p_{sat} depends on a geometry of the transducer (the angle a_0/F of focusing), parameters ε, ρ_0, c_0 of propagating medium, and the main frequency ω of a wave. With greater focusing angle and less frequency, greater limiting value of the pressure can be obtained.

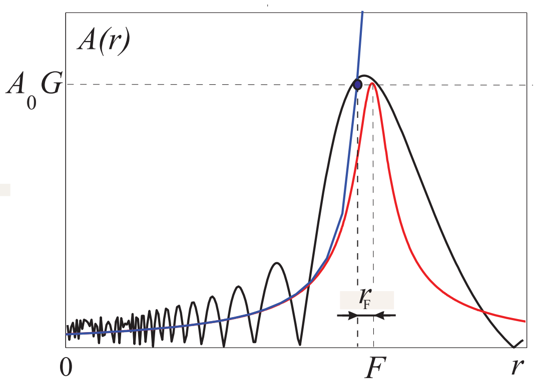

Figure 3.2: The amplitude of the harmonic wave as a function on the distance from the transducer along its axis in a case of linear propagation. Black color corresponds to piston source, red color - to Gaussian source, and the blue color - to spherical converging wave.

In effort of Ostrovskii and Sutin (Ostrovskii & Sutin, 1975) an approximate approach of alternative consideration of periodic wave focusing generated by piston source was applied. Initially, the approach considers only nonlinear focusing process neglecting diffraction effects. Then, starting at some distance close to focus, nonlinear effects are supposed negligible and only diffraction effects are considered. Next, in the focal area nonlinear effects once again prevail over diffraction effects and a nonlinear propagation of a plane wave is considered. According to this approach, the pressure maximum is achieved at a distance before the geometrical focus and equals

$$p_{sat} = \frac{2\rho_0 c_0^3}{\varepsilon \omega F}\frac{G}{\ln \eta}. \tag{3.11}$$

Here η is defined from equation $N p_{sh} \eta \ln \eta = 2\pi$, where $N = 2\pi\varepsilon p_0 F \omega/(\rho_0 c_0^3)$ is a nonlinear parameter and p_{sh} is a shock amplitude. Limiting values of the peak positive pressure obtained by using Eqs. (3.10) and (3.11) have the same order. In work (Ostrovskii & Sutin, 1975) the enhance coefficient of peak positive pressure was found to be more than four times greater than it would be in linear focusing.

Approaches proposed in works (Naugolnykh K.A. & Romanenko E.V., 1959) and (Ostrovskii & Sutin, 1975) allow the evaluation of the saturation pressure level for a piston source. However the model of Gaussian source is also widespread. In 1984, Bacon proposed an approach which allows to evaluate the limiting value of the peak positive pressure in the case of the Gaussian source (Bacon, 1984). In this approach one-dimensional propagation of nonlinear acoustic wave is considered in a tube whose walls are determined by localization of focused gaussian beam. The propagation of such beam is described by the nonlinear evolution equation

$$\begin{aligned} &\frac{\partial p}{\partial r} - \frac{\varepsilon}{\rho_0 c_0^3} p \frac{\partial p}{\partial \tau} + \frac{1}{2S}\frac{\partial S}{\partial r} p = 0, \\ &p(r=0) = p_0 \sin \omega_0 \tau, \end{aligned} \tag{3.12}$$

where $S = S(r) = \pi a_0^2 (1 + r^2/a_0^2)$ is a cross-sectional area of a tube given by a gaussian beam. Introducing new variables $\tilde{y}_1 = p\sqrt{S}$ and $\tilde{y}_2$ so that $d\tilde{y}_2 = dr/\sqrt{S(r)},\ \tilde{y}_2(r=0) = \tilde{y}_0$ and proceeding to dimensionless form, the first equation in (3.12) can be written in a form of a simple wave equation and as in a previous case, one can evaluate the saturation pressure

$$p_{sat} = \frac{\pi \rho_0 c_0^3}{\varepsilon \omega F} \frac{G}{\ln 2G}. \tag{3.13}$$

Eqs. (3.10), (3.11), and (3.13) provide similar values of the limiting pressure level at the focus. Moreover for large values of linear enhance coefficient $G \gg 2$ the limiting pressure levels obtained from all three equations will be the same.

As the nonlinear effects become more pronounced the saturation of the peak positive pressure occurs not only at the focus but also at some distances close to the transducer. This phenomenon was studied theoretically and experimentally in work (Shooter *et al.*, 1974) for converging and diverging spherical waves. Theoretical analysis in work (Shooter *et al.*, 1974) was performed using the Eq. (3.8) for spherical waves in regimes when the sawtooth wave is already formed. For each distance, the peak positive pressure of sawtooth wave was found as it was done in work (Naugolnykh K.A. & Romanenko E.V., 1959). The limiting value of the peak positive pressure at distance r_F coincided with the corresponding value obtained in (Naugolnykh K.A. & Romanenko E.V., 1959).

All considered above approaches for evaluating parameters of nonlinear focused acoustic fields neglect diffraction or account it separately from nonlinear effects, as it was done in work (Ostrovskii & Sutin, 1975). However, in focusing of high-intensity ultrasound waves used in medical applications combined effects of nonlinearity and diffraction should be taken into account simultaneously, especially in a focal area. A method, taking into account combined nonlinear effects and diffraction and allowed to find paraxial area of focused beams, was developed by Hamilton $et\ al.$ in (Hamilton *et al.*, 1997). The system of nonlinear eikonal and energy transfer equations describing distortions of wavefront due to nonlinear and diffraction effects was obtained. Analysis of the focusing gain G was performed using the KZ equation (Bakhvalov *et al.*, 1982). It was shown that until the shock front has not yet formed, nonlinear effects increase the focusing gain of the peak positive pressure due to more precise focusing of higher harmonics and phase shift between them caused by diffraction effects. At the geometrical focus the relation of the peak positive pressure p_+ to amplitude of the initial wave p_0 was found

$$\frac{p_+}{p_0} = G\left(1 + \frac{N}{2}\frac{(\pi/2G) - \ln(1/G)}{1 + (1/G)^2}\right) \sim G + NG^2. \tag{3.14}$$

As one can see, when diffraction effects (coefficient G) are fixed this relation linearly increases with increasing the amplitude of the initial wave (coefficient N). Note that Eq. (3.14) is applicable only for weak nonlinear waves until shock formation occurred.

Focusing of periodic waves generated by piston source and Gaussian source is studied in detail in works (Bessonova *et al.*, 2009, Bessonova O.V. *et al.*, 2009, Bessonova O.V. *et al.*, 2010) using the methods of numerical simulations based on the KZK equation (Bakhvalov *et al.*, 1982). In works (Bessonova *et al.*, 2009) and (Bessonova O.V. *et al.*, 2009) is was shown that existing analytical assessments (3.10), (3.11), and (3.13) provide underestimated values of the peak positive pressure. Increase of the pressure amplitude at the source leads to non monotonic change of the focusing gain: initially it increases (up to 3.5 times) then decreases. The maximum of the focusing gain is reached at such initial amplitude for which shock formation occurs at the focal area. The saturation of the peak positive pressure in the case of piston source reaches for less values of nonlinear parameter N, i.e., at lower initial pressure amplitude than it happens in the case of Gaussian source.

In the thesis, focusing of periodic fields was also studied using numerical simulations of the KZK equation as it was done in (Bessonova *et al.*, 2009, Bessonova O.V. *et al.*, 2009). This study was performed for further comparison with focused fields of shock pulses which were not studied using numerical methods before.

3.1.2 The saturation effect in pulsed fields: a literature review

Now consider approaches which are provided the evaluation of the limiting pressure values and field structures in pulsed fields. In contrast to periodic fields, in pulsed fields the saturation effect is not observed in one-dimensional case of nonlinear propagation of the plane wave (Vinogradova *et al.*, 1979). Solution of Eq.(3.1) for a single pulse with the shape of the N-wave is the following

$$\frac{p_+}{p_0} = \left(1 + \frac{\varepsilon}{\rho_0 c_0^3 T_0} x p_0\right)^{-\frac{1}{2}}, \tag{3.15}$$

where T_0 is a pulse duration. Peak positive pressure p remains dependant on the initial pressure amplitude p_0 even if the last one is infinitely increased $p_0 \to \infty$: $p = \sqrt{\rho_0 c_0^3 T_0 p_0 / \varepsilon x}$. Thus, nonlinear absorption of an energy on the developed shock is not enough to saturate parameters on the pulsed field in the case of plane wave propagation. However, saturation effects do exist if the pulsed field is focused.

In effort of Sapozhnikov *et al.* focusing of acoustic pulses generated by Gaussian sources is studied theoretically in a wide range of initial pressure amplitudes (Sapozhnikov, 1991). For weakly pronounced nonlinear effects analysis of nonlinear focusing was performed alternatively, as it was done in work (Ostrovskii & Sutin, 1975) for periodic fields. According to this approach the path of the wave was divided into two segments. On each segment either nonlinear effects or diffraction were negligible. Nonlinear effects were taken into account in the region between transducer and the focal area; here the wave was supposed to be a spherically convergent wave. In the focal area, wave supposed to be diffracted as a linear wave and nonlinear effects were not accounted. The size of the focal region was chosen so that the limiting transition to the linear case was carried out. In work (Sapozhnikov, 1991), it was shown that coordinate $r = F - r_F$ where $r_F = F/G$ is satisfied to this requirement (geometry is similar to shown in Fig. 3.1). Then, at the initial stage of propagation of the spherical converging wave its evolution can be expressed as an implicit function:

$$\frac{p}{p_0} = \frac{F}{F-r}\varphi\left(t - \frac{r}{c_0} + \frac{\varepsilon p}{\rho_0 c_0^3}(F-r)\ln\frac{F}{F-r}\right), \tag{3.16}$$

where function φ is a temporal waveform. After substituting $r = F - r_F$ pressure $p = p_F$ on the boarder of the focal region is

$$\frac{p_F}{p_0} = G\varphi\left(\tau + T_0\frac{p_F}{p_0}N\frac{\ln G}{G}\right), \tag{3.17}$$

where T_0 is an initial pulse duration. Then, solution (3.17) is used as a boundary condition to resolve linear diffraction equation for propagation in a focal area. According to (Vinogradova *et al.*, 1979) the solution of linear diffraction equation on the beam axis in parabolic approximation is

$$\frac{p}{p_0} = \int\limits_{-\infty}^{+\infty} \varphi(\tau')g(r,\tau-\tau')d\tau',$$
$$g(r,\tau) = \frac{1}{|1-r/F|}\frac{\partial}{\partial\tau}\left[H\left(\frac{\tau}{1-r/F}\right)\exp\left(-\frac{2rc_0\tau}{a_0^2(1-r/F)}\right)\right]. \tag{3.18}$$

Here $H(\tau)$ is a Heaviside step function. The temporal waveform of a pulse at the focal plane is found by expression (3.18), where instead of a_0 and F one should use $a_F = a_0 r_F/F$ and r_F, correspondingly, and function $\varphi(\tau)$ should be replaced by $p_F(\tau)/p_0$. Then the coefficient of the pressure enhancement will be given by

$$\frac{p_+}{p_0} = \frac{G}{1 - N\ln G}. \tag{3.19}$$

At $N = 1/\ln G$ the shock front is formed at the waveform on the boarder of the focal area. At the same time the coefficient of the pressure enhancement becomes infinite. It means that nonlinearity can not be neglected, i.e., the approach becomes unapplicable. Thus, estimation (3.19) is applicable only for weak nonlinear cases when $N < 1/\ln G$.

It was shown that linear diffraction does not limit the amplitude of shock waves. This limitation is due to effect of nonlinear refraction (Musatov *et al.*, 1992). Nonlinear refraction effect is caused by amplitude dependant velocity of the shock. The speed of the shock front is determined by the average pressure just before the shock front and behind it. Shock waves with greater amplitude propagate faster than shocks of lower amplitudes.

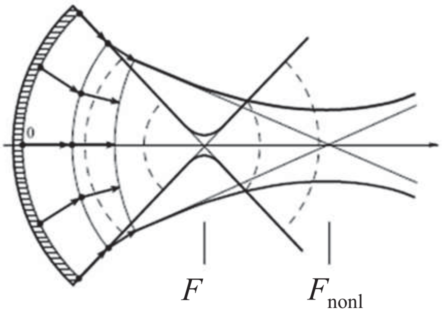

Figure 3.3: The effect of nonlinear refraction on the beam focusing - beam becomes defocused; focal area becomes wider and shifts from the transducer. The figure is taken from a review (Rudenko, 1995).

For Gaussian source the front velocity at the axis of the beam is greater than on its periphery. That leads to local defocusing of the beam and shift of the focal area (Fig. 3.3). The width of the focal area becomes wider than it would be in a linear case. Thus, for shock waves diffraction effects are less significant than nonlinear effects and focusing of pulsed fields could be described using ray approach. This approach was proposed by Sapozhnikov (Sapozhnikov, 1991). Two methods to find nonlinear rays for pulsed beams were applied to a pulse with a shape of isosceles triangle. In first method rays are lines perpendicular to shock front. Method of sequential approximations were used to find a ray pattern. Linear rays converging to a focus are used as a zero approximation. Along these rays the initial pulse is directed. Parameters of found pulses are used for a first approximation. Then normals are constructed to shock front and an initial pulse is propagated on new ray pattern, etc. For first approximation when the wave is supposed to be spherical the evaluation of the pressure amplitude p_{nonl} at the new nonlinear focus F_{nonl} where the wavefront becomes plane (see Fig. 3.3) is given by

$$\frac{p_{nonl}}{p_0} = \frac{F}{F_{nonl}}\sqrt{2}\left[1 + N\ln(\frac{F}{F_{nonl}})\right]^{-1/2}, \qquad (3.20)$$

where the coordinate of the front straightening F_{nonl} is found from

$$\frac{N}{G}\left(\frac{F}{F_{nonl}}\right)\ln\left(\frac{F}{F_{nonl}}\right) = \sqrt{2}\left(1 + N\ln\left(\frac{F}{F_{nonl}}\right)\right)^{1/2}. \qquad (3.21)$$

In this approach diffraction effects are supposed to be inessential. Also the effect of transverse amplitude distribution on waveform structure is evaluated. However, this approach does not take into account the inverse effect of waveform distortions on the pressure amplitude.

The second method taking into account this inverse effect is based on the assumption that before shock formation there is no nonlinear absorptions and triangular pulse propagates along linear rays (Sapozhnikov, 1991). After formation of the shock front at distance x_{sh} the pulse evolution is described by the simple wave equation with additional term accounting a tube section change Σ

$$\frac{\partial p}{\partial s} - \frac{\varepsilon p}{\rho_0 c_0^3}\frac{\partial p}{\partial \tau} + \frac{1}{2\Sigma}\frac{d\Sigma}{ds}p = 0. \tag{3.22}$$

Here $\tau = t - (s - s_1)/c_0$; s and s_1 are ray coordinate and its initial value, correspondingly. This approach takes into account the effect of the ray bending on the amplitude of the wave and provides equations to find the peak positive pressure p_+ at the focus:

$$\begin{gathered}
\frac{p_+}{p_0} = \frac{1}{p_0}\Phi(\frac{a}{a_0 f})\left[1 + \frac{N}{2F}\Phi(\frac{a}{a_0 f})\int\limits_{x_{sh}}^{x}\frac{dx'}{f(x')}\right]^{-1/2}, \\
f^2\frac{d^2 f}{dx^2} = \frac{N}{2F^2 G}\left(1 + \frac{N}{4F}\int\limits_{x_{sh}}^{x}\frac{dx'}{f(x')}\right)\left(1 + \frac{N}{2F}\int\limits_{x_{sh}}^{x}\frac{dx'}{f(x')}\right)^{-3/2}, \\
f|_{x=x_{sh}} = 1 - \frac{x_{sh}}{F}, \left.\frac{df}{dx}\right|_{x=x_{sh}} = -\frac{1}{F}.
\end{gathered} \tag{3.23}$$

Function Φ describes the amplitude distribution on the surface of transducer depending on transverse coordinate a. Eqs. (3.23) were obtained in assumption of aberration-free approximation of nonlinear geometrical acoustics and triangle waveform of the pulse. Eqs. (3.23) contain third-order differential equations not solved analytically. Nevertheless a solution can be found by using methods of numerical integration. This was done in work (Musatov *et al.*, 1992). The expression to estimate limiting value of the pressure in focused pulsed field was obtained

$$p_{sat} = 1.5 p_{in}\alpha^2, \tag{3.24}$$

where $p_{in} = \rho_0{}_0^2/2\varepsilon$ is inertial pressure in medium and $\alpha = a_0/F$ is a focusing angle. In dimensionless form it is

$$NP/G = 1.5, \tag{3.25}$$

where $P = p/p_0$ is dimensionless pressure amplitude, normalized on its initial value p_0. Thus, limiting value of pressure at the focus of Gaussian source generated pulsed field depends on only focusing angle α. This fact was confirmed in experiments (Musatov & Sapozhnikov, 1993a,Musatov & Sapozhnikov, 1993b).

In the thesis, the study of focusing of pulsed fields is performed for piston source and Gaussian source using methods of numerical simulations. Note that numerical simulation of focusing for shock pulses is a more complex problem in comparison with simulation of periodic waves, since it needs more calculation resources. In particular, for the same time and spatial steps of a grid, simulation of pulsed signals requires the use of greater time window (more than ten times greater even in a case of weak nonlinearity) than it is needed for periodic fields simulation. This leads to an increase of the random access memory necessary for calculation and a corresponding increase of calculation time even in the case of linear propagation. Numerical simulations of nonlinear focusing of pulsed fields became possible only lately due to the rapid progress of computing machinery and methods of parallel computing.

3.1.3 The structure of wavefronts at the focal area

Consider the focusing of an axial-symmetric beam as a process in which the upper half of the beam reflects from an axis of symmetry. Such consideration is correct from a mathematical point of view since boundary conditions on the beam axis and on reflecting rigid surface are the same: the normal derivative of the pressure in the transverse coordinate is equal to zero. Consideration of focusing as a process similar to reflection is also in agreement with physical nature. Such consideration is used, for example, in optics and electrostatics in method of mirror images. Then it is logical that the Mach stem formation is observed not only in reflection from rigid surfaces but also in focusing of axial-symmetric beams, at least in a case of small focusing angles and strongly nonlinear beams.

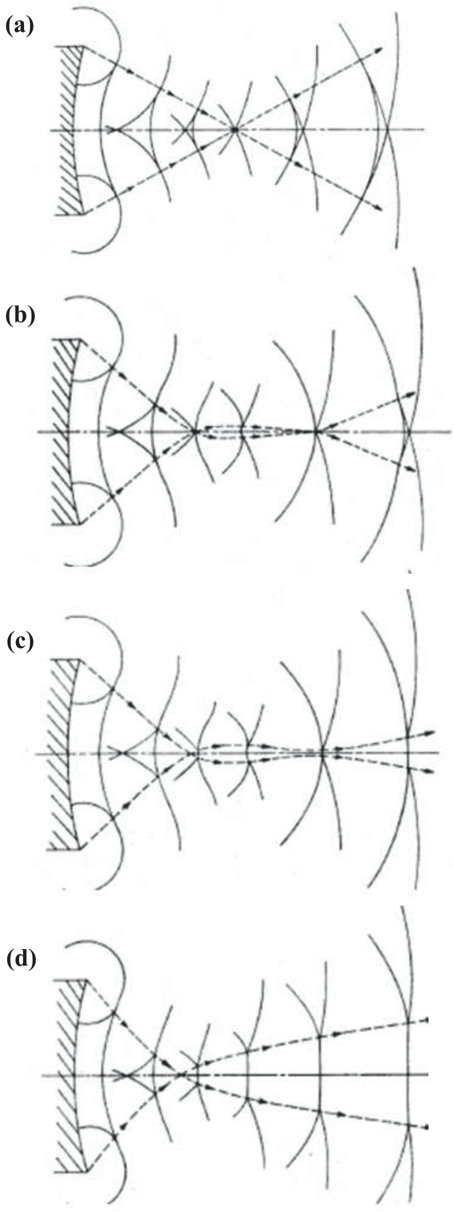

Figure 3.4: Wavefront geometry in focusing of shock waves with different Mach numbers. (a) Linear focusing, (b) focusing of weak shock ($M_a \sim 10^{-2}$), (c) focusing of moderately strong shock ($M_a \sim 10^{-1}$), (d) focusing of strong shock ($M_a \sim 1$). The figure is taken from PhD thesis (Kulkarny, 1975).

One of the few efforts to consider the Mach stem formation in focusing of shocks was performed by Kulkarny (Kulkarny, 1975). To generate focused step shocks he used a shock tube with a parabolic reflector on its edge. The shadowgraphy method was used for optical visualization of wavefront structures. The experiment was conducted in air in the range of acoustic Mach numbers $5 \cdot 10^{-3} \leq M_a \leq 5 \cdot 10^{-1}$. For $M_a \sim 10^{-3}$ linear focusing regime was observed as it is shown in Fig. 3.4(a). The intersection of the central wave and the edge wave occurs exactly at the focus. As the value of acoustic Mach number increases up to $M_a \sim 10^{-2}$ velocity of both central and edge waves is also increases and front interaction occurs closer to reflector [Fig. 3.4(b)]. The focal area becomes cigar shaped. In a paraxial area the Mach stem starts to form. With further increase of acoustic Mach number the focal area moves towards to reflector [Fig. 3.4(c),(d)]. The structure of fronts at the focal area resembles to the one observed in a case of strong shock reflection from a rigid boundary.

Note that Kulkarny performed his experiment in the 70s when reflection of weak shocks in a framework of the von Neumann paradox has not been relevant. Perhaps, this was a reason why the experiment failed to observe the case when the Mach stem formed at $M_a \sim 10^{-3}$. More sensitive to the pressure gradients optical system was necessary for that. Shadowgraphy method realized by Kulkarny did not have sufficient sensitivity to such visualizations.

Later, the focusing of weak shock waves has been studied numerically in (Tabak & Rosales, 1994), but only step shock cases were considered. As it was mentioned above, acoustical waves have more complicated waveforms than step shocks, thus focusing of acoustic weak periodic and pulsed shocks still remains relevant.

For Mach stem formation, two shocks should interact. In the case of reflection they are incident shock and reflected one, in focusing – shocks of the central wave and the edge wave. Interaction between shock fronts of the periodic wave was studied numerically and compared with experimental results in work (Khokhlova *et al.*, 2001). Unfocused harmonic wave radiated by intense continuous wave source with an oscillated near field was considered. It is shown that if a shock formation occurs in a penultimate maximum of peak positive pressure distribution on the axis then the center wave will interfere with the edge wave. Since the edge wave has reversed waveform, the shock formation in its waveform occurs in another position. Thus, formation of two shocks in each cycle of an initially harmonic wave, followed by their motion towards each other and further collision, is observed. In (Khokhlova *et al.*, 2001) interaction of shocks were considered in time domain on the beam axis. The structure of wavefronts on the paraxial area potentially containing the Mach stem was not considered. In the thesis of Bessonova the example of such structure is demonstrated but it was not considered as the Mach stem formation (Bessonova, 2010).

In this thesis, numerical simulations revisiting the classical problem of shock wave focusing under the light of Mach stem formation are performed. The model is based on a KZK equation for axially symmetric nonlinear beams. In subsection §3.5 results are presented for piston source and the possibility of the Mach stem formation in a focal area of medical transducers is discussed.

§3.2 Numerical model based on the KZK equation

The nonlinear propagation of high-intensity acoustic signals generated by focused sources is described here using the KZK equation. The equation takes into account the combined effects of nonlinearity, diffraction and absorption. For the axisymmetric beams the equation can be written in dimensionless form as

$$\frac{\partial}{\partial \Theta}\left[\frac{\partial P}{\partial \sigma} - NP\frac{\partial P}{\partial \Theta} - B\frac{\partial^2 P}{\partial \Theta^2}\right] = \frac{1}{4G}\left(\frac{\partial^2 P}{\partial \rho^2} + \frac{1}{\rho}\frac{\partial P}{\partial \rho}\right), \tag{3.26}$$

where $P = p/p_0$ is the acoustic pressure normalized by the initial amplitude p_0 at the transducer; $\sigma = x/F$ is the propagation distance normalized by the transducer focal length F; $\rho = r/a_0$ is the lateral distance normalized by the transducer radius a_0; $\Theta = 2\pi\tau/T_0$ is the dimensionless time; $\tau = t - x/c_0$ is the retarded time; T_0 is the signal duration (for the harmonic wave it equals to one period). Equation (3.26) contains three dimensionless parameters: $N = 2\pi F\varepsilon p_0/\rho_0 c_0^3 T_0$ is the nonlinear parameter, where ε is the coefficient of medium nonlinearity, $G = \pi a_0^2/c_0 F T_0$ is the diffraction parameter and B is the absorption parameter.

The initial pressure amplitudes of the harmonic wave and the pulse are chosen so that in the case of linear focusing the shape and the peak positive pressure P_+ amplitude of both signals at the transducer focus are the same (Fig. 3.5). A harmonic wave was selected as the initial periodic signal

$$P_0\left(\Theta\right) = \sin\Theta. \tag{3.27}$$

The pulsed regime is presented by a sequence of pulses with low pulse-repetition frequency. The shape of each pulse is a single period of a harmonic wave and the pressure between pulses was taken to be constant. In this case the signal value average over the time window was zero

$$P_0\left(\Theta\right) = \begin{cases} 1 - 1/n_0 - \sin\Theta, & \pi/2 \le \Theta \le 5\pi/2, \\ -1/n_0, & \Theta \le \pi/2 \ \ and \ \ \Theta \ge 5\pi/2, \end{cases} \tag{3.28}$$

where $2\pi n_0$ is the length of the time window and n_0 is the integer number. In the case of $G = 10$ the value $n_0 = 13$ was used for a Gaussian source and $n_0 = 30$ was used for a piston source. These initial conditions are convenient for comparison of the periodic wave focusing and focusing of single pulses in the nonlinear case.

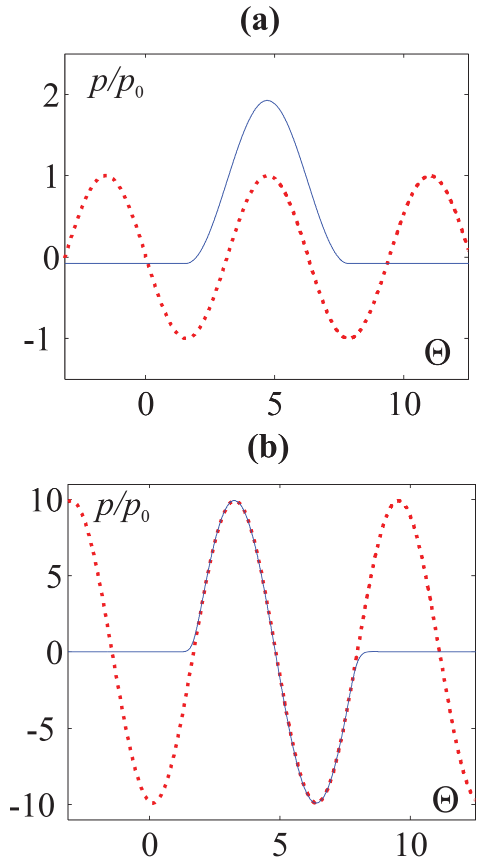

Figure 3.5: Initial waveforms on the transducer (a) and waveforms in its focus (b) in the case of linear focusing with $G = 10$. The harmonic wave is presented by the dashed curve, and pulse - by the solid curve.

The boundary condition was set in the plane $\sigma = 0$ and corresponded to a circular focused source with either Gaussian spatial apodization(3.29) or with uniform pressure amplitude distribution (3.30). Focusing of the beam is provided by a phase shift, which increases quadratically with the transverse coordinate ρ

$$P\left(\sigma = 0, \rho, \Theta\right) = P_0\left(\Theta + G\rho^2\right)\exp(-\rho^2), \tag{3.29}$$

$$P\left(\sigma = 0, \rho, \Theta\right) = \begin{cases} P_0\left(\Theta + G\rho^2\right), & \rho \le 1, \\ 0, & \rho > 1. \end{cases} \tag{3.30}$$

The equation (3.26) with boundary conditions (3.29, 3.30) and initial waveforms (3.27, 3.28) was solved numerically using a combined time-domain and frequency-domain approach based on a method of splitting in physical factors. Diffraction effects are calculated in the frequency domain using the Crank-Nicholson algorithm of the second order of accuracy over both spatial coordinates (Bessonova O.V. *et al.*, 2009). Absorption effects are taken into account using the exact solution for harmonics in the frequency domain (Filonenko & Khokhlova, 2001). Nonlinear effects are calculated in the time domain using the Godunov-type conservative numerical algorithm, which is capable to model the propagation of nonlinear waves even in case if only 3-4 time grid points per shock are present (Kurganov & Tandmor, 2000). Transition between spectral and time domains is carried out using the fast Fourier transform. The algorithm was adapted for parallel computation with the help of the OpenMP technology, which provided an opportunity to reduce significantly the calculation time.

The parameters for the numerical scheme were chosen based on the condition of stability for a numerical algorithm and a preset accuracy of calculation (2%). The calculation accuracy was estimated by comparison of solutions obtained for steps of discretization differing twice. If solutions differed by less than 2% than the discretization step was taken to be equal to the current one. For the Gaussian source there are no strong pressure gradients along both transverse ρ and lateral σ coordinates; thus, grid steps are chosen greater than in the case of piston source. For the Gaussian source, diffraction step along the propagation coordinate was $h\sigma = 10^{-3}$ and the step in the transverse coordinate was $h\rho = 4.06 \cdot 10^{-4}$. To satisfy the Kurant-Friedrichs-Levi condition for the Godunov-type scheme several steps over nonlinearity were performed within each diffraction step along the propagation coordinate. The nonlinearity step was h_{nonl} was selected automatically at each diffraction step $h\sigma$ and varied within the range $7 \cdot 10^{-5} \leq h_{nonl} \leq 3 \cdot 10^{-4}$. For a piston source the step along propagation coordinate was reduced up to $h\rho = 1 \cdot 10^{-4}$ for pulsed field; other steps were similar to used in the case of Gaussian source. For periodic field of the piston source steps were chosen $h\sigma = h\rho = 5 \cdot 10^{-5}$.

The time step of numerical grid or the number of the harmonics taken into account in calculation were also varied with propagation coordinate. Initially, 128 harmonics were taken into account for a periodic wave and 8192 for a pulse. This number of harmonics was sufficient to describe focusing with the selected precision in linear and weakly nonlinear cases ($N < 0.1$). The number of accounted harmonics was increased with the propagation coordinate since the wave became steeper. In a focal area 2048 harmonics were accounted for a periodic wave and 8192 for a pulse in the case of Gaussian source while 16384 were used in a pulsed bean produced by the piston source. Thus the minimal time stem was equal to $ht = 5 \cdot 10^{-3}$ and $ht = 1.5 \cdot 10^{-3}$ for a pulsed and periodic fields, correspondingly. Artificial absorption to smooth large field gradients in transverse directions leading to algorithm divergence was introduced (Bessonova O.V. *et al.*, 2010). Its value was selected from the condition for at least seven nodes of the time grid to fit a shock front at the focus. In this case the absorption was small in near field and increased with the propagation coordinate. In a focal area, the artificial absorption increased up to tenfold at $G = 10$ and 40 times at $G = 40$. The minimum value of the absorption coefficient was $B = 5.4 \cdot 10^{-3}$.

In numerical simulations, a priori knowledge about focusing geometry was used. For example, in a focal area the calculation along the transverse coordinate was performed only over the region where the peak positive pressure exceeded 0.06% of its maximum value.

§3.3 Effect of a signal waveform on limiting values of shock wave parameters in nonlinear focused beams

For numerical simulation of focused beams the following parameters in the equation (3.26) were chosen: $G = 10$; 20; 40; $0 \leq N \leq 6$. The peak pressure of $p_0 = 6\ MPa$, pulse duration of $T_0 = 4\ \mu s$, an effective reflector radius $a_0 = 77$ mm, and an effective focal distance $F = 128$ mm are typical for the Dornier HM3 lithotripter (Averkiou & Cleveland, 1999) and correspond to the dimensionless parameters $G = 14$ and $N = 1.4$. In the thesis most of the results are presented for $G = 10$ and $N = 1.0$, which are close to the values, typical for the fields of clinical shock-wave lithotripters. These values are also typical for medical transducers used in noninvasive surgery of soft tissues (Hill *et al.*, 2002).

Among the most important parameters of acoustic field are the peak positive P_+ and peak negative P_- pressures at the focus of the transducer. The peak positive pressure of shock wave determines the mechanical and thermal effects while the peak negative pressure is responsible for cavitation. In a case of linear propagations, P_+ and P_- at the focus are the same for periodic wave and the pulse (Fig. 3.5). Results of numerical simulations show the difference which occurs in the nonlinear case.

Figure 3.6 presents two-dimensional patterns of spatial distributions for the peak positive (a, b) and peak negative (c, d) pressures in a nonlinear beam ($G = 10$, $N = 1.0$) for periodic (a, c) and pulsed (b, d) fields of Gaussian transducer. The distance $\sigma = 1$ corresponds to the geometrical

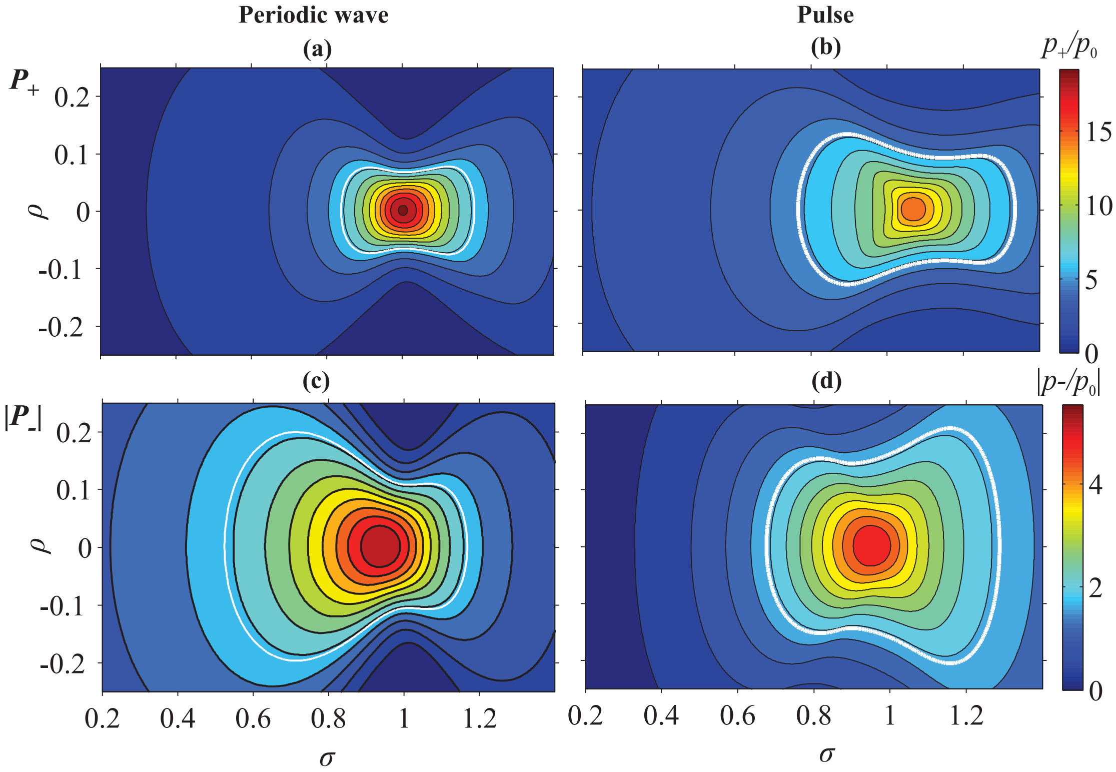

Figure 3.6: Two-dimensional spatial distributions for the peak positive (a, b) and peak negative (c, d) pressures in periodic (a, c) and pulsed (b, d) focused fields ($G = 10$, $N = 1.0$). White contours show the boundaries of focal areas. Color indicates the levels of the pressures.

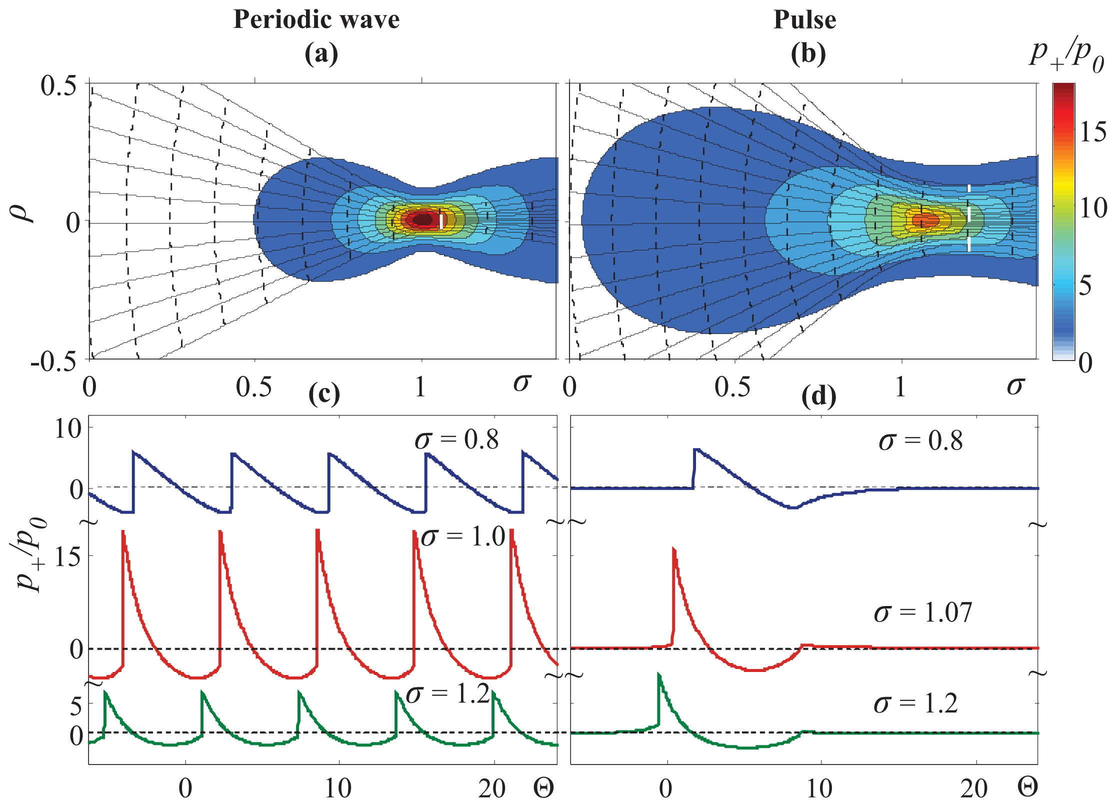

Figure 3.7: The upper series: ray patterns for periodic (a) and pulsed (b) fields. Rays are shown by solid lines and shock fronts – by dashed lines. The white dashed line indicates the front position at the point of its straightening in the paraxial area. Colors indicate levels of the peak positive pressure ($G = 10$, $N = 1.0$). The lower series: waveforms at the source axis of Gaussian transducer at different distances σ in the cases of periodic (c) and pulsed (d) fields.

focus of the transducer which is located at $\sigma = 0$. One can see clearly that greater values of both peak positive and negative pressures are achieved in a periodic field in comparison with the corresponding values in a pulsed field. At the same time, the focal region of the peak positive pressure in a periodic field is more compact in both longitudinal and transverse directions. In Fig. 3.6 the size of the focal region is determined at e^{-1} level of the maximum peak pressure in each case and indicated by a white contour. One can see that focused periodic fields are preferable for achieving the highest peak positive and peak negative pressures at the focus of the transducer than pulsed fields.

The focal area of P_- is shifted toward to transducer for both periodic and pulsed fields ($\sigma = 0.95$) that should be taken into account in describing the cavitation effects. The focal area of P_- has a non symmetrical shape in the form of a dumbbell. For periodic field it has bigger size in the direction to the source (Fig. 3.6c) while for a pulsed field asymmetry manifests in the opposite direction [Fig. 3.6(d)]. This difference is due to the fact that there is no rarefaction phase in the initial pulse profile. It appears only far from the source due to manifestation of diffraction effects.

Figure 3.7 presents ray patterns for periodic (a) and pulsed (b) fields in the case of Gaussian source with $G = 10$ and $N = 1.0$. A dashed line indicates wave fronts that were determined at each spatial point according to the maximum of the derivative from a waveform at this point. Solid lines indicate rays plotted as perpendicular to wave fronts in dimensional coordinates. Let us to call the location of the maximum for the peak positive pressure P_+ as a focus of the transducer. For a periodic field, the maximum of P_+ is achieved approximately at the geometrical focus of the source ($\sigma = 1.0$). In pulsed fields, the maximum of P_+ is reached behind the geometrical focus at $\sigma \approx 1.1$. In the linear case, the maximum of the peak positive pressure for periodic and pulsed fields is attained shifts to at $\sigma \approx 0.98$ due to diffraction effects (Rudenko & Soluyan, 1977). Thus, the location of the focus is different in cases of linear and nonlinear focusing and depends on temporal structure of the signal. Shift of the focus in high-intensity pulsed fields is caused by nonlinear refraction which is pronounced stronger in pulsed fields than in periodic ones. This is due to the fact that the shock front formed in an initially harmonic wave stays almost symmetrical with respect to zero up to the focus and its velocity is almost unchanged.

Waveforms on the axis of the beam at different distances σ from the transducer are presented in Fig. 3.7(c) for a periodic field. At $\sigma = 0.8$ a periodic waveform is still symmetrical with respect to zero, i.e., the front velocity in the traveling coordinate system is close to zero. The pulse profile at the same distance σ [Fig. 3.7(d)] is non symmetrical with zero pressure just behind the shock front. Therefore, the shock front of a pulse propagates faster than the front of a saw-tooth wave. Thus, the phenomenon of nonlinear refraction manifests strongly for a pulsed field than a periodic one. The effect of nonlinear refraction in periodic fields is significant only in the focal region, where the waveform becomes asymmetrical (a waveform at $\sigma = 1.0$). For pulsed fields the effect of nonlinear refraction becomes significant immediately after shock front formation. The waveforms shown at $\sigma = 1.0$ and $\sigma = 1.07$ correspond to foci of periodic (c) and pulsed (d) fields, correspondingly. As one can see, the maximum pressure in the periodic field is higher than in pulsed field and the pulse duration exceeds duration of a single period of a periodic wave. After passing the focus (waveforms at $\sigma = 1.2$), pressure in both periodic and pulsed fields decreases and the shock front in the traveling coordinate system is shifted to the left (i.e., it arrives earlier than a linear wave would) because of the combined influence of nonlinear refraction and diffraction effects.

The white dashed lines in Fig. 3.7(a,b) indicate wavefronts when they become plane in the paraxial area. The straightening of wavefronts occurs behind the focus and the wavefronts are still converging in the region, where maxima of the peak positive pressures are reached. Wavefront straightening in a pulsed field occurs farther from the focus than in a periodic field. This is also caused by the phenomenon of nonlinear refraction, which pronounces weaker in periodic focused beams than in pulsed ones.

The characteristic distortion of waveforms at the focus at different values of the nonlinear parameter N can be observed in Fig. 3.8(a,b). The front position of a periodic wave changes insignificantly, while the pulse front becomes strongly shifted to the left because of nonlinear refraction. As the nonlinear parameter N grows, the pulse duration increases while the duration of one period on a periodic wave does not change but the initially harmonic wave becoming a saw-tooth wave. At the value of linear focusing gain $G = 10$ a shock front formation in focal waveform in both periodic and pulsed fields occurs at $N = 0.5$. In a weakly nonlinear case (at $N < 0.5$) the peak positive pressure in pulsed and periodic fields grows with the increase of the nonlinear parameter N and then decreases after formation of a shock front (at $N > 0.5$) due to nonlinear absorption. Before formation of a shock front (at $N < 0.5$), the compression phase of a pulse is shortened and then at $N > 0.5$ lengthened vice versa. The rarefaction phase of a pulse is lengthened monotonically with the increase of N. In a periodic wave, the compression phase becomes shorter and the rarefaction phase becomes longer as nonlinear effects become stronger. Nevertheless, these changes are pronounce much more weakly in comparison with the pulsed case.

Figure 3.9a presents saturation curves for the peak positive pressure in periodic and pulsed fields of Gaussian source. Saturation curves for a periodic field are shown in dashed lines and for a pulsed field in solid lines. Let one to assume that saturation is achieved starting from the moment at which the derivative of a saturation curve is 5% of its maximal value. In this case for a periodic field saturation of the peak positive pressure occurs at $N = 5$ and for a pulsed field, at $N = 1.5$. Thus saturation in pulsed fields occurs earlier than in periodic fields, i.e., at smaller values of the nonlinear parameter N and therefore at smaller values of pressure amplitude on the source. In a weakly nonlinear case (at $N < 0.5$) saturation curves for periodic and pulsed fields are close to each other; i.e., the fields have close values of positive and negative pressures (Fig. 3.9a,b). At large values of the nonlinearity coefficient N, the peak positive pressure and the modulus of the peak negative pressure in a periodic field are larger than in a pulsed field. Saturation for the peak negative pressure is not observed in the interval of studied parameters N (Fig. 3.9b).

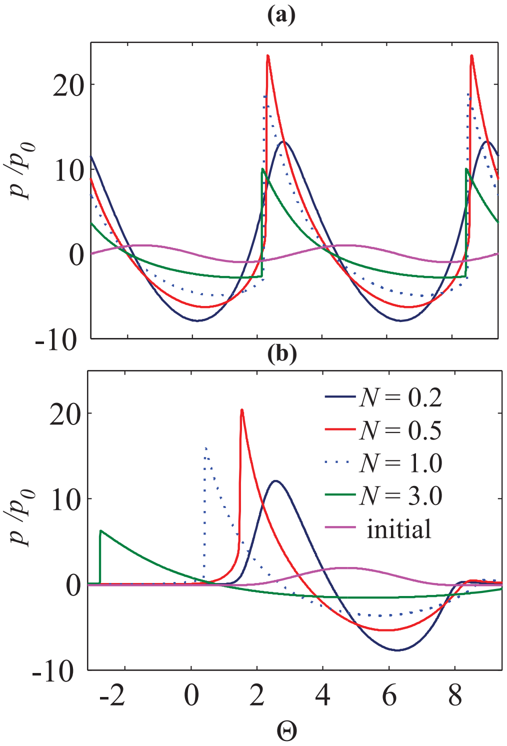

Figure 3.8: Waveforms at the focus (at the location of the maximum of the peak positive pressure) for periodic (a) and pulsed (b) signals with $G = 10$ and different values of the nonlinear parameter $N = 0.2$, 0.5, 1.0, and 3.0. Solid pink lines show waveforms at the source.

As one can see from Fig. 3.9(a), in the case of saturation for the peak positive pressure in pulsed fields, the numerically calculated coefficient $NP_+/G \approx 1.9$. Thus in pulsed fields the limiting peak positive pressure level predicted by Eq. (3.25) is $\approx 20\%$ smaller than the one obtained by numerical simulations taking into account diffraction effects. Note that the saturation level of the peak positive pressure does not depend on value of G, i.e., on the initial duration of the pulse. Similar phenomenon was predicted by Eq. (3.24).

Analytical expression (3.13) for peak positive pressure at the focus of periodic fields can be written in a dimensionless form as

$$NP_+/G = \frac{\pi}{\ln{(2G)}}. \tag{3.31}$$

The values of saturation pressure obtained using this formula for different values of the linear focusing parameter G are shown in different colors at the right from the legend in Fig. 3.9(a). As one can see, at $N = 6$ the approximate formula of Eq. (3.31) gives a pressure value approximately three times smaller than the one obtained in numerical calculation for a periodic field.

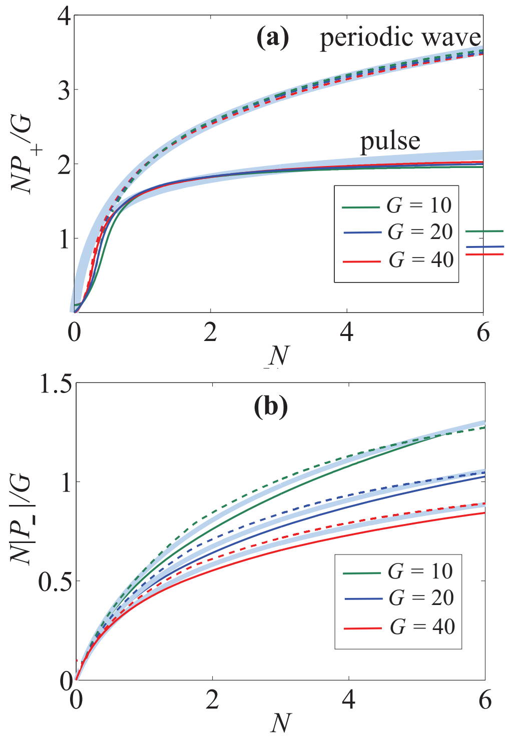

Figure 3.9: Saturation curves for the peak positive (a) and negative (b) pressures. Dashed lines correspond to the dependencies for a periodic field and solid lines - to a pulsed one. Thick light-blue lines show the saturation curves plotted using the approximations given by Eqs.(3.32)-(3.34). In the plot (a) at the right from the legend different colors indicate saturation levels calculated using the analytical solution given by Eq.(3.31).

Since saturation curves for the peak positive pressure [Fig. 3.9(a)] in periodic and pulsed fields turned out to be almost independent of the diffraction parameter G, convenient approximations for saturation curves for a periodic field

$$NP_+/G = \min(10N^2, 2.15\,\lg(7N+1)), \tag{3.32}$$

and a pulsed field

$$NP_+/G = \min(10N^2, 0.4\,\lg(N-0.28)+1.64). \tag{3.33}$$

can be used. Approximations are shown in Fig. 3.9 by thick light-blue lines. In both fields, the quadratic increase of the peak positive pressure is observed in a weakly nonlinear case and then gives place to a slow logarithmic increase. Precisely this increase describes saturation.

An analogous approximation was also selected for estimating limiting values of the peak negative pressure. Since these values are close in periodic and pulsed fields identical approximations were selected for both fields. Opposite to the saturation curves for the peak positive pressure, the values of the peak negative pressure at the given N depend on the parameter G

$$N|P_-|/G = \frac{\lg\left[\left(G/13+1.2\right)N+1\right]}{G/33+0.61}. \tag{3.34}$$

Figures 3.10 (a,b) show waveforms at different transverse distances ρ from the beam axis at the distance $\sigma = 0.8$ from the transducer. One can see that even at a small distance from the beam axis ($\rho = 0.24$) the waveforms are almost undistorted though on the axis the shock front is already formed in both periodic and pulsed fields.

Larger values of the peak positive pressure in periodic fields [Fig. 3.10(a)] can be explained qualitatively in the following way. Because of the Gaussian spatial apodization of pressure amplitude at the source, the peak pressure in the center wave is higher than in the wave coming from the source periphery. Since nonlinear effects manifest stronger for waves with larger amplitudes, the waves coming from the source periphery are distorted much weaker than shock central waves [Figs. 3.10(a,b)]. In nonlinear periodic fields, waves from the center of the source and its periphery are focused almost to the geometrical focus of the source (Fig. 3.11). Increasing of the pressure amplitude on the source leads to saturation effect for a center wave but not for waves coming from the source periphery: they are always linear. This is the reason that the saturation curve for a periodic field in the range of the studied parameters does not stabilize at a constant level and the value of the peak pressure in the focus continues to grow slowly [Fig. 3.9(a)].

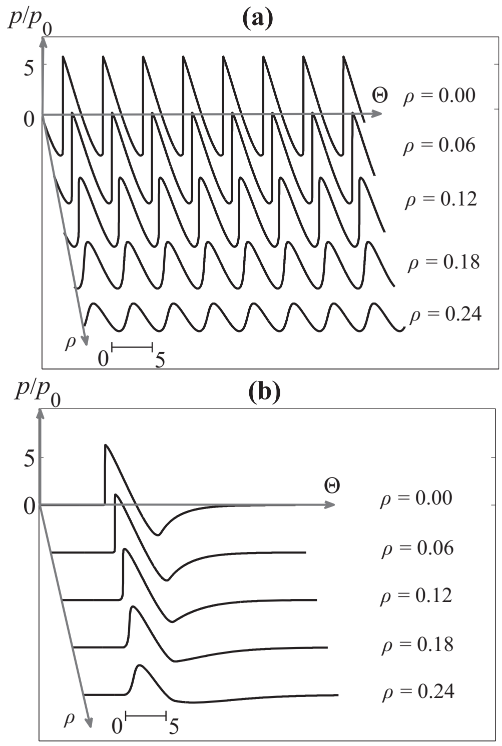

Figure 3.10: Waveforms at different transverse distances ρ to the beam axis at $\sigma = 0.8$ in the cases of periodic (a) and pulsed (b) fields generated by a Gaussian source.

In contrast to periodic fields, the phenomenon of nonlinear refraction is very significant in pulsed fields. Waves from the central part of the source are focused behind the geometrical focus due to nonlinear refraction, while weaker waves from the beam periphery still come approximately to the geometrical focus of the source (Fig. 3.11). Thus, in distinction to a periodic field, in a pulsed field the waves from the central part of the source and from the source periphery are focused at different points and, therefore, they do not amplify each other. This leads to the fact that, in pulsed fields, a saturation curve stabilizes at a constant pressure level lower in comparison with pressure in periodic beams with the same pressure amplitude at the source. Thus limitation of the peak positive pressure in pulsed fields is caused by the phenomenon of nonlinear refraction.

Figure 3.12 presents the dependencies of the beam energy on the distance σ from the source in periodic (a) and pulsed (b) focused fields at different values of the nonlinear parameter $N = 0.2$, 0.5, 1.0, and 3.0. The energy of a pulsed field at

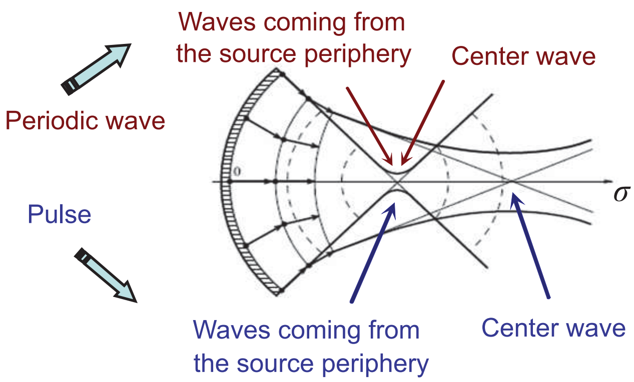

Figure 3.11: Focusing waves coming from the central part of the Gaussian source and from its periphery.

an arbitrary distance from the source was calculated as an integral over a time window and over the beam aperture in squared pressure at each point. Then the energy was normalized to its initial value. The energy over a single period was calculated as the energy of a periodic wave and also normalized to its initial value

$$\frac{E}{E_0} = \iint \frac{p^2}{p_0^2} a da dt. \tag{3.35}$$

One can see from Fig. 3.12 that near the source the energy of periodic and pulsed beams remains constant. Then, starting from the distance σ corresponding to the length of shock formation in waveforms at the beam axis, the energy starts to decrease due to nonlinear absorption in shocks. It is well known that in a plane nonlinear wave the energy of a pulsed signal after shock formation decreases with the distance as $1/\sigma$ and the energy of a periodic field decreases faster as $1/\sigma^2$ (Rudenko & Soluyan, 1977). In this case the effect of pressure saturation is observed in a plane periodic wave, while there is no saturation for a pulsed signal (Rudenko, 1995,Rudenko & Sapozhnikov, 2004). In the case of a focusing, the energy of a periodic field decreases with the distance also faster than the energy of a pulsed nonlinear field (Fig. 3.12). Thus nonlinear absorption is pronounced stronger in focused periodic nonlinear fields than in pulsed ones. This allows one to conclude that the main mechanism leading to saturation in focused periodic fields is nonlinear absorption. The effect of nonlinear refraction in significant only in a very small region near the focus and is insignificant on the whole. For pulsed fields the main mechanism of saturation of the peak positive pressure is nonlinear refraction.

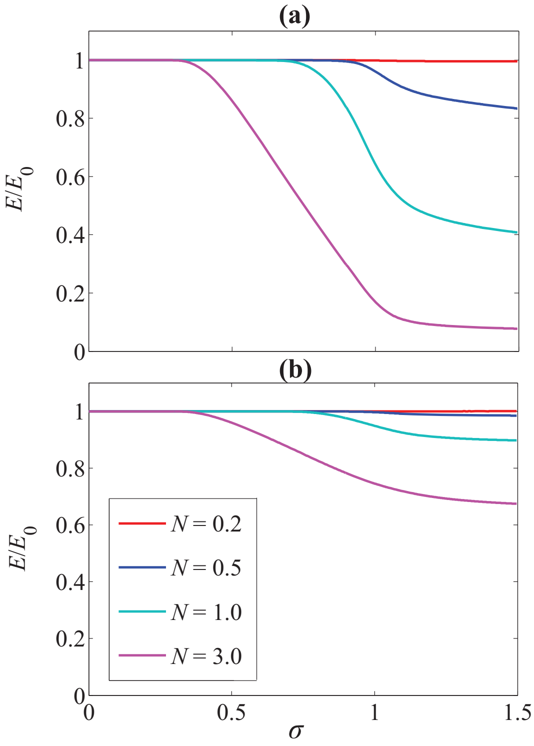

Figure 3.12: Dependencies of the beam energy on propagation distance σ for the periodic waves (a) and pulses (b) calculated with different values of nonlinearity $N = 0.2, 0.5$, 1.0, and 3.0.

Note that despite the fact that the energy of a periodic beam decreases faster, the maximum attainable value of the peak positive pressure in a periodic field is higher than that in a pulsed one. These peculiarities of nonlinear propagation provide a possibility to use beams of pulses for more effective delivery of the wave energy to the focal region, and periodic waves - to achieve higher values of the pressure amplitude in the focus.

§3.4 Effect of source apodization on spatial structure and limiting values of shock wave parameters in nonlinear focused beams

In a previous section it was shown that spatial structure and limiting values of acoustic parameters of focused fields depend on the signal temporal structure. Results of numerical simulations demonstrate that parameters of acoustic field are also strongly dependant on the distribution of the pressure amplitude on the source (or so-called source apodization). In a current section, Gaussian and uniform (piston) apodizations of the source are considered since they are the most widespread and corresponded to real transducers used in medicine (Hill *et al.*, 2002, Bailey *et al.*, 2003, Averkiou & Cleveland, 1999).

Figures 3.13 and 3.14 demonstrate two-dimensional spatial distributions of the peak positive (Fig. 3.13) and peak negative (Fig. 3.14) pressures in the case of focused periodic (a, c) and pulsed (b, d) fields produced by sources with Gaussian (a, b) and uniform (c, d) apodizations. Sizes of focal areas are shown in white solid lines and were determined by level of e^{-1} from peak pressure maximuma in each field. Differences in all four cases are clearly observed: for Gaussian source focal areas of peak pressures are 2–3 times narrower along the propagation direction σ than in the case of piston source. This is due to the fact that in fields produced by Gaussian sources, the shock formation occurs only in the central part of the beam where pressures are higher than in periphery. Waves from source periphery are coming in geometrical focus in Gaussian fields. Focusing of

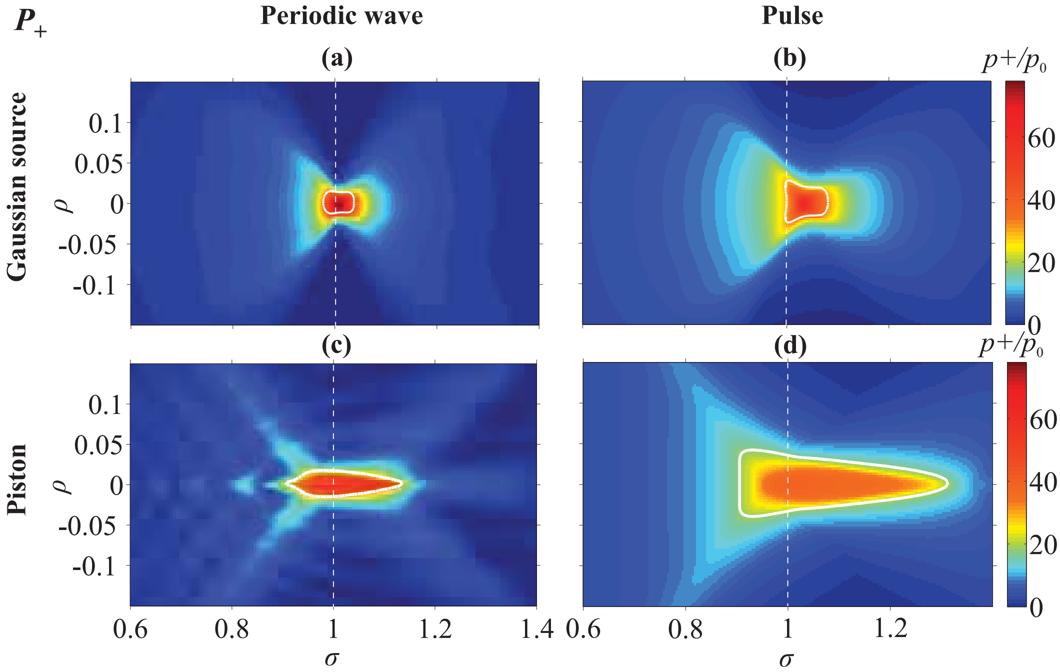

Figure 3.13: 2D spatial distributions of the peak positive pressure in cases of a Gaussian source (upper series a, b) and piston source (lower series c, d). Distributions in left column (a, c) correspond to the periodic field while the right column (b, d) - to the pulsed field. White solid lines indicate sizes of focal areas. White dashed lines show the plane of the geometrical focus. Distributions are plotted for $G = 40$, $N = 1.0$.

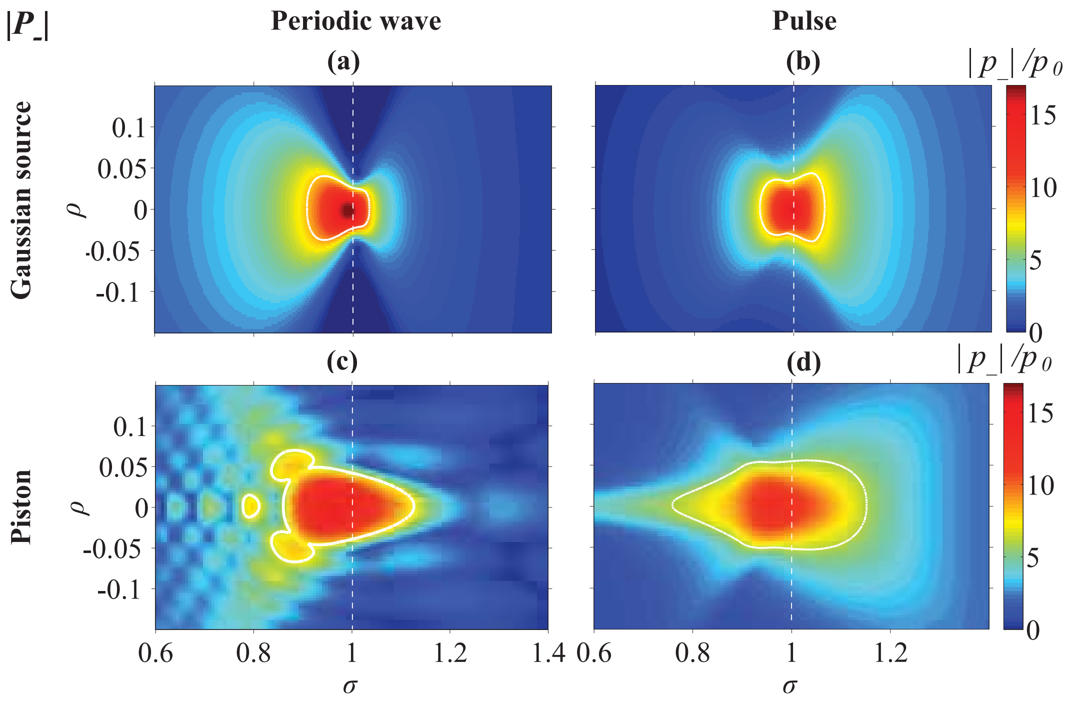

Figure 3.14: 2D spatial distributions of the peak negative pressure in cases of a Gaussian source (upper series a, b) and piston source (lower series c, d). Distributions in left column (a, c) correspond to the periodic field while the right column (b, d) - to the pulsed field. White solid lines indicate sizes of focal areas. White dashed lines show the plane of the geometrical focus. Distributions are plotted for $G = 40$, $N = 1.0$.

the edge wave of the piston source occurs nonlinearly that enhances the effect of the nonlinear refraction and increases sizes of the focal area.

Note that the transition of the source apodization from Gaussian to the uniform one changes the structure of both periodic and pulsed fields. In periodic field, oscillating structure caused by interference of the central and the edge waves appears [Figs. 3.13, 3.14 (c)]. In pulsed fields, there are no spatial oscillations but nonlinear effects become significant not only for the central wave but also for the edge wave.

Consider on-axis structure of nonlinear pulsed field produced by a focused piston source. In Figs. 3.15, 3.16 distributions of peak positive and peak negative pressures are shown for different values of the nonlinear parameter N. In the case of moderate focusing (Fig. 3.15, $G = 10$), the increasing of the pressure amplitude on the source shifts the on-axis maximum of P_+ away from the source while the shock formation is not occurred. After formation of the shock front, focus of P_+ shifts in opposite direction, i.e., towards to the source. The trajectory of the focus is a loop (Fig. 3.15). Focus displacement of P_+ away from the transducer is caused by the effect of nonlinear refraction. After shock is formed, nonlinear absorption becomes significant and focus moves back to transducer. In the case of Gaussian source, focal area of P_+ of pulsed field moves away from the source in the whole range of N. Difference in trajectories indicates that nonlinear refraction defocusing the beam is prevailing in Gaussian fields. For a piston source the structure of the focal area is determined equally by both nonlinear refraction and nonlinear absorption. This is due to the fact that nonlinear effects in Gaussian fields are significant only in paraxial part of

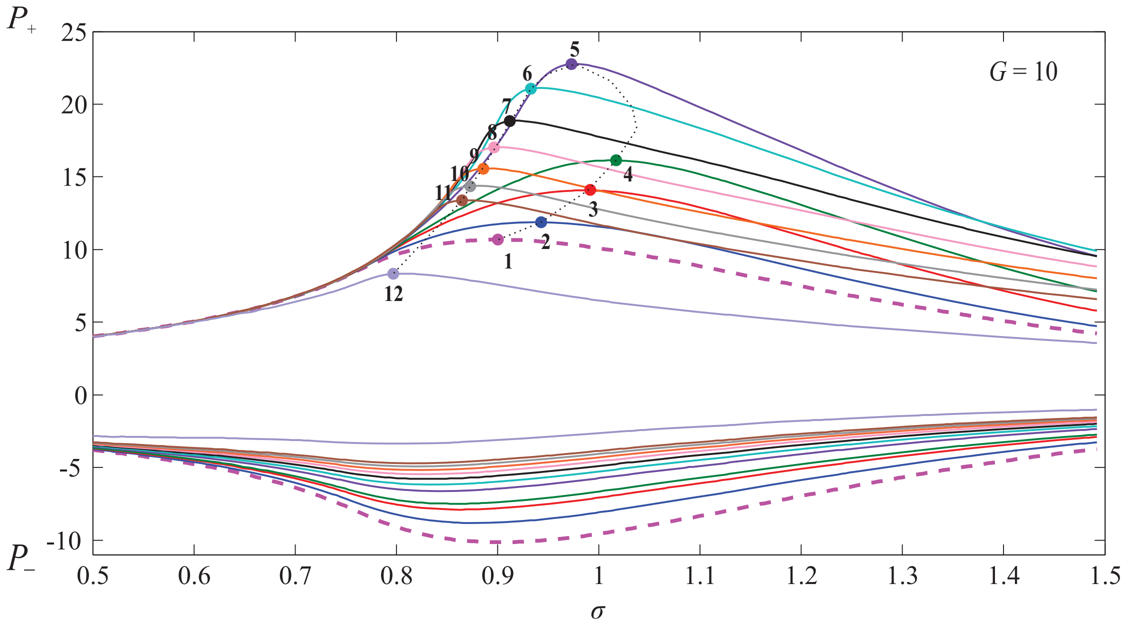

Figure 3.15: Distributions of peak positive P_+ and peak negative P_- pressures on the axis of the piston source in pulsed field at $G = 10$. Values of nonlinear parameter N are shown on the legend to Fig.3.16.

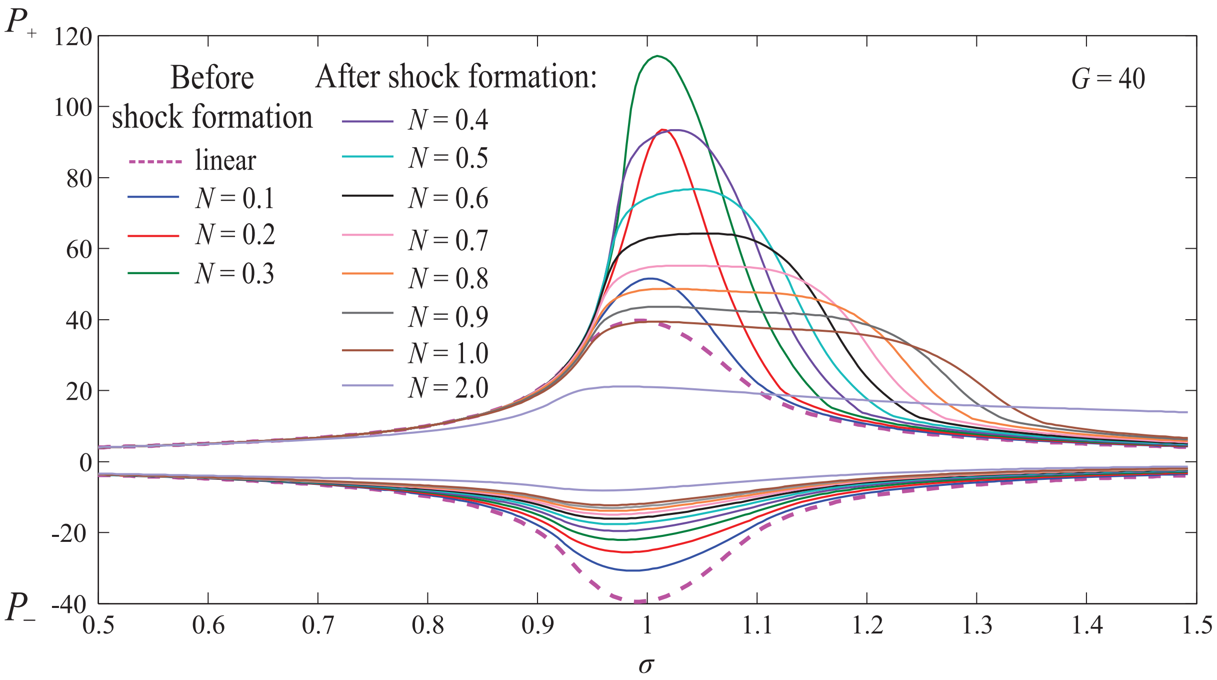

Figure 3.16: Distributions of peak positive P_+ and peak negative P_- pressures on the axis of the piston source in pulsed field at $G = 40$.

the beam with high pressure levels; while for a piston source nonlinear effects play significant role over the whole surface of the transducer.

Interesting features are observed for strong focusing of pulsed field when the influence of nonlinear refraction becomes more significant. In fig. 3.16, on-axis distributions of peak pressures are shown for a piston source at $G = 40$. Before the shock formation, shift of the focus of P_+ is negligible and a displacement from the geometric focus ($\sigma = 1$) is about 3% of the focal length. However, after shock is formed in a pulse profile, the focal region broadens and reaches in the

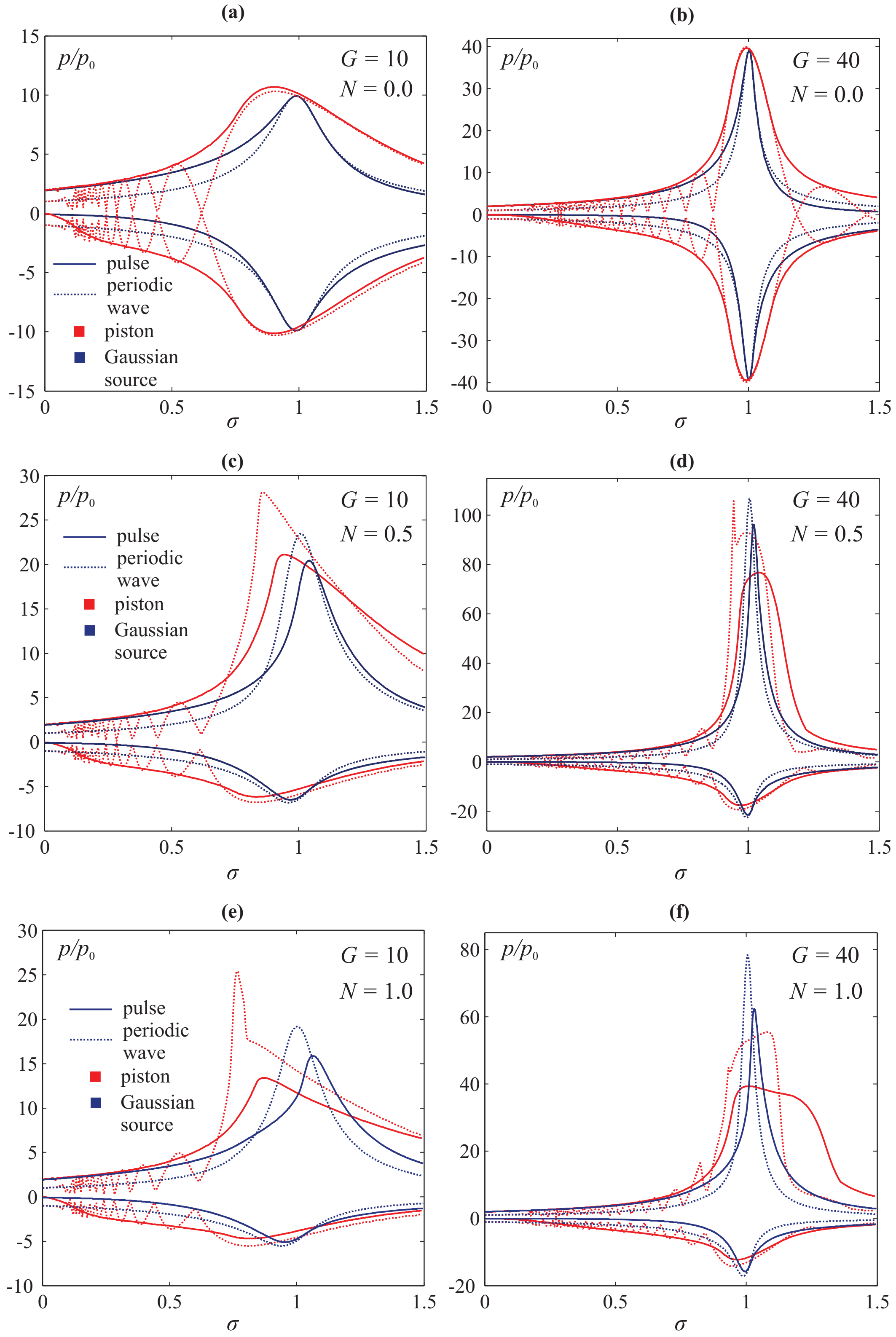

Figure 3.17: Distributions of peak positive P_+ and peak negative P_- pressure on the beam axis in cases of focused Gaussian source (blue curves) and piston source (red curves). Distributions are given for pulsed (solid lines) and periodic (dashed lines) fields at $G = 10$ (a, c, e) and $G = 40$ (b, d, f).

longitudinal direction 30% of the focal length. The peak positive pressure remains constant along the whole focal region: starting from $N = 0.6$ distributions in the region of the maximum of P_+ contain a plateau (Fig. 3.16).

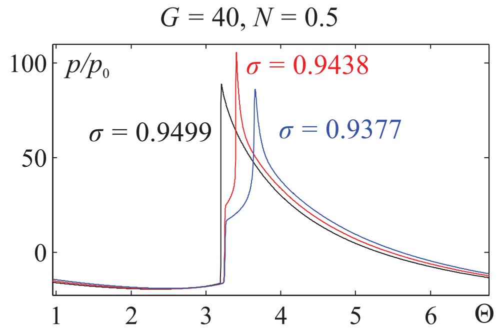

Figure 3.18: A single period of periodic wave in the area of the peak ($G = 40$, $N = 0.5$).

If nonlinear effects are strongly pronounced (curve for $N = 2.0$ in Fig. 3.16) a maximum of P_+ is reached before the geometrical focus since nonlinear absorption of energy on the shock front is significant. Then there is a very gradual decline in the peak positive pressure due to the appearance of nonlinear refraction. Thus, nonlinear effects significantly change the distribution of peak positive pressure compared to the linear case. Changes in the distribution of the peak negative pressure P_- with an increase of the pressure amplitude on the source (parameter N) is also quite strong, but it is more predictable: the focal area of P_- is slowly shifted to the source, $|P_-|$ is monotonically decreased. (Figs. 3.15, 3.16).

To analyze the focusing efficiency of periodic and pulsed fields produced by Gaussian and piston sources, let one compare acoustic fields with the same focusing angle (parameter G) and the same pressure amplitude p_0 on the source (parameter N). Note that such comparison describes not fully equivalent cases since the piston source at the same pressure amplitude p_0 will be powered more than a Gaussian source. However, the choice of the same pressure amplitude p_0 on both sources is caused to the same waveforms and peak pressures at the focus in the linear case for all four acoustic fields. In this way periodic and pulsed fields generated by a Gaussian source were compared in the previous section.

In Fig. 3.17, axial distributions of peak pressures P_+ and P_- are presented for all four cases mentioned above. Dashed lines correspond to curves for periodic field, solid lines correspond to pulsed field. Curves for a Gaussian source are shown by dark-blue color and curves for a piston source are shown by red color. Distributions are given for two values of diffraction parameter ($G = 10$ and $G = 40$) in cases of linear propagation $N = 0.0$ (a, b); nonlinear propagation at $N = 0.5$ (c, d) when shock is just formed for Gaussian fields; and in a case of strong nonlinearity at $N = 1.0$ (e, f) when shocks are developed for all fields. It is clearly seen that regardless the source apodization and manifestation of nonlinear effects, in periodic fields levels of P_+ and $|P_-|$ are higher than in pulsed fields [Fig. 3.17(c–f)]. Thus, focusing of periodic fields is preferred for achieving highest peak pressures. The second important feature is wider focal area in fields produced by a piston source compared to size of focal area in Gaussian fields. This feature is observed already in a linear case.

If the goal of focusing is to focus the acoustic beam in the focal region of the small size, one should use a focused periodic field of a Gaussian source. Periodic fields produced by a piston source contain sharp and narrow peaks in the distribution of P_+ in the region before focus: an example of such structure is clearly visible in Fig. 3.17(d). The reason for the formation of these peaks is a merger of two shocks in one period of a periodic wave to one shock front and, as a consequence, a sharp increase in the nonlinear absorption and rapid attenuation of the peak amplitude (see Fig. 3.18).

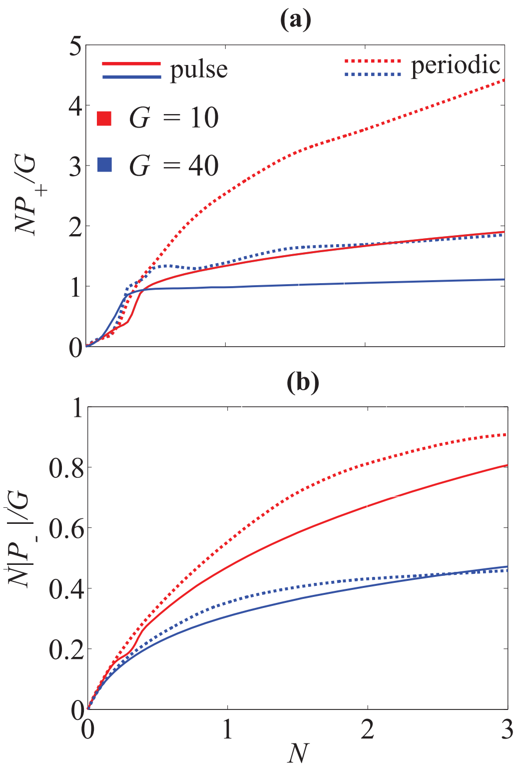

Figure 3.19: Saturation curves of peak positive (a) and peak negative (b) pressures in pulsed (solid lines) and periodic (dashed lines) fields of piston source. Curves are plotted for highest values of P_+ and $|P_-|$ achieved in each field.

In strongly nonlinear focused fields [Fig. 3.17 (d,f)] produced by a Gaussian source, peak pressures for periodic and pulsed fields are higher than in the case of piston source. The reason is more stronger manifestation of nonlinear effects for a piston source: nonlinear effects are significant along the whole transverse coordinate which leads to stronger nonlinear absorption of energy and to lower values of peak positive pressure at the focus than in Gaussian fields. Thus, transducers with Gaussian apodization are better suited to achieve highest peak pressures in a small focal area than piston sources.

Saturation curves of peak positive and negative pressures in the case of piston source are shown in Fig. 3.19. In contrast to ones obtained in Gaussian fields [Fig. 3.9(a)], saturation curves for a piston source are no more superimposed for different values of the diffraction parameter G. This means that limiting values of peak pressures for a piston source depend on either pulse duration or the frequency of the harmonic wave. For a case of $G = 40$ the peak positive pressure in pulsed field reaches the saturation immediately after the formation of the shock front.

Saturation curves for peak negative pressure for periodic and pulsed fields differ no more than 35% [Fig. 3.19(b)]. Levels of $|P_-|$ in fields produced by a piston source are below corresponding levels of $|P_-|$ in Gaussian fields [Fig. 3.9(b)].

§3.5 Interaction of shock fronts in nonlinear focused acoustic beams

As shown in the previous section, during the propagation of acoustic wave shock fronts of the same wave can interact with each other (Fig. 3.18). To observe this phenomenon for periodic waves, the shock formation should occur in the penultimate pressure maximum on the transducer axis, then in the region of the main maximum central wave interferes with an edge wave. The edge wave is reverse polarity wave, in which shock is formed in another part of the profile. As a result, the formation of two shocks in the single period of the wave occurs and their interaction is observed (Khokhlova *et al.*, 2001). In the numerical simulations performed in this study, similar phenomenon was also observed in nonlinear focusing of pulsed fields produced by a piston source and oscillating near field was found absent. Such interaction of fronts in space, not in time, will

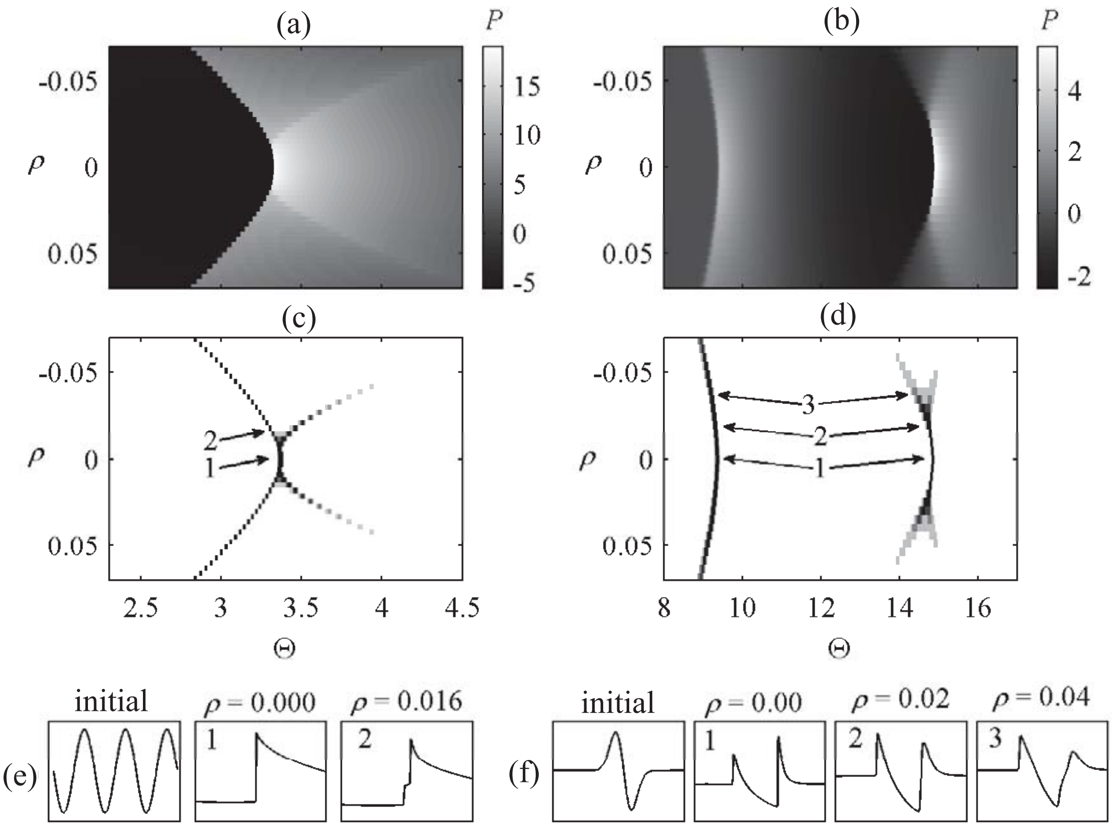

Figure 3.20: Mach stem formation in the focused beams of periodic waves [(a)-(c)] and bipolar pulses [(d)-(f)]. (a), (d) Temporal pressure waveforms at different transverse distances ρ from the beam axis. (b), (e) Temporal derivatives of the pressure waveforms shown on (a) and (d) correspondingly, i.e., numerical schlieren images. The darker greys indicate higher values of the derivatives. (c), (f) Initial waveform and waveforms at different radial distances ρ from the axis indicated by arrows in (b) and (e) correspondingly.

be similar to the Mach stem formation described in detail in the previous chapter. This paragraph will be devoted to this phenomenon.

It is interesting that attempts to ’find’ in numerical simulations the spatial structure similar to the Mach stem were not successful in fields produced by Gaussian source regardless the temporal structure of the signal. The Mach stem formation does not occur in fields of Gaussian source. This is caused by the absence of the interaction of two shocks, for Mach stem formation the edge wave should contain the shock front. In the case of Gaussian source the edge wave is always linear. Also it was impossible to ’find’ the Mach stem formation in the focal area of piston source generated pulses without pronounced rarefaction phase (for example, for pulse shown in Fig. 3.5(a)). Therefore, nonlinear focused fields of harmonic wave and bipolar pulse produced by piston source were chosen for the study.

First, consider results of modeling obtained at $G = 10$ and $N = 1$ for nonlinear propagation of focused periodic acoustic waves [Figs. 3.20(a)-(c)]. It is clearly seen that the spatial structure of the wave front is very similar to the von Neumann reflection: it contains one front intersecting the beam axis (the Mach stem) further dividing into two fronts at each distance from the axis [Figs. 3.20(a) and (b)]. A continuous slope can be seen between the focusing front and the Mach stem that distinguishes the von Neumann reflection regime. Note that the Mach stem structure corresponds to one shock in one period of the wave [Fig. 3.20(c), waveform 1], while there are two shocks in one period of the wave away from the axis at $\rho = 0.016$ [Fig. 3.20(c), waveform 2]. In (Khokhlova *et al.*, 2001) it was shown that for the two shock structure in one period of the harmonic wave, the higher shock is coming from the edge of the source, and the lower shock is coming from its central part. The formation of the Mach stem structure in the focal area of acoustic beams is thus the result of nonlinear interaction of shock fronts of the edge and central waves. These two fronts merge, because the velocity of the shock depends on its pressure, the higher shock in the waveform propagates faster than the lower shock. These two shocks collide and the Mach stem forms in the beam region close to the axis.

In pulsed beams, the edge wave starts to collide with the central wave at the end of the pulse, therefore the second shock front and Mach stem structure form within an initially negative phase of the bipolar pulse [$14 < \Theta < 16$ in Figs. 3.20(d) and (e)]. The front pattern in this case also resembles the von Neumann reflection with continuous slope between the fronts of the central wave and the Mach stem [Fig. 3.20(d)], but the front structure is blurred [Fig. 3.20(e)]. Smearing of the front structure occurs since the edge wave in the pulsed fields is smoother than in the periodic fields [Fig. 3.20(f), rear shocks of waveform 2 and waveform 3] and thus the values of the pressure derivative are less. When the edge wave front merges with that of the central wave, they turn into a sharp shock and provide the excess of the pressure amplitude on the rear shock [Fig. 3.20(f), waveform 1]. This excess of the pressure is clearly observed as the white area in [Fig. 3.20(d)] at the location of the Mach stem structure.

Thus, numerical simulations based on the KZK equation for nonlinear periodic and pulsed acoustic beams in water showed a process analogous to the Mach stem formation. The structure of the front patterns in the focal region of the beam resembled to the von Neumann reflection as the result of interaction between the edge and the central waves coming from the source. For pulsed beams the effect occurred only for the rear shock of the pulse. In periodic fields generated by a piston source the Mach stem formation occurs at less values of nonlinear parameter N (i.e., at less pressure amplitudes on the source) than in the case of pulsed field.

§3.6 Conclusions

The chapter describes the effects of nonlinear saturation in focused beams of periodic waves and pulses generated by Gaussian and piston sources. Numerical simulations were based on the axial symmetric KZK equation. It is shown that in periodic fields the saturation of the peak positive pressure is mainly due to the effect of nonlinear absorption at the shock front. In acoustic fields of single pulses the main mechanism of saturation is the nonlinear refraction. The level of the peak positive pressure in the periodic field, achieved at the focus, appeared to be higher than that of the single pulse. The total energy of the beam of the periodic wave, however, decreases much faster with the distance from the source than that of the single pulse. These nonlinear propagation effects propose a possibility to use pulsed beams for more effective delivery of the wave energy to the focal region while periodic waves are preferable to use for achieving higher peak pressures at the focus. Also it was shown that the formation of the Mach stem could be observed in the focal area of piston source in fields of periodic waves and bipolar pulses; and could be described using the KZK equation.

Chapter 4

Characterization of nonlinear focused ultrasound fields of new medical devices

§4.1 Introduction

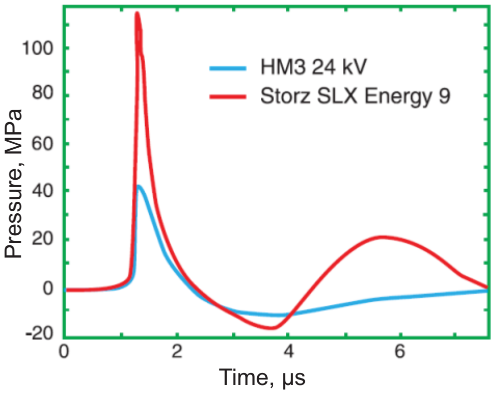

Figure 4.1: Profiles of shock pulses measured at the focus of lithotripters Dornier HM3 and Storz SLX. The figure is taken from (Cleveland & McAteer, 2012).

Focusing of shock pulses is an important problem of nonlinear acoustics since focused shock waves are widely used in medical applications. Lithotripters are among the first medical devices which uses shock pulses in clinical practice. For about 30 years lithotripters are used for destruction of kidney stones (Hill *et al.*, 2002, Bailey *et al.*, 2003). There are three types of lithotripters: electrohydraulic, electromagnetic, and piezoelectric (Cleveland & McAteer, 2012). Classification is based on the method of the pulse excitation. The shock front in the initial profile of the generated pulse is contained only in fields of electrohydraulic lithotripter; the principle of its action is based on creating an electrical discharge in one of the foci of the elliptical reflector. Pulses generated by electromagnetic and piezoelectric sources initially do not contain shocks. In these cases, formation of the shock front occurs while pulse propagates and is caused by nonlinear effects pronounced due to high pressure levels.

Examples of waveforms measured at the foci of electrohydraulic (Dornier HM3) and electromagnetic (Storz SLX) lithotripters are shown in Fig. 4.1. Typical parameters of pulses used in lithotripsy are following: peak positive pressure is in the range from 30 to 110 MPa, peak negative pressure is from -20 up to -5 MPa, and a duration of pulses is several microseconds (Cleveland & McAteer, 2012).

Extracorporeal shock wave therapy (ESWT) is another important medical application of shock pulses. Since the beginning of the 90s ESWT is used for noninvasive treatment of multiple musculoskeletal disorders such as tendonopathies, plantar fasciitis, lateral epicondylitis, pain after joint replacement, bedsores, etc (Kudo *et al.*, 2006, Rompe *et al.*, 2003, Gerdesmeyer *et al.*, 2003, Furia, 2005, Rompe, 2004, Steinberg, July 2006). Therapeutic effects induced by ESWT include a growth of blood vessels in a sore (angiogenesis effect) (Ito *et al.*, 2009); osteogenesis effect (new bone formation) (Endres *et al.*, 2008); and antinociceptive effect (Wang, 2003, Ohtori *et al.*, 2001) (Fig. 4.2). After ESWT procedure, a patient feels less pain, a possibility of movement in joints appears, local metabolism becomes improved, and blood circulation is restored in tissue.

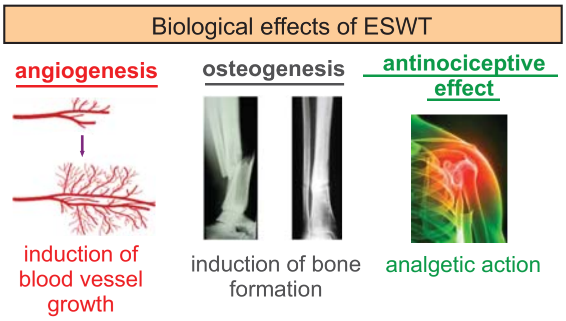

Figure 4.2: Biological effects of ESWT; X-ray of healing of fractures is taken from (Endres *et al.*, 2008).

Although ESWT is used clinically and refers to the use of focused shock waves, physical mechanisms of ESWT action on bones and tissues are not fully understood (Cleveland *et al.*, 2007). It is believed that one of the ESWT actions based on the cavitation effect on the boundary of two media. Acoustic impedances of water and soft tissue are almost the same and significantly less than acoustic impedance of bone. As a result, propagating pulses almost do not damage soft tissues but have a direct effect on the bone. When fractures grow together slowly or false joints are formed, powerful pulses destroy the surface layer of the bone. Micro-cracks and a large number of tiny fragments of bone are formed. Stimulation of bone formation (osteogenesis) occurs and a blood supply in the fracture zone is improved (Steinberg, July 2006). A lot of clinical studies have shown high efficiency and effectiveness of the ESWT (Endres *et al.*, 2008, Wang, 2003, Kudo *et al.*, 2006, Rompe *et al.*, 2003, Gerdesmeyer *et al.*, 2003, Furia, 2005, Rompe, 2004, Steinberg, July 2006, Ohtori *et al.*, 2001). However, there are a number of works (Brown *et al.*, 2005, Buchbinder *et al.*, 2002, Haake *et al.*, 2002) which state that the positive effects of ESWT is a placebo effect while there are no therapeutic effects. The reason of this disagreement is not full understanding of the physical and biological mechanisms of ESWT action on biological tissues and lack of optimal treatment protocols for each of the diseases and for each available device (Cleveland *et al.*, 2007). If a treatment protocol is not sufficient the therapy has no effects.

ESWT devices use the same methods of shock waves generating as lithotripters use. However, there are also pneumatic (or ballistic) ESWT devices which are considered to be the most inexpensive and reliable (Cleveland *et al.*, 2007). ESWT uses longer pulses than lithotripsy does: their duration is about 20 μs in contrast to 5 μs in lithotripsy; peak positive pressures vary from 4 MPa up to 40 MPa depending on the particular device model; peak negative pressures are in the range from -20 MPa up to -4 MPa.

Pneumatic and electromagnetic ESWT devices are the most common in clinical practice. Acoustic fields generated by pneumatic ESWT device were studied by Cleveland (Cleveland *et al.*, 2007) for the model EMS Swiss Dolorclast Vet (Fig. 4.3a) used in veterinary practice. The emitter of this model is equipped with radial (unfocused) and focusing applicators. However, measurements of the field indicated that focused applicator on clinically significant distances (up to 12 cm from the source) has qualitatively the same field structure as unfocused applicator has. This was explained by too large focusing distance of the focused applicator. Pressure waveforms measured in water at a distance of 1 cm from transducer are shown in Fig. 4.3 (b, c) for both applicators. Waveforms are

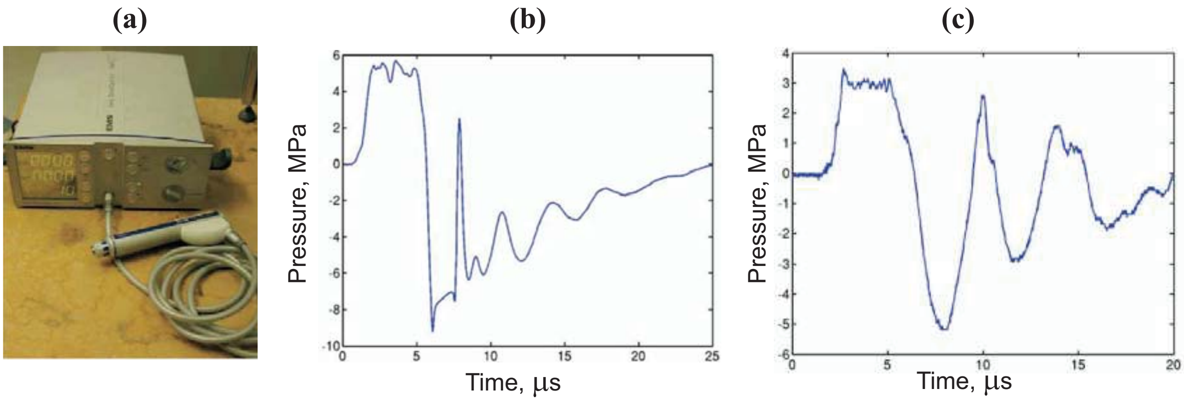

Figure 4.3: (a) Pneumatic ESWT device, model EMS Swiss Dolorclast Vet. (b), (c) Pressure waveform measured in water at a distance 1 cm from the source for unfocused and focused applicators, correspondingly. Figures are taken from (Cleveland *et al.*, 2007).

strongly different from ones used in lithotripsy (Fig. 4.1): they don't contain typical for lithotripsy pressure jump with a shock front at the beginning of the pulse.

In this chapter of the thesis the acoustic field of a clinical ESWT device (Duolith SD1 T-Top produced by Storz Medical, Switzerland) is characterized in water using a combined measurement and modeling approach.

Device Duolith SD1 is used in orthopedics, cosmetology, and neurology. The Duolith SD1 T-Top device has dual modes of operation, one called "focused shock wave therapy" (focused electromagnetic head), and the other one is "radial shock wave therapy" (ballistic head). Radial mode is used for the treatment of diseases with shallow location or required low energy surface treatment. Focused therapy is used for the treatment which requires deeper penetration. Fig. 4.4 demonstrates how the treatment of a heel spur and tennis elbow occurs using the focused therapy head (figures and acoustic parameters of generated pulses are taken from technical specification sheet of Duolith SD1).

Focused fields of electromagnetic ESWT devices are more intensive compared to ones of pneumatic devices, therefore, nonlinear effects in case of electromagnetic sources are more substantial.

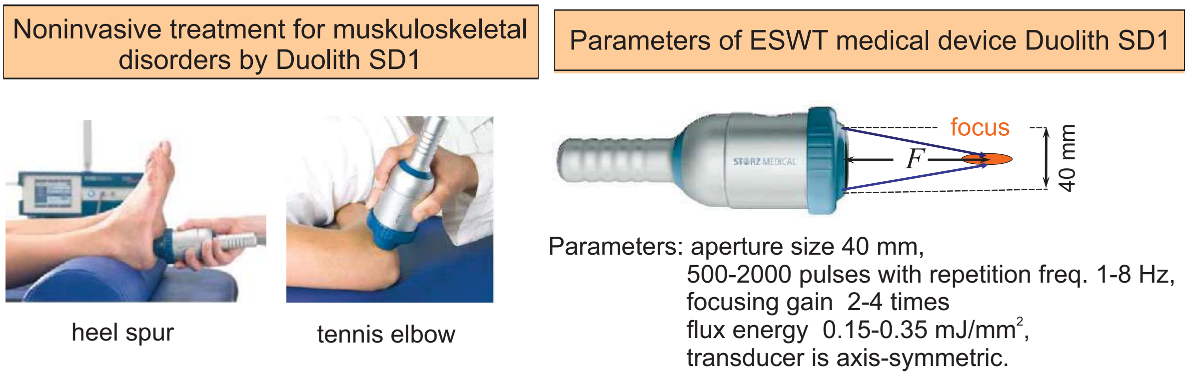

Figure 4.4: Noninvasive treatment for orthopedic disorders using ESWT device Duolith SD1 (Storz Medical, Switzerland). Figures and acoustic parameters of generated pulses are taken from technical specification sheet of Duolith SD.

At the moment, the presence of shock front in pulses produced by electromagnetic ESWT devices remains unknown; this problem is studied in section §4.2 using methods of numerical simulations.

Figure 4.5: Use of acoustic radiation force to push kidney stones. Diagnostic probe Philips C5-2 controlled by Verasonics is used for the procedure.

Another new promising medical application of focused shock pulses is a treatment of kidney stones by pushing small stones from the kidney using an acoustic radiation force (Fig. 4.5) (Shah *et al.*, 2010). Formation of kidney stones (nephrolithiasis) is a common urological disease, which affects about 10% of the population during their lifetime. Nephrolithiasis may be asymptomatic and detected only at the time of examination of the body in cases of suspected other diseases. However, in the 85% cases kidney stones are beginning to move from the kidneys through the ureters into the bladder causing a blockage of the ureter and severe pain attacks (renal colic). Patients describe renal colic to be extremely painful. Every year thousands of operations to remove kidney stones are held. Mentioned above lithotripsy is the medical procedure that is widely used for extracorporeal removal of kidney stones. It utilizes high-energy focused shock pulses to break stone into small fragments which can pass from the body in a natural way. However, remaining of residual stone fragments in the lower pole of the kidney is a common problem confronted by urologists and documented in 21%-59% of patients who underwent lithotripsy (Osman *et al.*, 2005).

Ultrasonic propulsion of kidney stones is a new stone management technique being under development. It uses a diagnostic ultrasound probe to create a real-time B-mode image and to generate a pulse to move the kidney stone out of the kidney with acoustic radiation force (Fig. 4.5). Ultrasonic propulsion could be an alternative extracorporeal procedure to remove small kidney stones by pushing them toward ureter; or effective method to facilitate passage of stone fragments after lithotripsy.

Preliminary investigative clinical results of ultrasonic propulsion have been successful and the displacements of kidney stones pushed by acoustic radiation force were fixed in experiments in the porcine model (Shah *et al.*, 2012). Recently, the method has been successfully tested on patients volunteers who were waiting for a lithotripsy procedure (Hickey, January 10, 2014). In preliminary experiments, the pushing of kidney stones were produced by a standard diagnostic probes (Philips ATL HDI C5-2 and ATL HDI P4-1) generated long millisecond pulses at the highest possible applied voltage. Physical principles and treatment protocols are still not developed for this new technology.

This chapter of the thesis is devoted to investigation of nonlinear effects in the fields of modern diagnostic (Philips C5-2 probe) and ESWT (Duolith SD1) medical devices. The combined measurement and modeling approach (Kreider *et al.*, 2013, Canney *et al.*, 2008, Bessonova &

Wilkens, 2013) was used to describe the field structures. The approach is based on using low power measurements to set boundary condition in numerical model (Perez *et al.*, 2013, Karzova *et al.*, 2013, Karzova *et al.*, 2015a). Experiments were performed in the Center for Industrial and Medical Ultrasound (CIMU), University of Washington, Seattle. The author was participated in planning of experiments, data processing and discussion of obtained data.

§4.2 Nonlinear effects in acoustic field of a clinical shock wave therapy device Duolith SD1

4.2.1 Measurements of pressure waveforms by a fiber optic probe hydrophone in water

Experiments were performed in CIMU by its former PhD student Camilo Perez (Perez C., 2015).

Measurements were performed on the portable Duolith SD1 T-Top (Storz Medical AG, Tägerwilen, Switzerland) ESWT device that uses a focused electromagnetic source. The electromagnetic source was coupled with the standoff of 20 mm radius that contains the oil bag attachment to the membrane of the therapy head. The therapy head was located outside the water tank (31 cm long×18 cm deep ×18 cm wide) and was coupled to the tank via a tegaderm window and coupling gel (Fig. 4.6). The maximum degassed level 8% O_2 was at room temperature. Measurements of the acoustic field were performed in water using a 3D computer-controlled positioning system (Velmex NF90, Bloomfield, NY) and a fiber optic hydrophone (FOPH 2000, RPI, Acoustics, Germany; the fiber tip was 100 μs in diameter). The focal length of therapy head was set $F = 30$ mm; the machine pulse repetition frequency was ranged from 1 to 8 Hz.

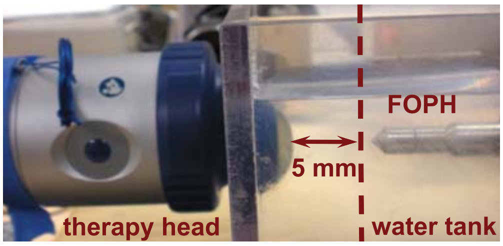

Figure 4.6: Measurements of pressure waveforms at the plane located 5 mm far from the source.

Alignment of the FOPH to the acoustic field was done by performing a raster scan in two separate planes: One plane intersected the acoustic axis at the focus, with the maximum pressure at the center. The other plane was distal to the first. The beam axis was found as a line crossing the pressure maxima of the two planes. The FOPH was positioned parallel to the axis x of the beam. Radial symmetry of the field emitted from the device was confirmed after initial experiments.

4.2.2 Setting a boundary condition in a model using a method of an equivalent source

To set a boundary condition in numerical model the method of equivalent source was applied (Kreider *et al.*, 2013, Canney *et al.*, 2008, Bessonova & Wilkens, 2013, Perez *et al.*, 2013, Karzova *et al.*, 2013, Karzova *et al.*, 2015a). The method consists in using of experimental data to set parameters

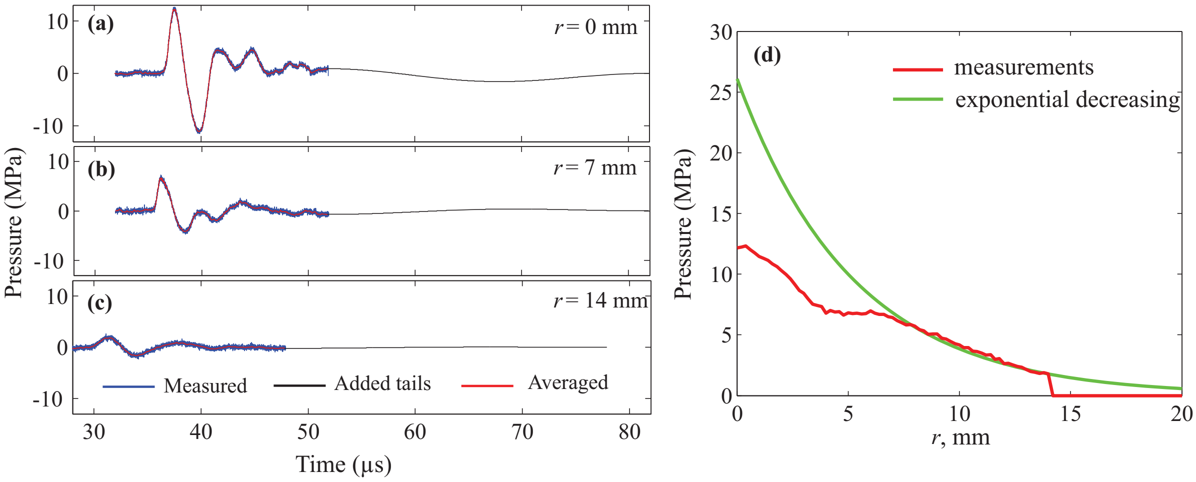

Figure 4.7: (a),(b),(c) Radial scan waveforms in a plane 5 mm from the standoff at radial distances $r = 0$, 7 and 14 mm, respectively. Typical measured waveforms are shown in blue, the waveforms after averaging in red, and the numerical tails added to each waveform are shown in black. (d) The red curve shows the decreasing pressure amplitude with radial distance. Additional waveforms were introduced from 14 mm to 20 mm with the amplitude shown in green color.

of so-called ’equivalent source’, which generates the same acoustic field as the real transducer. In experiments, pressure waveforms were measured radially in a plane as close to the therapy head as possible for the existing experimental arrangement, which was approximately 5 mm from the standoff (Fig. 4.6). The waveforms were measured from the beam axis at $r = 0$ up to the radial coordinate $r = 14$ mm. Although the standoff radius was 20 mm, measurements at distances $14 < r < 20$ mm were not collected because of low signal-to-noise levels. A total of 71 waveforms were measured with a spatial step 0.2 mm, time step 2 ns and duration 20 μs. Signals were sampled at 500 MSample/s and each waveform was averaged over 20 individual waveforms. These data were used to set a boundary condition for numerical modeling of the ESWT field.

Representative examples of averaged waveforms collected from the experiment for setting the boundary condition are shown in Fig. 4.7 (a,b,c) in blue. In order to make them applicable for the numerical simulations it was necessary 1) to reduce the noise level in the measured signal; 2) to add the tail to each waveform for zero mean value of the signal (which is necessary for fast Fourier transform (FFT) in numerical simulations); 3) to change the spatial step of the grid for boundary condition; 4) to add waveforms in the radial scan from 14 mm to 20 mm from the axis. Each procedure is described below in more detail.

Reducing the noise level in measured waveforms

To facilitate the modeling effort, each experimental waveform was numerically smoothed to reduce the noise level in the measured signal. To avoid decreasing the signal amplitude in the smoothing process each waveform was divided into two parts. The first part contained the region around the maximum of the peak positive pressure (within 1.25 μs) and the second part contained the other smoother parts of the pulse. The first part was numerically smoothed 3 times over 5 points that allowed for keeping the same amplitude level. The second part of the signal was smoothed 3 times over 30 points. The resulting smoothed waveforms are also shown in Fig. 4.7 (a,b,c) in red.

Requirement of zero mean value of the waveform

The general properties of the solution to the KZK equation yield that the time integral over the pulse must be equal to zero, as the zero frequency component in the FFT series expansion of the signal is eliminated by diffraction. To ensure that the pulses used for the boundary condition satisfy this requirement, a tail of $\Delta t = 30$ μs duration was added at the end of each pulse as

$$p(t_*) = p_1 \cos^2(\pi t_*/2\Delta t) - (p_1 + \frac{2S}{\Delta t}) \sin^2(\pi t_*/2\Delta t)\,. \tag{4.1}$$

Here p_1 is the pressure value at the last measured time point of each waveform, t_* is time counted from this last point, S is the integral over the averaged waveform. The absolute value of the maximum pressure in the tail did not exceed 1.6 MPa, i.e., it was of the same order as the level of noise in the measured waveforms (± 0.7 MPa). The tails adding to waveforms are shown in Fig. 4.7 (a,b,c) as black lines.

Changing steps of the grid

The radial step in the numerical modeling was further refined by adding 36 waveforms in between each two experimental waveforms. Each of these 36 additional waveforms was obtained by linear interpolating the pressure for each time point in the neighboring experimental waveforms. The coefficients for interpolation were i/36 and $(1 - i/36)$ where i is the number of an additional waveform between the two experimental ones. As a result, the radial step was refined to 5.4 μ m instead of 0.2 mm in the experiment.

With the numerically added tail, the number of time points increased to 25000, with a time step of 2 ns. A requirement for FFT version used in our simulation program5 is setting the number of time points as a power of 2. In order to satisfy this requirement the number of time points was increased up to 32768 by padding the signals with zeros.

Adding waveforms at the edges of the source

To account for non-measured waveforms in the radial coordinate from 14 mm to 20 mm from the axis, additional waveforms were numerically introduced in the boundary condition by taking the very last radial waveform obtained at 14 mm and exponentially decreasing its amplitude along the radial coordinate with a linear time delay that followed the overall geometry of the measured field. The decrease in the pressure amplitude along the radial coordinate is shown on Fig. 4.7(d) as a red line, additional waveforms were introduced with the amplitude shown in Fig. 4.7(d) by a green line.

Obtained using the method of equivalent source boundary condition is shown in Fig. 4.8 and was used in the modeling of KZK equation. Here, the time-axis of the signals is shifted by 32

μs, so that its beginning corresponds to $t = 0$. In the simulations, boundary condition was set in the window of 65.5 μs × 43.2 mm. Not shown in Fig. 4.8 part of boundary condition was equal to zero. One can clearly see that the profiles have a different time delay depending on the radial coordinate r, which will provide the focusing of the beam in the simulations.

4.2.3 Numerical modeling based on the KZK equation

The KZK equation (3.26) with the boundary condition described above (Fig. 4.8) was simulated using an algorithm previously described in detail in section §3.2. The parameters for the modeling were: 16384 harmonics, 32768 time-steps, 65.5 μs time window, 2 ns time step, 43.2 mm radial window, 8000 radial grid points, 5.4 μm radial step, and 0.11 mm axial step.

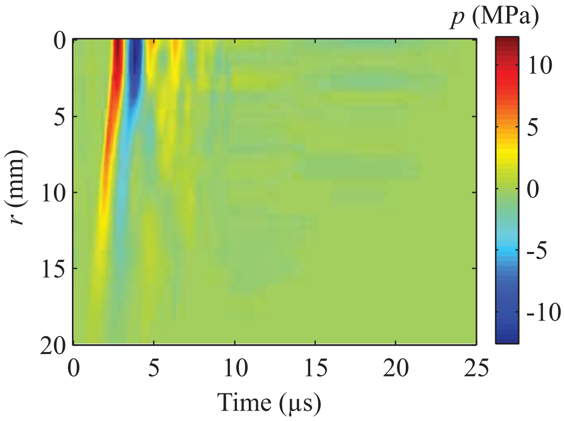

Figure 4.8: Boundary condition map for the modeling algorithm.

4.2.4 Comparison of data obtained in measurements and nonlinear modeling

Numerical simulations of ESWT device Duolith SD1 were performed in wide range of supplied power. First, consider structure of the acoustic field corresponding to the boundary conditions obtained from the experiment - this situation corresponds to supplied power used in clinical practice. To confirm the validity of the numerical simulations, a series of measurements of pressure profiles was further conducted along the beam axis and in the transverse direction in focal plane at $F = 30$ mm.

A comparison of the measurement and modeling results for peak positive and negative pressures along the axis is shown in Fig. 4.9. Experimental results are shown by black circles and numerical results by red lines. The position of the therapy head is marked by blue dashed line. Modeling results are in a good agreement with the experimental data for the peak positive pressure and there are some discrepancies for the peak negative pressure, but they are all within the experimental error. It was observed that the maximum of the peak negative and positive pressures were achieved in different spatial locations: at $x = 29$ mm away from the therapy head for p_+ and at $x = 12$ mm for p_-. This difference is caused by a com-

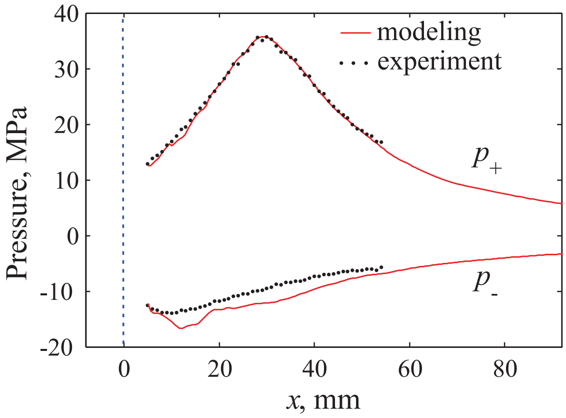

Figure 4.9: Axial distribution of the measured peak positive and peak negative pressures (black circles) compared to the modeling results (red line). Blue dash line corresponds to the position of the therapy head of the standoff.

bination of nonlinear and diffraction effects. The measured and modeled waveforms at different distances x from the source along the beam axis are shown in Fig. 4.10. Red color corresponds to simulated waveforms and grey color corresponds to experimental ones. There is excellent agreement between the measured and modeled axial waveforms, where again, the simulations predict a slightly more negative peak pressure. Note that simulated waveforms are well fitted with experimental ones in a sharp pressure jump at the front of the pulse formed due to nonlinear propagation effects in the focused beam.

The radial (transverse) scans for peak positive p_+ and peak negative $|p_-|$ pressures in the focal plane $F = 30$ mm are shown in Fig. 4.11 in two perpendicular to the beam axis directions.The modeling results are in excellent agreement with the measurements and confirm radial symmetry of the acoustic field generated by Duolith SD1.

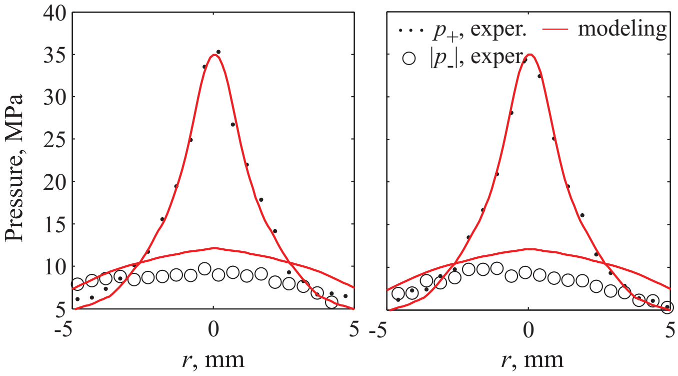

Figure 4.11: Radial (transverse) scans at the focus for peak positive p_+ and peak negative $|p_-|$ pressures in two perpendicular to the beam axis directions.

Numerical modeling has a great advantage over experiment that provides full reconstruction of the spatial structure of the field that is difficult to implement in the experiment. Spatial distributions of the peak positive pressure p_+, peak negative pressure p_-, and intensity I are of particular interest since p_+ is associated with the stress, p_+ is associated with cavitation, and I is responsible for heating. The 2D spatial distribution of these values obtained in numerical simulations are shown in Fig. 4.12. One can see how different focal area of all three distributions: for p_+ it has an

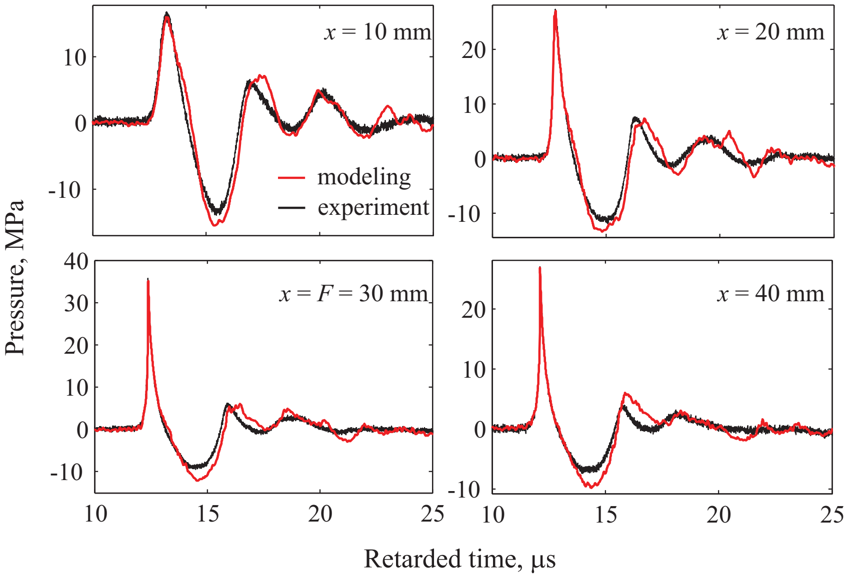

Figure 4.10: Axial pressure waveforms at different x distances from the transducer. Black color corresponds to measured profiles and red color to modeled ones.

elongated shape along the axis of the beam and is localized at about a focal depth $F = 30$ mm; focal areas of $|p_-|$ and I are wider in the transverse direction than the focal area of p_+ and located at a distance corresponding to about one third of the focal length F.

Numerical simulation were performed for a wide range of initial pressure amplitudes on the source. This was done by scaling the pressure amplitudes of the boundary condition (Fig. 4.8) from 0.4 to 2 in steps of 0.1. From these scaled pressures, the axial distributions and focusing gain can be compared for increasing source output. Although this linear scaling does not precisely correspond to changing the output level of the device, it was an adequate approach as nonlinear effects were weak at the distance where measurements for the boundary condition were taken.

The results of these additional simulations are shown in Fig. 4.13a. The dashed lines correspond to the results simulating the experimental conditions. One can see how the focal zone changes with source pressure amplitude. With an increase in source output, the position of the spatial maximum of p_+ on the beam axis changes non-monotonically. It first moves away from the source and then backward. This effect is typical for nonlinear focused beams and has been observed in the earlier studies described in chapter 3 (§3.4) for focused pulsed fields. The shift away from the source is characteristic for focusing without formation of shocks. It is caused by strengthening of the nonlinear self-refraction phenomenon because the speed of the pulse front depends on its amplitude. At very high source outputs, when a shock is formed prefocally, strong absorption at the shock results in diminishing of the peak positive pressure and the maximum moves backward. Note also that the maximum shift in the natural focus from the lowest to highest setting is about 6 mm. The peak negative pressure maximum always moves toward the source with the increase of its output.

Therapeutic bioeffects from ESWT are often categorized as being due to the presence of the shock front. Despite the fact that the name of therapy requires a shock front, in work (Cleveland *et al.*, 2007) it was shown that the field of ballistic transducer EMS Swiss Dolorclast Vet, used in veterinary medicine, does not contain not only shock fronts, but even sharp jumps in pressure. In the case of electromagnetic transducer Duolith SD1 nonlinear effects are pronounced stronger than in fields of ballistic transducers and the waveform of the pulse at the focus (Fig. 4.10) is similar to one produced by lithotripters.

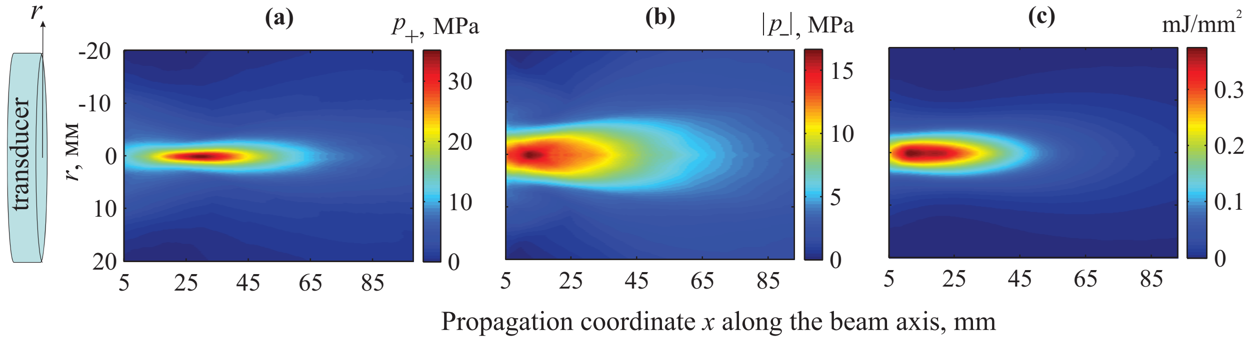

Figure 4.12: Two-dimensional spatial distributions of the peak positive (a) and peak negative (b) pressures, and energy density (c) in the field generated with the short standoff obtained in the modeling of transducer Duolith SD1.

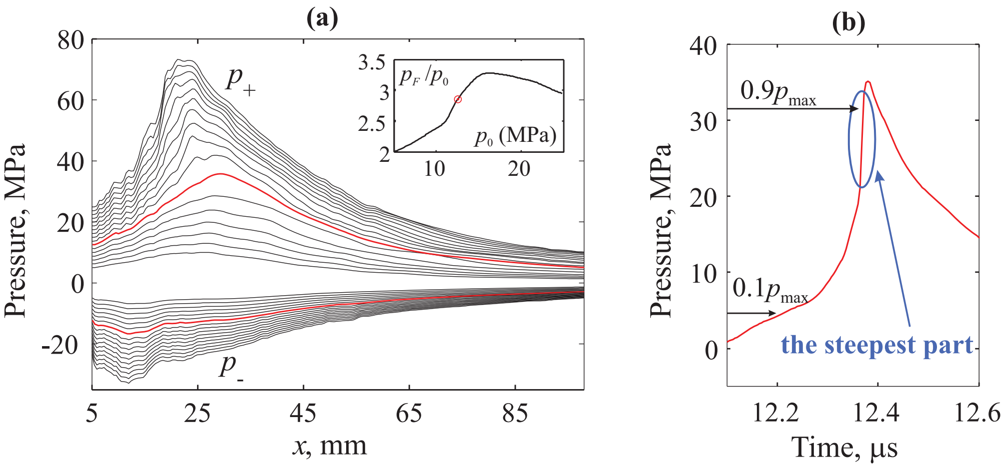

Figure 4.13: (à) Simulations of the axial peak pressure distributions. Inset: The focusing gain for the peak positive pressure (inset). The dashed lines correspond to the results simulating the experimental conditions. The inset shows the ratio of the peak positive pressure at the focus to its initial value at the boundary as a function of the source pressure output. The dashed circle in the inset indicates the experimental point corresponding to that gain curve. (b) Front at the focus of the transducer.

The shock front determines the minimum spatial scale at which the biological effects of ultrasound occur in the tissue. If the size of the cell is larger than the width of the shock front then the shock front can break the cell membrane due to the formation of strong spatial gradient field. If the shock front is wider than the cell size then it will cause only the acceleration in the cell movement. The average size of a human cell is about 10-30 microns which corresponds to the time scale of the order of 1 ns in the pressure waveform. The limited temporal resolution of the hydrophone (2 ns) does not allow to register the fine structure of the front in measurements. However, to answer the question whether the shock wave therapy IS a SHOCK wave therapy can be obtained by using numerical simulations.

In Fig. 4.13 (b) a front at the focus obtained in numerical simulations is shown (distance $x = F = 30$ mm, the whole waveform is shown in Fig. 4.10). It is clearly seen that the smooth 'pedestal' rise precedes the sharp pressure jump. The classical definition of the shock front determines its duration τ_{rt} from 10% to 90% of the peak positive pressure (shock amplitude A_s) and the shock is supposed to be governed by the stationary solution of the Burgers equation (Hamilton & Blackstock, 1998)

$$p(\tau) = \frac{A_s}{2}\left\{1 + \tanh\left(\frac{\varepsilon A_s}{2b}\tau\right)\right\} = \frac{A_s}{2}\left\{1 + \tanh\left(\frac{\tau}{\tau_0}\right)\right\}, \tag{4.2}$$

where τ is the retarded time, ε and b are coefficients of nonlinearity and the thermoviscous absorption of the propagation medium, correspondingly, $\tau_0 = 2b/\varepsilon A_s$.

In Fig. 4.13 (b) the part of the front corresponded to pressure rise from 10% to 90% of its maximum value is shown. This part of the front contains a smooth 'pedestal' rise. Thus, classical definition of the shock rise time is not correct in this case. To account only the steepest part of the front the shock rise time should be defined using its derivative. The $0.1A_s$ to $0.9A_s$ rise time of the pressure at the shock in Eq. (4.2) is the length of time for the function $\tanh$ to change from -0.8 to

0.8, and is equal to $\tau_{rt} = 2.2\tau_0$. The time derivative of Eq. (4.2) is $\partial p/\partial\tau = A_s/2\tau_0 \cdot \cosh^{-2}(\tau/\tau_0)$ $= A_s/2\tau_0 \cdot (1 - \tanh^2(\tau/\tau_0))$. It is equal to 0.36 of the maximum value of the derivative when $\tanh$ is equal to plus or minus 0.8. For a stationary shock such as governed by Eq.(4.2) these two definitions are equivalent.

The shock rise time described by Eq.(4.2) is defined by combined effects of nonlinearity and thermoviscous absorption. Nonlinear effects tend to steepen the shock, while thermoviscous effects of energy absorption at the shock tend to smoothen it. The balance of these two effects creates a shock of quasi stationary thickness τ_{rt}, inversely proportional to the shock amplitude A_s. If the front of amplitude A_s has greater thickness than τ_{rt} then the front is not a shock and potentially can be more steeper due to nonlinear effects.

Now estimate the thickness of the front at the focus of Duolith SD1 and analyze whether the front is a shock. The rise time of the front calculated on the level of 0.36 of the maximum of the pressure derivative is 8 ns that corresponds to pressure $\Delta p = 25$ MPa at the front (Fig. 4.14). In the case of the shock front with an amplitude $A_s = \Delta p/0.8$ the thickness of the front defined from Eq.(4.2) is $\tau_{rt} = 0.28$ ns (for propagation in water at $\varepsilon = 3.5$, $b = 4.33 \cdot 10^{-3}$ kg/(c·m)). Thus, the shock formation did not occur for current clinical machine Duolith SD1 settings.

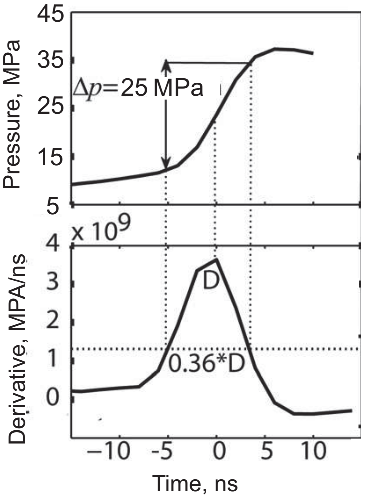

Figure 4.14: Definition of the shock rise time used its time derivative (level 0.36 of the maximum level of the derivative should be used).

Note that the estimation of the shock front thickness given above was obtained for propagation in water. However, if the shock front formation is not occurred in water it will not be formed in biological tissue since the absorption will be even more significant.

In focused nonlinear fields the shock front formation occurs then the focusing gain reached its maximum (Bessonova O.V. *et al.*, 2009, Rosnitskiy *et al.*, 2015). The inset of Fig. 4.13 (a) shows the peak positive focusing gain, given by the ratio of p_+ at the focus to its initial value at the boundary, as a function of the source pressure output. In our case, the experimental conditions correspond to the output level that is lower than the level of the maximum focusing gain, i.e., the shock has not yet formed. Apparently, if the device could generate an extra factor of 2 in pressure at the source, a shock may indeed form at the focus.

§4.3 Nonlinear effects in ultrasound field of rectangular focused diagnostic-type transducer Philips C5-2

4.3.1 Low power measurements on the axis and in the focal plane of the transducer

Measurements were performed in CIMU (Seattle) by Bryan Cunitz.

The illustration of the experimental setup for pressure field measurements of Philips C5-2 abdominal imaging probe (Philips, Bothel, WA) is depicted in Fig. 4.15. The focused pressure fields were generated using a V-1 Verasonics ultrasound engine with extended transmit burst capabilities (Verasonics, Kirkland, WA); the Verasonics was controlled through an HP Z820 PC (HP, Palo Alto, CA) using Windows 7 (Microsoft, Redmond, WA) and Matlab 2011b (Mathworks, Natick, MA). The probe was fixed vertically in a large water tank facing downwards. Water was degassed to about 10% dissolved oxygen. The axes of the probe were aligned to those of a 3-axis positioner (Velmex, Bloomfield, NY). A hydrophone was mounted to the positioner by a custom L-shaped fixture so that they were parallel to the imaging probe.

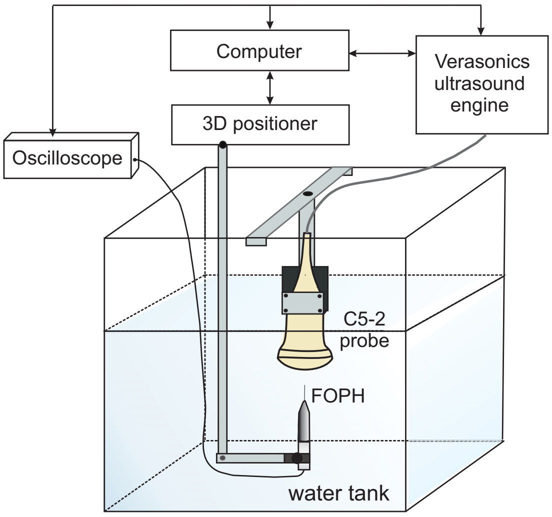

Figure 4.15: Diagram of the experimental arrangement for measurement of acoustic field in water. Fiber optic hydrophone (FOPH) was used for high-power measurements while low-amplitude measurements were performed using a capsule hydrophone.

High-power measurements were performed using a fiber optic hydrophone FOPH-2000 (RP-Acoustics, Leutenbach, Germany, the size of the tip is 100 μm) that allows measurements of pressure waveforms at frequencies up to 100 MHz. Fiber optic hydrophones have a relatively low sensitivity (approximately MPa) but they are well suited for measurements of high-amplitude pressure waveforms comprising steep parts.

Low-amplitude calibration measurements were performed using a capsule hydrophone HGL-0085 in conjunction with AH-2010 preamplifier (Onda, Sunnyvale, CA). Capsule hydrophones are used for measurements in the frequency range from 1 MHz to 20 MHz with pressure levels of the order of several MPa. The sensitive surface of the capsular hydrophone HGL-0085 is a PVDF membrane of 200 μm diameter.

The transmit signals were 75 cycles at $f = 2.3$ MHz with a pulse repetition frequency of 20 Hz. A trigger signal was generated by the Verasonics at the beginning of the transmit signal to synchronize oscilloscope acquisition.

The C5-2 array probe comprises 128 single elements located on a cylindrical surface (see Fig. 4.16). The projection of active probe surface onto the xy plane is a rectangle of the height l_y. Steering of the focus F_x in the xz plane is performing electronically by changing the pressure phase over the probe elements in x-direction. The cylindrical acoustic lens focuses the field at a constant depth F_y to reduce the divergence of the beam in the yz plane. Field measurements were performed for the regimes with 16, 32, 40, 64, and 128 active elements; the centermost elements for each configuration were used.

The exact geometrical parameters of the probe Philips C5-2 is unknown. Nominal parameters of the C5-2 probe were approximately measured by a ruler: radius of curvature $R \approx 38$ mm, angle of aperture $2\theta \approx 40^\circ$, and height $l_y \approx 12$ mm. Despite these values are not exact they give an initial approximation for fitting the parameters of an equivalent source in numerical modeling. The product specification sheet from manufacturer provide nominal values of the width of each element (0.37 mm) and the gap between them (0.05 mm). In experiments, delays to each of the elements of the probe were programmed by a time of flight calculation using the speed of sound in water as 1480 m/s and a focal position of $z = F_x = 50$ mm along the axis of the probe.

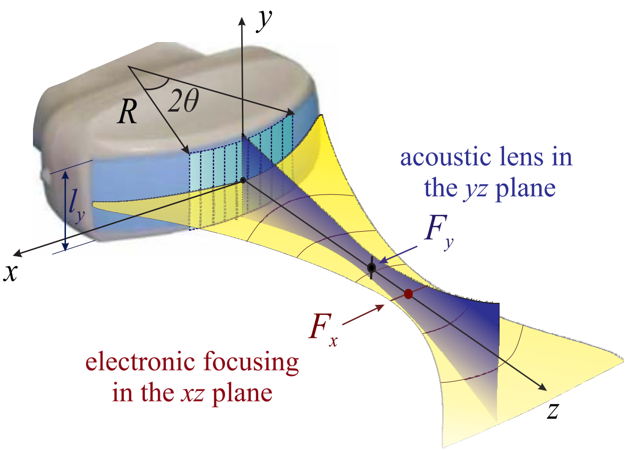

Figure 4.16: Geometry of focusing from the diagnostic 2.3 MHz C5-2 array probe

The hydrophone measurements included two steps. On the first one low-amplitude measurements of pressure waveforms were performed by capsule hydrophone along the beam axis z and in two perpendicular directions x and y in the focal plane at $z = 50$ mm. These measurements were carried out at the lowest possible voltage (2 V) applied to the probe and were used for setting a boundary condition to numerical model. A step size along the z-axis was 0.5 mm while transverse scans were done along x- and y-axis with the steps of 0.1 mm and 0.05 mm, correspondingly.

The second step of measurements were carried out for a wide range of applied voltages (from 5 V to 90 V). Pressure nonlinear fields were measured using a fiber optic hydrophone. The location of peak positive pressure was found using a transmit sequence with 128 elements at 50 V. At this location, corresponded to $z = 50$ mm, all the waveforms were collected at the different number of elements and different voltage levels. Each acquisition point used 128 averages with the FOPH bandwidth set at 100 MHz and a sampling rate of 320 MHz. The waveform was calibrated and deconvolved with a manufacturer supplied impulse response. Mean and standard deviation values for maximum positive pressure and minimum negative pressure were taken for 50 of the 74 cycles so that a steady state was reached in the waveform. These measurements were performed for further comparison with results of numerical modeling of nonlinear acoustic field of the probe.

4.3.2 Setting the boundary condition for numerical model using low-amplitude measurements of pressure waveforms

A boundary condition of numerical model was set by finding the best fit between distributions of pressure amplitude on the beam axis and in the focal plane obtained in linear modeling and in measurements. In numerical model, a continuous periodic wave of frequency $f = 2.3$ MHz was used as an initial condition. The pulse length in experiments was chosen sufficiently long (75 periods of harmonic wave) for such simplification in the modeling. The pressure amplitude was assumed to be uniform over the cylindrical surface of the equivalent source. The phase was

Table 4.1: Parameters of the equivalent source provided the best fit between results of linear field simulations using the Rayleigh integral with ones obtained in measurements.

Number of elements	**16**	**32**	**40**	**64**	**128**
Angle of aperture θ, rad $\times 10^{-2}$	8.421	16.842	21.053	33.684	67.368
Initial pressure amplitude p_0, kPa	295	275	265	217	160
Focal depth of acoustic lens F_y, mm	85	86	86	70	70
Other parameters	$F_x = 50$ mm, $R = 38$ mm, $l_y = 12.5$ mm				

changed continuously over the source surface to provide the focusing in planes xz and yz

$$p(R, \theta, y, t) = p_0 \sin\left[\omega t + k\left(\Delta x + \frac{y^2}{2F_y}\right)\right], \tag{4.3}$$

where $\Delta x = \sqrt{(R\sin\theta)^2 + (R - R\cos\theta + F_x)^2} - F_x$ is a path difference of focused waves emitted by the apex of the probe and by selected point on the surface of the probe; (R, θ, y) is a cylindrical coordinate system with the origin at the center of curvature of the probe; $\omega = 2\pi f$ is a cyclic frequency; $k = 2\pi f / c_0$ is the wavenumber, and t is time. Changing number of the operating elements was accounted in the model by changing the angle of aperture θ. Rayleigh integral was used for numerical calculation of linear acoustic field:

$$p(\vec{r}, t) = -i\rho_0 f \int\limits_S \frac{u(\vec{r}') \exp(ik\,|\vec{r} - \vec{r}'|)}{|\vec{r} - \vec{r}'|} dS', \tag{4.4}$$

where $\vec{r} = \{x, y, z\}$, ρ_0 is the density of water, and $u(\vec{r}')$ is the complex amplitude of the vibration velocity on the surface S of the probe.

Since parameters R, θ, l_y, p_0, F_x, and F_y of the probe were initially known only estimated, but not exactly, numerical calculation of the linear field was carried out in several iterations. The first time the field was calculated for approximate values of R, θ, l_y given above in subsection 4.3.1, and for $F_x = F_y = 50$ mm. Then, each of these five parameters was varied individually so that the pressure amplitude distributions normalized by its maximum coincided well with those measured at the first step of the experiment on the beam axis and in focal plane. Note that each of parameters affects on a particular feature in the distributions and therefore was quite easy defined. For example, parameter l_y has predominant influence on the pressure distribution in the focal plane along the y-axis, but has almost no effect on the axial distribution along the z-axis. After finding the best fit values of parameters R, θ, l_y, F_x, and F_y for configurations of 16, 32, 40, 64, and 128 active elements, the initial pressure amplitude p_0 was determined by multiplying the already found normalized distributions on required pressure at the focus. Obtained in this way geometric parameters of the equivalent source are shown in Table 4.1 for a different number of active elements.

Distributions of the pressure amplitude calculated numerically using the Rayleigh integral with the best fit parameters given in Table 4.1 are shown in Fig. 4.17 and are compared with measurements. The spatial structure of acoustic field of a C5-2 probe was strongly dependent on the number of active elements even in the case of a linear propagation. Fig. 4.17 demonstrates that with increasing of number of active elements the size of the focal area reduces in both longitudinal and transverse directions and the pressure amplitude at the focus increases.

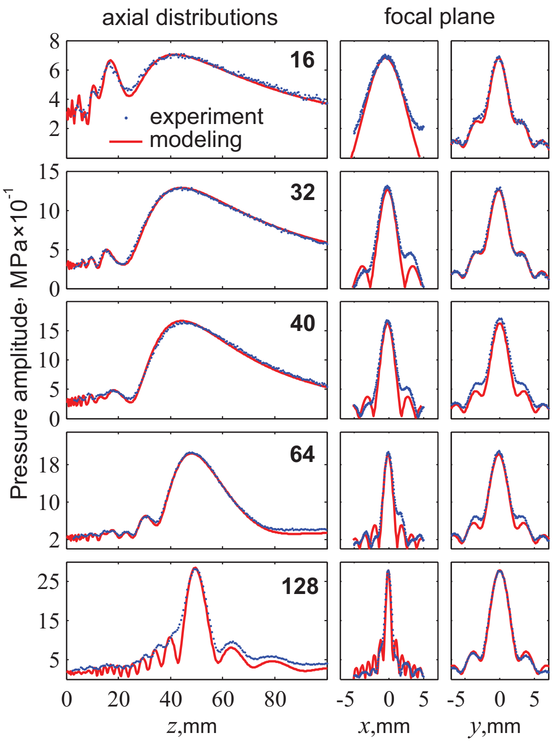

Figure 4.17: Comparison of simulated and measured acoustic pressure amplitude distributions at the lowest probe output of 2V (linear propagation). Axial pressure distributions are depicted in the left column while two right columns depict distributions in two transverse directions in the focal plane at $z = 50$ mm. Results are presented for 16, 32, 40, 64, and 128 active elements of the probe.

The numerical simulation of the linear field of the probe allowed to characterize the field structure in the entire space that is a time consuming task in measurements. Fig. 4.18 presents the two-dimensional distributions of the pressure amplitude in a plane located at a distance of 2 mm from the apex of the probe (upper series) as well as the beam focusing in the xz and yz planes (middle and lower rows, respectively). On distributions in the plane $z = 2$ mm the active surface of the probe is clearly visible and schematically shown by white dotted lines. Note that in the area in front of the edges of the active surface the pressure amplitude is up to two times higher than in the central part - particularly it is clearly noticeable for configuration of 128 elements. First, this is caused by the fact that waves coming from the edges of the probe are almost in phase. Second, they pass a longer path than waves coming from the central part of the probe and therefore increasing of the amplitude associated with the wave focusing is pronounced stronger. Distributions also clearly demonstrate that near field of the probe is a very nonuniform along its surface since waves emitted by the different elements interfere.

Now let one consider the structure of the field in the both focal planes of the beam (Fig. 4.18, middle and bottom rows). Case of 16 active elements is a single configuration for which the size of the active surface along the y-axis is greater than that along the x-axis. In this case the beam is weak focused and pressure amplitude at the focus is only 2 times higher than its initial value. The square shape of the active surface is achieved by powering the 32 elements of the probe. The structure of the field in the xz and yz planes is almost identical and the size of the focal area in both transverse directions is the same. One of the most common configuration used in clinical practice is 40 active elements. In this mode, the focusing is quite effective since the focal pressure amplitude is 6 times greater than its initial value. The transverse dimensions of the focal area defined by the level of -6 dB are 2×3 mm along x and y axes, respectively. With a further increase of the number of active elements, the focusing efficiency increases while the size of the focal areas decreases (64 and 128 elements configurations in Fig. 4.18).

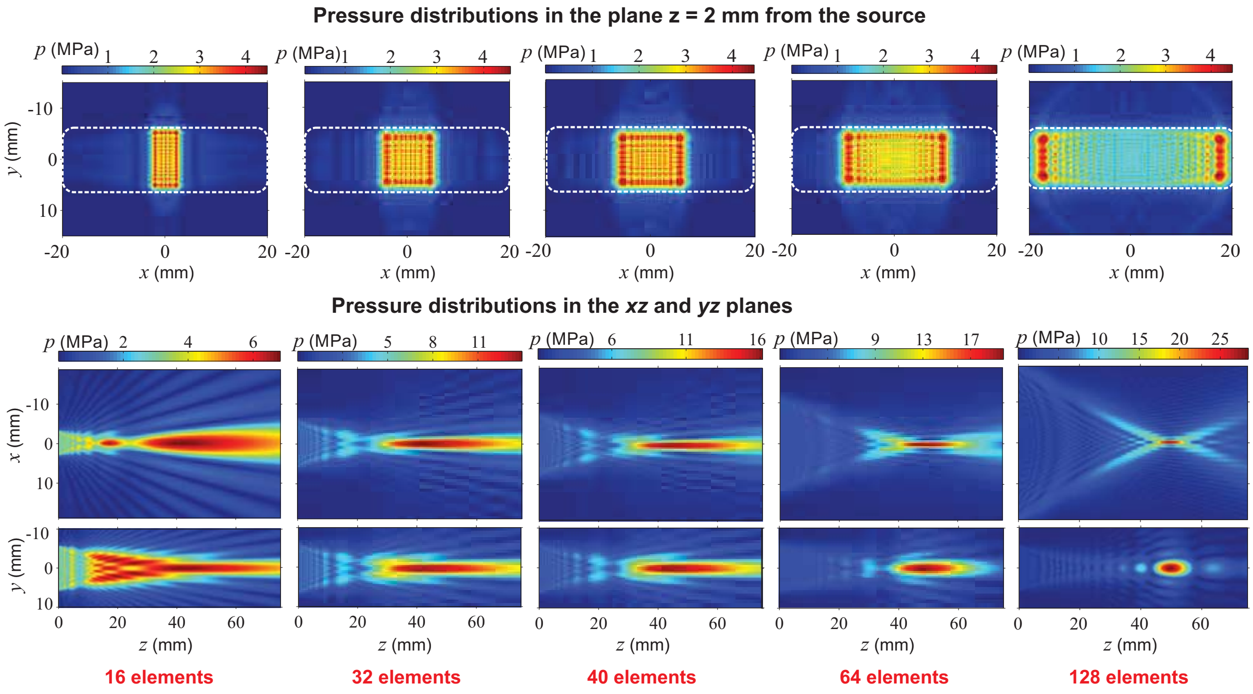

Figure 4.18: Spatial distributions of the pressure amplitude obtained in numerical simulations of linear propagation for 16, 32, 40, 64, and 128 active elements. White dashed curves show the active surface of the probe.

4.3.3 Transfer of the boundary condition from cylindrical surface to the plane

Once the parameters of the equivalent sorce were found on a cylindrical surface, the boundary condition for modeling three-dimensional nonlinear field of the C5-2 probe was set on the plane $z = 0$. For this aim pressure distribution in the plane $(x, y, z = 0$ mm) calculated using the Rayleigh integral was transferred onto the plane $(x, y, z = 0$ mm) using the angular spectrum method

$$p(z+\Delta z) = p(z)\exp[i\Delta z(\sqrt{k^2 - k_x^2 - k_y^2} - k)], \tag{4.5}$$

where k_x and k_y are spatial frequencies, Δz is the shift in z-axis z (Yuldashev P., 2011). The resulting distribution at plane $(x, y, z = 0$ mm) was used as a boundary condition to the 3D nonlinear ultrasound field modeling.

4.3.4 Numerical model based on Westervelt equation to calculate the three-dimensional nonlinear field

The Westervelt equation written in a retarded time coordinate was used to simulate nonlinear field generated by the probe (Westervelt, 1963)

$$\frac{\partial^2 p}{\partial\tau\partial z} = \frac{c_0}{2}\Delta p + \frac{\beta}{2\rho_0 c_0^3}\frac{\partial^2 p^2}{\partial\tau^2} + \frac{\delta}{2c_0^3}\frac{\partial^3 p}{\partial\tau^3}. \tag{4.6}$$

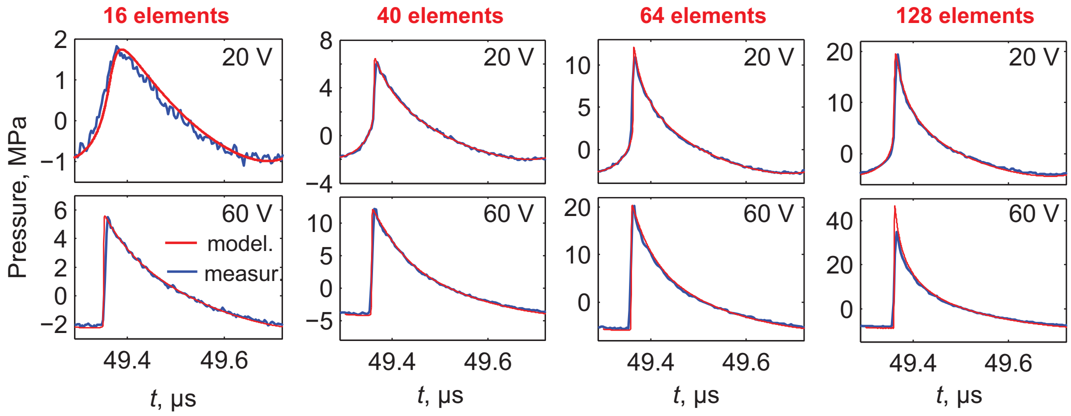

Figure 4.19: Comparison of single periods of wave at the focus of the probe obtained in numerical simulations and measured in water.

Here $\tau = t - z/c_0$, $\Delta p = \partial^2 p/\partial x^2 + \partial^2 p/\partial y^2 + \partial^2 p/\partial z^2$; parameters ρ_0, c_0, ε, and δ are the ambient sound speed, nonlinearity coefficient, and the thermoviscous absorption of the medium, respectively. The values of the physical constants were chosen to represent the experimental measurement conditions in water at room temperature $\rho_0 = 998$ kg/m^3, $c_0 = 1486\ m/s$, $\varepsilon = 3.5$, $\delta = 4.33 \cdot 10^{-6}$ m^2/s. Equation (4.6) describes nonlinear propagation in one-direction along the z-axis and in contrast to the KZK equation does not require the smallness of the diffraction angles.

Numerical algorithm for simulation the Westervelt equation (4.6) was developed in our laboratory earlier by Petr Yuldashev (Yuldashev P., 2011). The author of the thesis set the boundary and initial conditions to the solving code and found numerical grids. The details of the numerical algorithm is presented in (Yuldashev P., 2011), only its main stages will be listed here.

The simulations were performed using the method of fractional steps with an operator splitting procedure of second order. The diffraction operator was calculated in the frequency domain for each harmonic component using the angular spectrum method. The absorption was calculated in the frequency domain using an exact solution for each harmonic. The nonlinear operator was calculated in the frequency domain using a forth-order Runge-Kutta method at small distances from the probe and conservative time-domain Godunov-type scheme at greater distances. The switch to the Godunov-type scheme was made at a distance z where the amplitude of the tenth harmonic exceeded 1% of the amplitude at the fundamental frequency f. Parameters of the numerical scheme were: longitudinal step $dz = 0.075$ mm, transversal steps $dx = dy = 0.02$ mm. Maximum number of harmonics was set to 750.

4.3.5 Results on numerical simulations of nonlinear propagation, comparison with measurements

Numerical simulations of the three-dimensional nonlinear field of the diagnostic probe were performed in a wide range of applied voltages. In modeling, the increase of the applied voltage was simulated by increasing the pressure amplitude p_0 of the initial harmonic wave. The relationship between the pressure amplitude in the modeling and the applied voltage in experiment was found by assuming a linear dependence between these values. To validate the results of the modeling of nonlinear propagation, calculated pressure waveforms at the beam focus at $z = 50$ mm were compared with waveforms measured on the second stage of the experiment using a fiber optic hydrophone. Examples of measured waveforms and calculated ones are represented in Fig. 4.19 for configurations of 16, 32, 40, 64, and 128 active elements at the applied voltage of 20 V (upper row) and 60 V (bottom row).

Waveforms obtained numerically were in a good agreement (accuracy of 3%) with the experimental data for all configurations except the case of 128 active elements. In the last case a good agreement was observed only for voltages less than 25 V while for greater voltages modeling predicts higher values of the peak positive pressure than it was measured (see the last waveform in the bottom row of Fig. 4.19). Further, it will be shown that this discrepancy is possible due to the fact that the size of the focal area of the peak positive pressure p_+ at applied voltages (above 25 V) becomes smaller than the size of FOPH surface (100 μm). This kind of problem has been observed previously in the calibration of nonlinear fields produced by multielement arrays of therapeutic clinical noninvasive surgery system (Kreider *et al.*, 2013).

Diagnostic probe Philips C5-2 is designed for supplied voltages in the range from 2 V to 90 V. The lower boundary of this range corresponds to ultrasound visualization regime used in a clinical practice. From physical point of view it is a linear propagation of ultrasonic waves. Trial experiments to push kidney stones were performed using the upper limit of this range (90 V) when the wave profile is highly distorted due to nonlinear effects and contains a shock front. It is interesting to note that even at voltages equal to 20 V the steep parts in profile began to be formed and waveforms became to be strongly asymmetric (top row in Fig. 4.19). The formation of the shock front in waveforms occurred at the applied voltages equal to about one-third of the maximum.

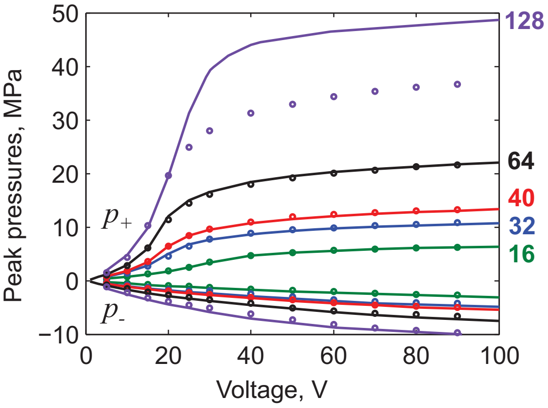

Figure 4.20: Saturation curves for the peak positive and negative pressures obtained in numerical simulation (solid curves) and in hydrophone measurements (markers) for configurations of 16, 32, 40, 64, and 128 active elements of the probe.

The efficacy of the treatment can be increased by using higher transducer output to provide stronger pushing force which requires greater focal pressure. However, nonlinear acoustic saturation effect can be a limiting factor. Fig. 4.20 shows the saturation curves for peak positive p_+ and peal negative p_- pressures for configurations of 16, 32, 40, 64, and 128 active array elements. Peak pressures were calculated at a distance $z = 50$ mm on the beam axis. Curves obtained in numerical simulations are shown by solid lines while measurements are shown by markers. One can see that starting from applied voltage of 50 V the peak positive pressure p_+ increases very slowly. If one assumes that the saturation of p_+ occurs when derivatives from saturation curves are less than 5% of its maximum value then the voltage level of 50 V will correspond to this threshold. Thus, pushing of kidney stones by acoustic radiation force of the ultrasonic beam generated by a diagnostic probe is happening in a saturation regime. The limiting values of the peak positive pressure at the focus are 20 MPa and 10 MPa for 64 and 32 active elements, correspondingly. Peak negative pressures p_- are not become at a constant level and decrease monotonically in the entire voltage range. The minimum values of p_- in the fields of diagnostic probe are achieved in the case of 128 active elements and reachs -10 MPa.

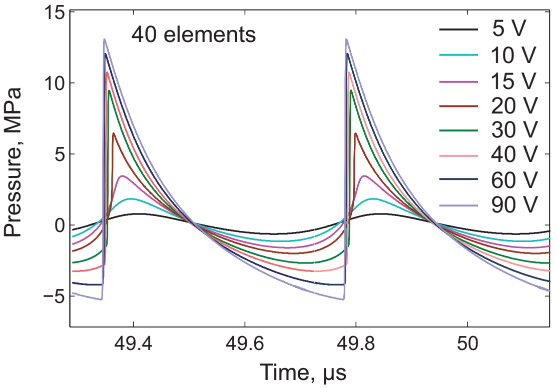

Figure 4.21: Waveforms at the focus of the probe ($z = 50$ mm) obtained in numerical simulations for 40 active elements of the probe.

The evolution of waveforms with the increasing of applied voltage is shown in Fig. 4.21 at a distance z = 50 mm for 40 active elements configuration. It is clearly seen how initially harmonic wave (profile at 5 V) distorts with increasing of its amplitude and finally turns into a sawtooth wave with the shock front (profile at 90 V). Note that changes in waveforms in the saturation regime are minimal (profiles at 60 V and 90 V in the figure).

Measurements of pressure waveforms in a large volume of space with fine spatial step is time consuming process. Numerical modeling has allowed to investigate in detail the spatial structure of the nonlinear ultrasonic field of the diagnostic probe with a spatial step of 5 times smaller than the size of the hydrophone. Simulations were performed for the entire range of the voltage applied to the probe. Let one first consider the results of the nonlinear simulation of peak pressure distribution along the z-axis at different number of active elements (Fig. 4.22). In the case of 16 active elements the beam is narrow in the direction of x-axis, its focusing occurs less efficient than in use of a larger number of active elements. Levels of the peak pressures at $z = 50$ mm differ from ones in intra-focal maximum not more than 2 times. When one uses 40 active elements it is necessary to take into account a significant shift of the maximum of the peak pressure from the supposed focal depth $z = 50$ mm. The shift of the maximum of peak positive pressure first occurs away from the probe and then towards to the probe, the shift of the focal area at voltage level of 90 V is about 1 cm. Similar effect is discussed in chapter 3 (§3.4) when focusing of pulsed fields was considered. Also in chapter 3 (§3.4) the possibility of observing the sharp and narrow peaks in the distribution of the p_+ in the prefocal area of the periodic field was discussed. In the field of a diagnostic probe this feature was observed in the case of 40 active elements in saturation regime of p_+ (shown in inset of Fig. 4.22). Minimum of the peak negative pressure p_- is displaced with pressure amplitude increase toward to the probe. If all 128 elements are active, the focusing occurs almost exactly at the focus $z = 50$ mm.

Consider how a field spatial structure of the peak pressures in the xz plane of electronic focusing is changed with an applied voltage. Fig. 4.23 shows the two-dimensional distributions of p_+ and p_- in the plane of the electronic focusing in the case of 40 active elements of the probe. The first column shows the distributions corresponding to the quasi linear regime (15 V) when waveform is not greatly distorted (see Fig. 4.21) and a shock front is not formed. Distributions of

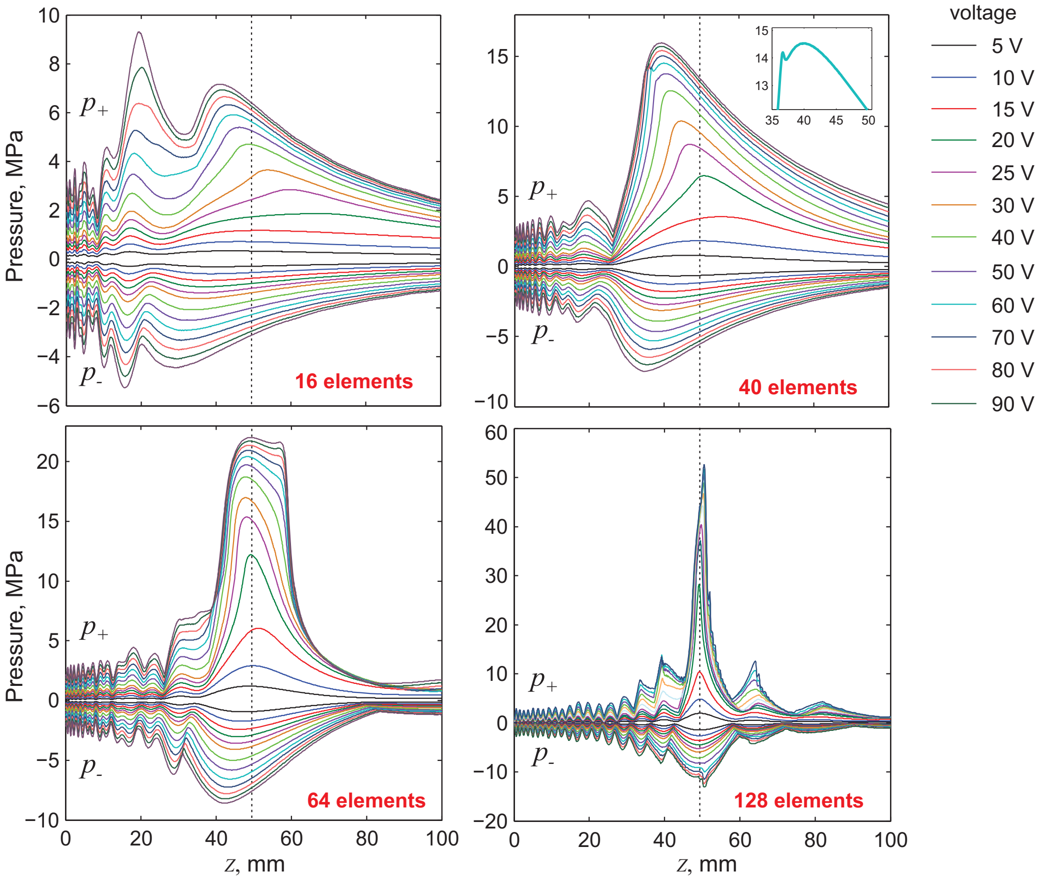

Figure 4.22: Distributions of peak pressures along the z-axis of the beam obtained in numerical simulations for different number of active elements.

peak pressures p_+ and p_- in this case are similar in structure but the focal area of p_+ has greater length along the z-axis and located farther than the focal area of p_-. The second column shows the distribution in the nonlinear regime (30 V) when the waveform contains a shock front (see Fig. 4.21). Distributions in the last column correspond to the saturation regime of the p_+ (80 V). With increase of applied voltage, the focal area of p_+ becomes smaller in size but remaining highly elongated along the z-axis of the probe. Interestingly that there are no fundamental changes in distributions of p_- with an increase of applied voltage, only pressure levels are increased and a small displacement (about 2-3 mm) of the focal area of p_- is occurred toward to the probe.

Comparison of two-dimensional distributions of the peak positive p_+ and peak negative p_- pressures in a saturation regime is demonstrated in Fig. 4.24 for configurations from 16, 40, and 128 active elements. It is clearly seen that the focal area of p_+ dramatically reduces in the xz plane with an increase of a number of active elements. In the case of 128 active elements the size of the focal area of p_+ along the x-axis is only 50 μm, which is 2 times smaller than the diameter of the FOPH tip (100 μm). Such a small size of the focal area and a sharp pressure gradient out of its boarder have led to significant differences (35 %) between the profiles measured by a hydrophone and calculated numerically (see Fig. 4.20, case of 128 active elements and Fig. 4.19). Significant changes with an increase in the number of active elements occur also in the yz plane of focusing of the beam by acoustic lens. The size of the focal region dramatically reduced along the z-axis but remained almost unchanged along y-axis. As a general conclusion one can say that using a greater

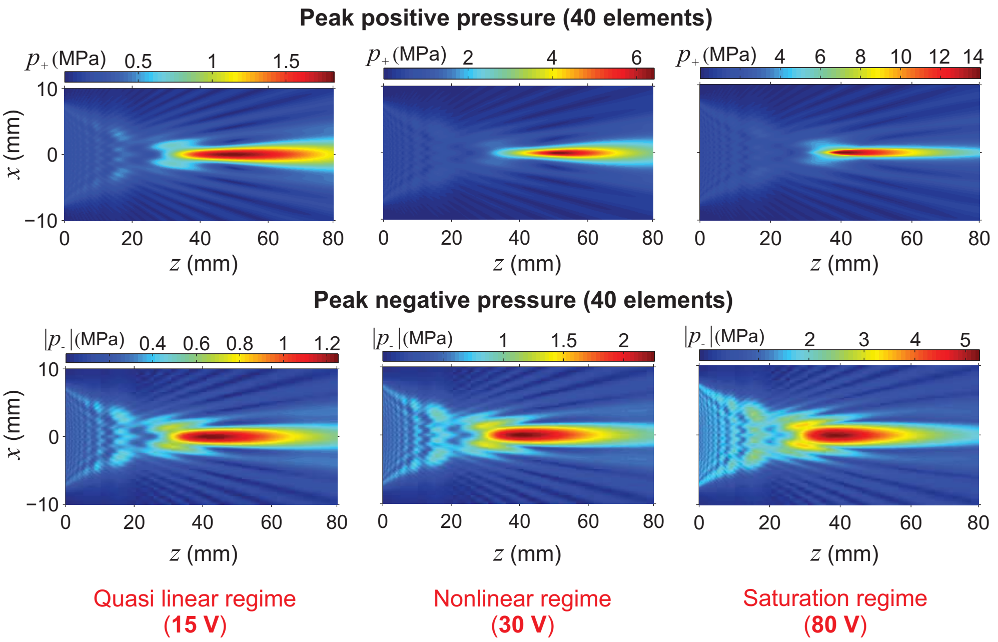

Figure 4.23: Comparison of 2D spatial distributions of the peak positive and peak negative pressures in the xz plane of electronical focusing at different values of applied voltages in the case of 40 active elements.

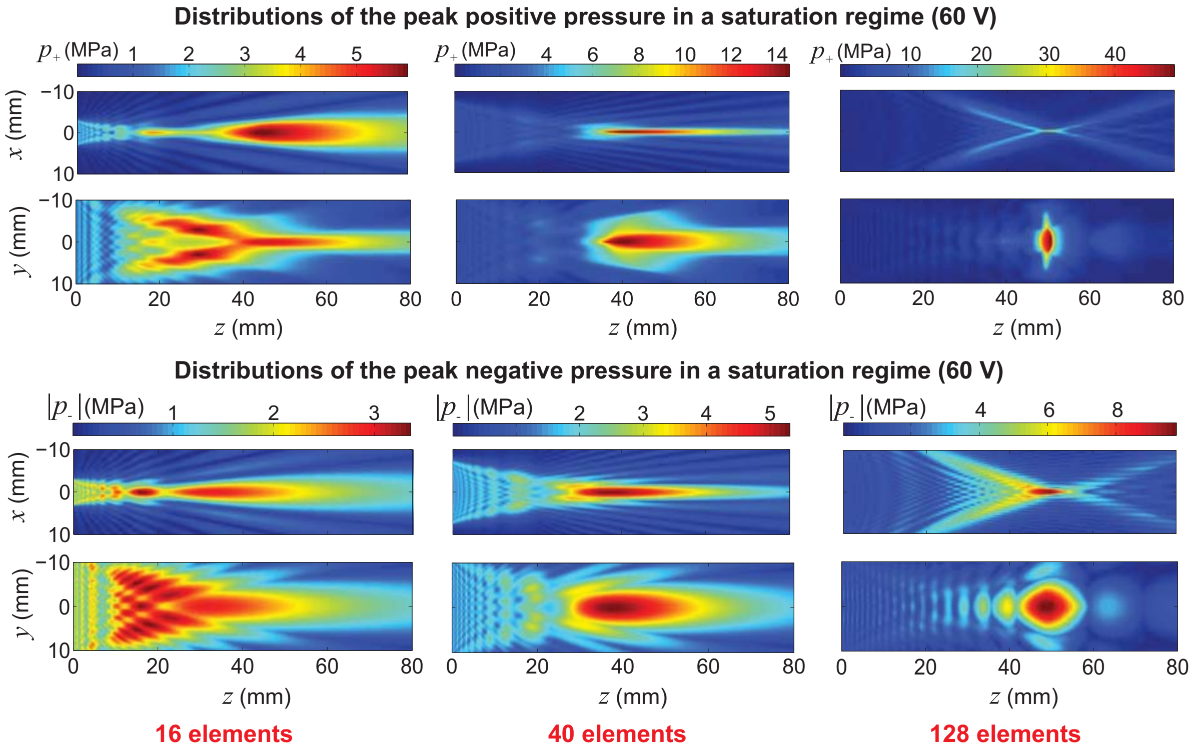

Figure 4.24: Comparison of 2D spatial distributions of the peak positive and peak negative pressures in a saturation regime at applied voltage of 60 V for configuration of 16, 40, and 128 active elements of the probe.

number of active elements in a saturation regime lead to shift of focal areas of peak positive and negative pressures away from the probe, reducing of their sizes and increasing of peak pressure levels.

§4.4 Conclusions

Nonlinear effects in fields of ESWT and diagnostic-type medical transducers were studied both theoretically and experimentally. It was shown that in the ESWT field the shock front formation did not occur for the currently machine settings. A true shock formation could be reached if the maximum initial pressure output of the device is doubled. In the field of diagnostic ultrasound probe nonlinear saturation effect of peak pressures was observed. Formation of the shock front occurs at levels of acoustic pressure about one third of those used in clinical experiments for pushing kidney stones by ultrasound radiation force.

Appendix A

Numerical calculation of the inverse Abel transform from the light intensity pattern in the schlieren image

In chapter 1 the method for reconstruction of dimensionless pressure waveforms from the light intensity pattern in the schlieren image was proposed. Here consider the numerical calculation of the integral $\int\limits_r^{+\infty} d/dx \left(\int\limits_x^{+\infty} I(r')dr' \right) dx/\sqrt{x^2 - r^2}$ in Eq. (1.8), which is used to reconstruct the dimensionless waveform from the schlieren image. Inner integral $A(x) = \int\limits_x^{+\infty} I(r')dr'$ is calculated using trapezoidal numerical integration while the outer integral contains a singularity at $x \to r$ and could not be calculated in this way. To avoid singularity, the integrand is approximated using a cubic spline interpolation and then calculated numerically.

Note that the investigated integral multiplied by the factor $(-1/\pi)$ is the Abel inversion transform that is written in general form as (Bracewell, reprint 2000)

$$B(r) = -\frac{1}{\pi} \int\limits_r^{+\infty} \frac{dA}{dx} \frac{dx}{\sqrt{x^2 - r^2}}. \tag{A.1}$$

One uses the next property of this inversion:

$$A = \int\limits_x^{+\infty} \frac{2rBdr}{\sqrt{r^2 - x^2}} = -2 \int\limits_x^{+\infty} \sqrt{r^2 - x^2} \frac{dB}{dr} dr. \tag{A.2}$$

Calculating the derivative, one finds $dA/dx = 2 \int\limits_x^{+\infty} \frac{dB}{dr} x dr / \sqrt{r^2 - x^2}$. It follows that $(dA/dx)|_{x=0} = 0$.

Let us approximate $A(x)$ using cubic spline interpolation:

$$A(x) = a_n + b_n(x - x_n) + c_n(x - x_n)^2 + d_n(x - x_n)^3 = \alpha_n + \beta_n x + \gamma_n x^2 + \delta_n x^3 \tag{A.3}$$

and assume that the function $A(x)$ is given at the nodes of the uniform grid $x_n = \Delta \cdot n$, $n = 1...N$, where Δ is the mesh spacing.

First, consider calculation for $r = 0$:

$$B(r=0) = -\frac{1}{\pi}\int\limits_{0}^{+\infty} \frac{dA}{dx}\frac{dx}{x}. \tag{A.4}$$

Split the integral (A.4) for the sum of terms

$$B(r=0) = -\frac{1}{\pi}\int\limits_{0}^{\Delta} \frac{dA}{dx}\frac{dx}{x} - \frac{1}{\pi}\sum_{n=1}^{n=N-1}\int\limits_{n\cdot\Delta}^{(n+1)\cdot\Delta} \frac{dA}{dx}\frac{dx}{x}. \tag{A.5}$$

Substituting the cubic spline approximation (A.3) with $\beta_0 = 0$ (because $(dA/dx)|_{x=0} = 0$) in Eq. (A.4), one obtains

$$B(r=0) = -\frac{1}{\pi}(2\gamma_0\Delta + \frac{3}{2}\delta_0\Delta^2) - \frac{1}{\pi}\sum_{n=1}^{n=N-1}\left[\beta_n \ln(\frac{b}{a}) + 2\gamma_n(b-a) + \frac{3}{2}\delta_n(b^2 - a^2)\right],$$
$$a = n\cdot\Delta, b = (n+1)\cdot\Delta. \tag{A.6}$$

Second, consider calculation for $r = m\cdot\Delta, m = 1...N-1$. Let $A(x = N\cdot\Delta) = 0$ because $A(x) \to 0$ if $x \to \infty$. Replace the integral by the sum of integrals over the segments:

$$B(r = m\cdot\Delta) = -\frac{1}{\pi}\sum_{n=m}^{n=N-1}\int\limits_{n\cdot\Delta}^{(n+1)\cdot\Delta} \frac{dA}{dx}\frac{dx}{\sqrt{x^2 - r^2}}. \tag{A.7}$$

Using cubic spline approximation (A.3) for every segment, one obtains

$$B(r = m\cdot\Delta) = -\frac{1}{\pi}\sum_{n=1}^{n=N-1} I_n,\ where\ I_n = \beta_n(b' - a') + 2\gamma_n c\,[sh(b') - sh(a')] +$$
$$+\frac{3c^2\delta_n}{2}(b' - a' + \frac{1}{2}\,[sh(2b') - sh(2a')]), a' = arch(\frac{a}{c}), b' = arch(\frac{b}{c}), c = m\cdot\Delta. \tag{A.8}$$

Thus, using Eqs. (A.6) and (A.8) it is possible to calculate the Abel inversion transform (A.1) numerically by summing the results for each segment. However, the light intensity I is equal to zero for distances x beyond the location of the pulse and therefore numerical integration requires a finite window. In numerical simulations, the size of spatial window was equal to the size of the schlieren image and the spatial step was 8 μs.

Appendix B

Synthèse des résultats

Dans l'introduction nous présentons l'actualité du sujet de la thèse qui porte sur l'étude de la focalisation nonlinéaire et de la réflexion d'ondes de choc acoustiques. Dans le contexte des applications aux ultrasons médicaux et à l'aéroacoustique l'état de l'art à ce jour des questions scientifiques est exposé ainsi que les objectifs généraux. Ci-après nous résumons les travaux et les principaux résultats obtenus.

Le premier chapitre est consacré à la mise en oeuvre des méthodes optiques pour la mesure de profils de pression acoustique dans le cas d'une onde en N générée par une source d'étincelle dans l'air. Dans le §1.1 un examen des méthodes existantes pour mesurer les ondes de choc acoustiques est présenté et les limites de la mesure par des microphones à condensateur sont discutés. Les méthodes optiques proposées comme une alternative pour les mesures d'impulsions de choc acoustiques sont l'ombroscopie schlieren et l'interferométrie. Dans le §1.2 le dispositif expérimental conçu pour les mesures schlieren d'ondes acoustiques générées par une source à étincelles en milieu homogène est présenté. Une procédure de reconstruction des formes d'onde de pression acoustique à partir d'images schlieren est décrite dans le §1.3. Les formes d'onde de pression ont été reconstruites à l'aide d'une méthode d'inversion de type Abel, à partir des cartes d'intensité lumineuse enregistrées avec une caméra haute résolution et rapide. Les niveaux de pression absolue ont été déterminés par une analyse à différentes de distances de propagation de la durée de la phase de compression d'impulsions, qui est modifiée en raison des effets de propagation non linéaire. Des exemples des signatures de pression reconstruites à différentes distances de la source sont présentés dans le §1.4. Notons que la résolution temporelle de la méthode (3 μs) est limitée par la durée d'exposition de la caméra à grande vitesse. Une autre méthode optique proposée dans la thèse pour les mesures de forme sphérique divergeante d'onde en N est basée sur la technique d'interférométrie Mach-Zehnder. Le dispositif expérimental est décrit dans le §1.5. Dans le §1.6 la méthode de reconstruction pour restaurer des formes d'onde de pression à partir de signaux de phase optique est décrite. La reconstruction est basée sur une inversion de type Abel. Contrairement à la méthode optique de strioscopie, la méthode de Mach-Zehnder permet la reconstruction quantitative des formes d'ondes de pression d'onde en N et, par conséquent, on dispose ainsi d'un "microphone laser" à large bande. Les résultats des mesures optiques obtenues à l'aide de l'interféromètre de Mach-Zehnder sont données dans le §1.7. La résolution temporelle de la méthode interféromètrique (0.4 μs) est principalement déterminée par la largeur finie du faisceau laser (environ 0.1 mm). Dans le §1.8 les avantages et les limites des deux méthodes optiques (méthode schlieren et la méthode de interférometrie Mach-Zehnder) pour les mesures des ondes de choc acoustiques dans l'air sont discutées.

Le deuxième chapitre de la thèse est consacré à l'étude expérimentale d'une réflexion irrégulière d'une onde en N sur une surface rigide . Dans le §2.1 nous présentons un examen des études théoriques et expérimentales existantes sur la réflexion d'onde de choc ainsi que sur la réflexion des chocs faibles avec le paradoxe de von Neumann. La classification des différents régimes de réflexion de faibles chocs acoustiques sur une surface rigide est donnée dans le §2.2. Une attention particulière est portée sur les différences entre la réflexion de "step-shock" et celle de formes d'onde plus complexes typiques des applications en acoustique. Dans le §2.3 le dispositif expérimental conçu pour la visualisation optique schlieren de la réflexion de l'onde de choc sur une surface rigide est présenté. Les images schlieren obtenues dans l'expérience sont analysées. Nous avons montré l'existence d'une réflexion irrégulière qui se traduit par un pied de Mach (Mach stem) dont la longueur évolue dynamiquement lorsque l'impulsion se propage le long de la surface. Le système optique schlieren permet une visualisation du motif de réflexion pour le choc avant de l'onde en N. La méthode de interferomètre de type Mach-Zehnder a été utilisé pour mesurer les formes d'onde de pression de l'onde en N proche de la surface réfléchissante. Dans le §2.4 les formes d'ondes de pression mesurées expérimentalement sont analysés. L'interaction non linéaire entre le choc avant réfléchi et le choc arrière incident de l'onde en N est discutée dans le §2.5. L'interaction conduit à la formation de pieds de Mach au-dessus de la surface où se croisent ces chocs et une zone de surpression est formée au-dessus de la surface.

Dans le troisième chapitre les mécanismes de saturation non linéaire des champs acoustiques focalisés d'ondes périodiques et des impulsions courtes sont considérés. Dans le §3.1 un examen des approches analytiques qui fournissent l'estimation des valeurs limites de pression positive maximale dans les faisceaux acoustiques périodiques et pulsés est détaillé. La possibilité d'observer la formation d'un pied de Mach dans la zone focale axiale est discutée. Dans le §3.2 un modèle numérique basé sur l'équation parabolique KZK est décrit. Le modèle a été utilisé pour caractériser des champs focalisés non linéaires de faisceaux acoustiques impulsionnels ou périodiques générés par une source de type piston et une source gaussienne. Dans le §3.3 l'effet de la signature temporelle du signal sur les valeurs limites de pressions crêtes est discuté. Nous avons montré que dans les faisceaux acoustiques périodiques les pressions crêtes positives sont plus élevées que celles réalisées dans des faisceaux pulsés. Le §3.4 est consacrée à étudier l'effet de répartition de la pression de la source sur la structure spatiale du faisceau ulstrasonore émis et les valeurs limites de pressions crêtes dans les champs acoustiques focalisés. Nous montrons que les sources gaussiennes sont plus appropriées pour atteindre les hautes pressions dans une zone focale de faible taille que les sources de type piston. L'analyse du §3.5 de l'interaction entre les fronts de choc des champs périodiques et pulsé focalisé à symétrie axiale montre qu'elle peut être considérée comme un procédé similaire à la réflexion de la surface rigide. Il est aussi démontré que l'équation KZK permet de décrire la formation d'un pied de Mach dans la zone focale pour une source de type piston. La structure des motifs des fronts d'onde dans la région focale du faisceau ressemble à celle de la réflexion de von Neumann comme le résultat d'une interaction entre le bord et la partie centrale de l'onde en provenance de la source ultrasonore.

Le quatrième chapitre est consacré à la caractérisation des champs acoustiques focalisés non linéaires de nouveaux dispositifs médicaux utilisés dans la thérapie par ondes de choc extracorporelle (ESWT) et dans les sondes ultrasonores de diagnostique. Dans le §4.1 un examen des perspectives d'utiliser l'ESWT pour plusieurs troubles musculo-squelettiques est présenté ainsi que les paramètres de dispositifs de ESWT. La mise en oeuvre d'une sonde de diagnostic utilisant la force de rayonnement d'une source ultrasonore focalisé pour déplacer les calculs rénaux du système de collecte urinaire est également discutée. La modélisation numérique est de nos jours un outil important pour la caractérisation des champs acoustiques de ces dispositifs médicaux. Dans le §4.2 les effets non linéaires dans le faisceau acoustique focalisé du dispositif électromagnétique Duolith SD1 de ESWT sont étudiés en combinant mesures et modélisations numériques. La condition limite pour la modélisation non linéaire avec l'équation KZK a été obtenue à partir de l'expérience en appliquant la méthode de la source équivalente. Ainsi notre procédé utilise des mesures pour obtenir des paramètres de source équivalente, à savoir la source avec le même champ acoustique sur l'axe du faisceau comme la vraie. Il a été montré que, dans les champs ESWT la formation choc ne se produit pas pour les paramètres d'utilisation actuelle de la machine. Une véritable formation de choc pourrait être atteinte si l'amplitude de pression initiale maximale du dispositif était doublée. Dans le §4.3 l'approche combinée mesure-modélisation a été utilisée pour caractériser le champ ultrasonore non linéaire de la sonde de diagnostic standard Philips C5-2 utilisé dans les expériences cliniques pour pousser les calculs rénaux. Les mesures ont été effectuées en deux étapes. La première était la mesure des formes d'ondes de pression de faible amplitude le long de l'axe de la sonde et dans son plan focal. Ces mesures ont été effectuées à faible puissance de sortie et ont été utilisées pour définir la condition limite introduite dans le modèle numérique. La seconde série de mesures a été effectuée à différents niveaux de sortie et a été réalisée pour comparaison avec les résultats des simulations non linéaires. Un modèle numérique 3D basé sur l'équation de Westervelt a été utilisé pour simuler le champ acoustique non linéaire générée dans l'eau par la sonde de diagnostic à des niveaux de sortie différents et pour un nombre différent d'éléments actifs dans la source ultrasonore. Il a été montré que la poussée des calculs rénaux se produit en régime de saturation. Dans le §4.4 les conclusions du quatrième chapitre sont donnés.

References

Almgren, M. 1986. Acoustic boundary layer influence on scale model simulation of sound propagation: Experimental verification. *J. Sound Vib.*, **110**, 247–259.

Averiyanov, M., Blanc-Benon, P., Cleveland, R. O., & Khokhlova, V. 2011a. Nonlinear and diffraction effects in propagation of N-waves in randomly inhomogeneous moving media. *J. Acoust. Soc. Am.*, **129**(4), 1760–1772.

Averiyanov, M., Ollivier, S, Khokhlova, V., & Blanc-Benon, P. 2011b. Random focusing of nonlinear acoustic N-waves in fully developed turbulence: Laboratory scale experiment. *J. Acoust. Soc. Am.*, **130**(6), 3595–3607.

Averkiou, M.A., & Cleveland, R.O. 1999. Modeling of an electrohydraulic lithotripter with the KZK equation. *J. Acoust. Soc. Am.*, **106**(1), 102–112.

Bacon, D.R. 1984. Finite amplitude distortion of the pulsed fields used in diagnostic ultrasound. *Ultrasound. Med. Biol.*, **10**(2), 189–195.

Bailey, M.R, Khokhlova, V.A., Sapozhnikov, O.A., Kargl, S.G., & Crum, L.A. 2003. Physical mechanisms of the therapeutic effect of ultrasound (A review). *Acoust. Phys.*, **49**(4), 369–388.

Bakhvalov, N.S., Zheleikin, Y.M., & Zabolotskaya, E.A. 1982. *Nonlinear Theory of Sound Beams*. Moscow: Nauka.

Baskar, S., Coulouvrat, F., & Marchiano, R. 2007. Nonlinear reflection of grazing acoustic shock waves: unsteady transition from von Neumann to Mach to Snell-Descartes reflections. *J. Fluid Mech.*, **575**, 27–55.

Ben-Dor, G. 1992. *Shock Wave Reflection Phenomena*. Springer Verlag, New York.

Bessonova, O., & Wilkens, V. 2013. Membrane hydrophone measurement and numerical simulation of HIFU fields up to developed shock regimes. *IEEE Transactions on Ultrasonics, Ferroelectrics, and Frequency Control*, **60**(2), 290–300.

Bessonova, O., Khokhlova, V., Bailey, M., Canney, M., & Crum, L. 2009. Focusing of high power ultrasound beams and limiting values of shock wave parameters. *Acoust. Phys.*, **55**(4), 463–473.

Bessonova, O.V. 2010. *Nonlinear effects in focused high-intensity ultrasound beams: numerical modeling and application in noninvasive surgery* ($inRussian$). Ph.D. thesis, Moscow.

Bessonova O.V., Khokhlova V.A., Bailey M.R., Canney M.S., & Crum L.A. 2009. Focusing of high power ultrasound beams and limiting values of shock wave parameters. *Acoust. Phys.*, **55**(4–5), 463–473.

Bessonova O.V., Khokhlova V.A., Bailey M.R., Canney M.S., & Crum L.A. 2010. A derating method for therapeutic applications of high intensity focused ultrasound. *Acoust. Phys.*, **56**(3), 354–363.

Birkhoff, G. 1950. *A Study in Logic. Fact and Similitude*. Princeton University Press.

Blanc-Benon, P., Ollivier, S., Attenborough, K., & Qin, Q. 2005. Laboratory experiments to study N-waves propagation: effects of turbulence and/or ground roughness. *Pages 651–654 of: 17^{th} International Symposium on Nonlinear Acoustics, Manchester, UK*, vol. 838.

Born, M., & Wolf, E. 1999. *Principles of Optics*. 7th ed., Cambridge University Press, Cambridge.

Bracewell, R. N. reprint 2000. *The Fourier Transform and Its Applications*. McGraw-Hill, New York, NY.

Brio, M., & Hunter, J.K. 1992. Mach reflection for the two-dimensional Burgers equation. *Physica D*, **60**, 194–207.

Brode, H. L. 1959. Blast wave from a spherical charge. *Phys. of Fluids*, **2**, 217–229.

Brown, K.E., Nickels, F.A., Caron, J.P., Mullineaux, D.R., & Clayton, H.M. 2005. Investigation of the immediate analgesic effects of extracorporeal shock wave therapy for treatment of navicular disease in horses. *Ultrasound Med. Biol.*, **34**, 554 Ű558.

Buchbinder, R., Ptasznik, R., Gordon, J., Buchanan, J., Prabaharan, V., & Forbes, A. 2002. Ultrasound guided extracorporeal shock wave therapy for plantar fasciitis. *JAMA*, **288**, 1364 Ű1372.

Canney, M.S., Bailey, M.R., Crum, L.A., Khokhlova, V.A., & Sapozhnikov, O.A. 2008. Acoustic characterization of high intensity focused ultrasound fields: A combined measurement and modeling approach. *J. Acoust. Soc. Am.*, **124**(4), 2406–2420.

Cleveland, R.O., & McAteer, J.A. 2012. *Physics of Shock-Wave Lithotripsy*. in Smith's Textbook of Endourology, Volume I&II, 3rd Edition (eds A. D. Smith, G. H. Badlani, G. M. Preminger and L. R. Kavoussi), Wiley-Blackwell, Oxford, UK.

Cleveland, R.O., Chitnis, P.V., & McClure, S.R. 2007. Acoustic field of a ballistic shock wave therapy device. *Ultrasound Med. Biol.*, **33**, 1327–1335.

Colella, P., & Henderson, L.F. 1990. The von Neumann paradox for the diffraction of weak shock waves. *J. Fluid Mech.*, **213**, 71–94.

Cowan, G.R., & Hornig, D.F. 1950. The experimental determination of the thickness of a shock front in a gas. *J. Chem. Phys.*, **18**, 1008–1018.

Davy, B. A., & Blackstock, D. T. 1971. Measurements of the refraction and diffraction of a short N-wave by a gas-filled soap bubble. *J. Acoust. Soc. Am.*, **49**(3B), 732–737.

DuMond, J.W.M., Cohen, E.R., Panofsky, W.K.H., & Deeds, E. 1946. A determination of the waveforms and laws of propagation and dissipation of ballistic shock waves. *J. Acoust. Soc. Am.*, **18**, 97–118.

Elmer, K.R., & Joshi, M.C. 1994. Varability of measured sonic boom signatures: volume 1 - technical report. *NASA Contracor Report 191483*, **1**.

Endres, S., Weiskirch, M., Hinz, C., Hütter, F., & Wilke, A. 2008. Extracorporeal shock-wave therapy in the treatment of pseudoarthrosis: a case report. *Cases J.*, **1**, 276.

Fidell, S., Silvati, L., & Pearsons, K. 2002. Relative rates of growth of annoyance of impulsive and non-impulsive noises. *J. Acoust. Soc. Am.*, **111**(1), 576–585.

Filonenko, E.A., & Khokhlova, V.A. 2001. Effect of Acoustic Nonlinearity on Heating of Biological Tissue by High-Intensity Focused Ultrasound. *Acoust. Phys.*, **47**(4), 468–475.

Furia, J.P. 2005. Safety and efficacy of extracorporeal shock wave therapy for chronic lateral epicondylitis. *Am. J. Orthop. (Belle Mead, NJ)*, **34**, 13–19.

Gerdesmeyer, L., Wagenpfeil, S., Haake, M., Maier, M., Loew, M., Wörtler, K., Lampe, R., Seil, R., Handle, G., Gassel, S., & Rompe, J.D. 2003. Extracorporeal shock wave therapy for the treatment of chronic calcifying tendonitis of the rotator cuff: a randomized controlled trial. *JAMA-J. Am. Med. Assoc.*, **290**, 2573–2580.

Graeme, J. 1996. *Photodiode Amplifiers: OP AMP Solutions*. 1st ed. McGraw-Hill, New York.

Greene, E.F., Cowan, G.R., & Hornig, D.F. 1951. The thickness of shock fronts in argon and nitrogen and rotational heat capacity lags. *J. Chem. Phys.*, **19**, 427–434.

Grillon, V., Meynial, X., & Polack, J.D. 1996. What can auralisation in small scale models achieve. *Acta Acust.*, **82**, 362–364.

Guderley, K. G. 1962. *The Theory of Transonic Flow*. Pergamon.

Haake, M., König, I.R., Decker, T., Riedel, C., Buch, M., Müller, H.H., Vogel, M., Auersperg, V., Maier-Boerries, O., Betthäuser, A., Fischer, J., Loew, M., Müller, I., Rehak, H.C., Gerdesmeyer, L., Maier, M., & Kanovsky, W. 2002. Extracorporeal shock wave therapy in the treatment of lateral epicondylitis: A randomized multicenter trial. *J. Bone Joint Surg. Am.*, **84**, 1982–1991.

Hamilton, M.F., & Blackstock, D.T. 1998. *Nonlinear Acoustics*. Academic, San Diego.

Hamilton, M.F., Rudenko, O.V., & Khokhlova, V.A. 1997. A new method for calculating the paraxial region of intense acoustic beams. *Acoust. Phys.*, **43**(1), 48–53.

Hickey, Hannah. January 10, 2014. Trial to test using ultrasound to move kidney stones. *News and Information about University of Washington*.

Hill, C., Bamber, J., & Haar, G. T. 2002. *Physical principles of medical ultrasonics*. 2nd edn. Wiley.

Hirschberg, A., Gilbert, J., Msallam, R., & Wijnands, A.P.J. 1996. Shock waves in trombones. *J. Acoust. Soc. Am.*, **99**(3), 1754–1758.

Ito, K., Fukumoto, Y., & Shimokawa, H. 2009. Extracorporeal Shock Wave Therapy as a New and Non-invasive Angiogenic Strategy. *Tohoku J. Exp. Med.*, **219**, 1–9.

Karzova, M., Khokhlova, V.A., Perez, C., & Matula, T.J. 2013. Temporal and spatial characteristics of nonlinear acoustic field generated by an extracorporeal shockwave therapy device: modeling and measurements. *POMA*, **19**, 075100 (5 pages).

Karzova, M., Cunitz, B., Yuldashev, P., Andriyakhina, Y., Kreider, W., Sapozhnikov, O., Bailey, M., & Khokhlova, V. 2015a. Nonlinear effects in ultrasound fields of diagnostic-type transducers used for kidney stone propulsion: Characterization in water. *AIP Conf. Proc.*, **1685**, 040002.

Karzova, M., Yuldashev, P., Ollivier, S., Khokhlova, V., & Blanc-Benon, Ph. 2015b. Nonlinear reflection of a spherically divergent N-wave from a plane surface: Optical interferometry measurements in air. *AIP Conf. Proc.*, **1685**, 090011.

Karzova, M.M., Averianov, M.V., Sapozhnikov, O.A., & Khokhlova, V.A. 2012. Mechanisms for saturation of nonlinear pulsed and periodic signals in focused acoustic beams. *Acoust. Phys.*, **58**(1), 81–89.

Karzova, M.M., Yuldashev, P.V., Khokhlova, V.A., Ollivier, S., & Blanc-Benon, Ph. 2015c. Application of a Mach–Zehnder interferometer to the observation of Mach stem formation when a shock wave is reflected from a rigid surface. *Bulletin of the Russian Academy of Sciences. Physics*, **79**(10), 1293–1295.

Karzova, M.M., Yuldashev, P.V., Khokhlova, V.A., Ollivier, S., Salze, E., & Blanc-Benon, Ph. 2015d. Characterization of spark-generated N-waves in air using an optical schlieren method. *J. Acoust. Soc. Am.*, **137**(6), 3244–3252.

Karzova, M.M., Khokhlova, V.A., Salze, E., Ollivier, S., & Blanc-Benon, Ph. 2015e. Mach stem formation in reflection and focusing of weak shock acoustic pulses. *J. Acoust. Soc. Am.*, **137**(6), EL436–EL442.

Khokhlova, V.A., Souchon, R., Tavakkoli, J., Sapozhnikov, O.A., & Cathignol, D. 2001. Numerical modeling of finite amplitude sound beams: Shock formation in the near field of a cw plane piston source. *J. Acoust. Soc. Am.*, **110**(1), 95–108.

Khokhlova, V.A., Bessonova, O.V., Canney, M.S., Bailey, M.R., & Crum, L.A. 2006. Spatial distributions of acoustic parameters in high-intensity focused ultrasound fields. *J. Acoust. Soc. Am.*, **120**(5(2)), 3194.

Krehl, P., & van der Geest, M. 1991. The discovery of the Mach reflection effect and its demonstration in an auditorium. *Shock Waves*, **1**(1), 3–15.

Kreider, W., Yuldashev, P.V., Sapozhnikov, O.A., Farr, N., Partanen, A., Bailey, M.R., & Khokhlova, V.A. 2013. Characterization of a multi-element clinical HIFU system using acoustic holography and nonlinear modeling. *IEEE Transactions on Ultrasonics, Ferroelectrics, and Frequency Control*, **60**(8), 1683–1698.

Kudo, P., Dainty, K., Clarfield, M., Coughlin, L., Lavoie, P., & Lebrun, C. 2006. Randomized, placebo-controlled, double-blind clinical trial evaluating the treatment of plantar fasciitis with an extracoporeal shock wave therapy (ESWT) device: a North American confirmatory study. *J. Orthop. Res.*, **24**, 115–123.

Kulkarny, V. 1975. *An experimental investigation on focussing of weak shock waves in air*. Ph.D. thesis, California Institute of Technology.

Kurganov, K., & Tandmor, E. 2000. New high-resolution central schemes for nonlinear conservation laws and convention-diffusion equations. *J. Comp. Phys.*, **160**, 241–282.

Leatherwood, J.D., & Sullivan, B.M. 1992. Subjective loudness response to simulated sonic booms. *Pages 151–170 of: High-Speed Research: Sonic Boom, (SEE N92-33874 24-05)*, vol. 1.

Lee, R.A., & Downing, J.M. 1991. Sonic Boom produced by United states Navy aircraft: measured data, AL-TR-1991-0099. *Biodynamic Environment Branch, Biodynamics and Bioengenineering Division, Armstrong Laboratory,Wright-Patterson Air Force Base, Ohio*.

Lipkens, B. 2002. Model experiment to study sonic boom propagation through turbulence. Part III: Validation of sonic boom propagation models. *J. Acoust. Soc. Am.*, **111**(1 Pt.2), 509–519.

Lipkens, B., & Blackstock, D.T. 1998a. Model experiment to study sonic boom propagation through turbulence. Part I: Model experiment and general results. *J. Acoust. Soc. Am.*, **103**(1), 148–158.

Lipkens, B., & Blackstock, D.T. 1998b. Model experiment to study sonic boom propagation through turbulence. Part II: Effect of turbulence intensity and propagation distance through turbulence. *J. Acoust. Soc. Am.*, **104**(3 Pt.1), 1301–1309.

Loubeau, A., Sparrow, V.W., Pater, L.L., & Wright, W.M. 2006. High-frequency measurements of blast wave propagation. *J. Acoust. Soc. Am.*, **120**(3), EL29–EL35.

Mach, E. 1878. *Über den Verlauf von Funkenwellen in der Ebene und im Raume*. Sitzungsbr. Akad. Wiss. Wien 78, 819-838.

Mach, E., & Salcher, P. 1887. Photographische fixierung der dunch projectile in der luft eingeleiteten Vorgänge. *Sitzungsb. Akad. Wiss. Wien*, **95**, 764–780.

Maglieri, D.J., Sotchcott, V.E., & Keefer, T.N. 1992. A summary of XB-70 sonic boom signature data for flights during March 1965 through May 1966. *NASA Contracor Report 189630*.

Marchiano, R., Baskar, S., Coulouvrat, F., & Thomas, J.-L. 2007. Experimental evidence of deviation from mirror reflection for acoustical shock waves. *Phys. Rev.*, **E 76**, 056602.

Merzkirch, W. 1974. *Flow visualization*. Academic Press, New York and London.

Mizukaki, T. 2010. Application of digital phase-shift holographic interferometry to weak shock waves propagating at Mach 1.007. *Shock Waves*, **20**, 19–27.

Musatov, A.G., & Sapozhnikov, O.A. 1993a. Focusing of powerful acoustic pulses at different convergence angles on the initial wave front. *Acoust. Phys.*, **39**(2), 166–169.

Musatov, A.G., & Sapozhnikov, O.A. 1993b. Nonlinear effects in process of focusing of acoustic pulses with shock front. *Acoust. Phys.*, **39**(3), 266–269.

Musatov, A.G., Rudenko, O.V., & Sapozhnikov, O.A. 1992. Nonlinear refraction and absorption phenomena due to powerful pulses focusing. *Acoust. Phys.*, **38**(3), 502–510.

Naugolnykh K.A., & Romanenko E.V. 1959. The dependence of the gain of the acoustic focusing system of ultrasonic intensity. *Akusticheskij Zhurnal (in Russian)*, **5**(2), 191–195.

Neumann, J. Von. 1974. *Oblique reflection of shocks*. in John von Neumann Collected Work, edited by A.H. Taub (MacMillan, New York, 1963), vol. 6, pp. 238-299.

Ohtori, S., Inoue, G., Mannoji, C., Saisu, T., Takahashi, K., Mitsuhashi, S., Wada, Y., Takahashi, K., Yamagata, M., & Moriya, H. 2001. Shock wave application to rat skin induces degeneration and reinnervation of sensory nerve fibers. *Neurosci Lett*, **315**, 57–60.

Ollivier, S., Desjouy, C., Yuldashev, P.Y., Koumela, A., Salze, E., Karzova, M., Rufer, L., & Blanc-Benon, Ph. 2015. High frequency calibration of MEMS microphones using spherical N-waves. *AIP Conf. Proc.*, **1685**, 030011.

Orenstein, L. 1982. The rise time of N-waves produced by sparks. *Technical Report, Appl. Res. Lab., Univ. Texas Austin*, ARL–TR–82–51.

Osman, M.M., Alfano, Y., & Kamp, S. 2005. et al, 5-year-follow-up of patients with clinically insignificant residual fragments after extracorporeal shockwave lithotripsy. *Eur Urol.*, **57**(6), 860–864.

Ostrovskii, L.A., & Sutin, A.M. 1975. Focusing of acoustic waves of a finite amplitude. *Sov. Phys. Dokl.*, **20**, 275–277.

Panda, J. 1995. Wide angle light scattering in shock-laser interaction. *AIAA Journal*, **33**, 2429–2431.

Panda, J., & Adamovsky, G. 1995. Laser light scattering by shock waves. *Phys. Fluids*, **7**, 2271–2279.

Perez, C., Chen, H., Matula, T.J., Karzova, M.M., & Khokhlova, V.A. 2013. Acoustic field characterization of the Duolith: Measurements and modeling of a clinical shockwave therapy device. *J. Acoust. Soc. Am.*, **134**(2), 1663–1674.

Perez C. 2015. *Characterizing ultrasound pressure fields, microbubbles and their interaction*. Ph.D. thesis, Center for Industrial and Medical Ultrasound (CIMU), Applied Physics Lab, University of Washington.

Picaut, J., & Simon, L. 2001. A scale model experiment for the study of sound propagation in urban areas. *Appl. Acoust.*, **62**(3), 327–340.

Picaut, J., Pollès, T. Le, L'Hermite, P., & Gary, V. 2005. Experimental study of sound propagation in a street. *Appl. Acoust.*, **66**(2), 149–173.

Pierce, A. D. 1981. *Acoustics: an introduction to its physical principles and applications*. New York: McGraw-Hill Book Co.

Plotkin, K. J. 2002. State of the art of sonic boom modeling. *J. Acoust. Soc. Am.*, **111**(1), 530–536.

Qin, Q., & Attenborough, K. 2004. Characteristics and application of laser-generated acoustic shock waves in air. *Appl. Acoust.*, **65**(4), 325–340.

Reed, J. W. 1977. Atmospheric attenuation of explosion waves. *J. Acoust. Soc. Am.*, **61**, 39–47.

Rompe, J.D. 2004. Repetitive low-energy shock wave treatment for chronic lateral epicondylitis in tennis players. *Am. J. Sports Med.*, **32**, 734–743.

Rompe, J.D., Decking, J., Schoellner, C., & Nafe, B. 2003. Shock wave application for chronic plantar fasciitis in running athletes: a prospective, randomized, placebo-controlled trial. *Am. J. Sports Med.*, **31**, 268–275.

Rosnitskiy, P.B., P.V., Yuldashev, & V.A., Khokhlova. 2015. Effect of the angular aperture of medical ultrasound transducers on the parameters of nonlinear ultrasound field with shocks at the focus. *Acoust. Phys.*, **61**(3), 301–307.

Rudenko, O. V. 1995. Nonlinear sawtooth-shaped waves. *Phys. Usp.*, **38**, 965Ű–989.

Rudenko, O. V., & Soluyan, S. I. 1977. *Theoretical foundations of nonlinear acoustics*. New York: Consultants Bureau.

Rudenko, O.V. 2007. Nonlinear waves: some biomedical applications. *Physics-Uspekhi*, **50**(4), 359–367.

Rudenko, O.V., & Sapozhnikov, O.A. 2004. Self-action effects for wave beams containing shock fronts. *Physics-Uspekhi*, **47**(9), 907–922.

Salze, E., Yuldashev, P., Ollivier, S., Khokhlova, V., & Blanc-Benon, Ph. 2014. Laboratory-scale experiment to study nonlinear N-wave distortion by thermal turbulence. *J. Acoust. Soc. Am.*, **136**(2), 556–566.

Sapozhnikov, O.A. 1991. Focusing of powerful acoustic pulses. *Acoust. Phys.*, **37**(4), 760–769.

Semenov, A. N., Berezkina, M. K., & Krassovskaya, I. V. 2012. Classification of pseudo-steady shock wave reflection types. *Shock Waves*, **22**, 307–316.

Settles, G. S. 2001. *Schlieren and shadowgraph techniques: visualizing phenomena in transparent media*. Springer-Verlag, Heidelberg.

Shah, A., Owen, N., Lu, W., Cunitz, B., Kaczkowski, P., Harper, J., Bailey, M., & Crum, L. 2010. Novel ultrasound method to reposition kidney stones. *Urological Research*, **38**(6), 491–495.

Shah, A., Harper, J., Cunitz, B., Wang, Y.-N., Paun, M., Simon, J., Lu, W., Kaczkowski, P., & Bailey, M. 2012. Focused ultrasound to expel calculi from the kidney. *The Journal of Urology*, **187**, 739–743.

Shooter, J.A., Muir, T.G., & Blackstock, D.T. 1974. Acoustic saturation of spherical waves in water. *J. Acoust. Soc. Am.*, **55**(1), 54–62.

Skews, B., & Ashworth, J. 2005. The physical nature of weak shock wave reflection. *J. Fluid Mech.*, **542**, 105–114.

Smeets, G. 1977. Laser interference microphone for ultrasonics and nonlinear acoustics. *J. Acoust. Soc. Am.*, **61**(3), 872–875.

Steinberg, J. July 2006. ESWT role in Wound care. *Podiatry today*, 63–67.

Tabak, E.G., & Rosales, R.R. 1994. Focusing of weak shocks waves and the von Neumann paradox of oblique shock reflection. *Phys. Fluids*, **6**, 1874–1892.

Tesdall, A. M., & Hunter, J. K. 2002. Self-similar solutions for weak shock reflection. *J. Appl. Maths*, **63**, 42–61.

Uizem, J. 1977. *Linear and nonlinear waves*. Moscow, Mir.

Vasil'ev, A.A. 1964. *Shadow Methods*. Moscow: Nauka Press.

Vasil’ev, E., & Kraiko, A. 1999. Numerical simulation of weak shock diffraction over a wedge under the von Neumann paradox conditions. *Comput. Math. Phys.*, **39**, 1335–1345.

Vinogradova, M. B., Rudenko, O. V., & Suhorukov, A. P. 1979. *Teorija voln*. Nauka.

Wang, C.J. 2003. An overview of shock wave therapy in musculoskeletal disorders. *Chang Gung Med. J.*, **26**, 220–232.

Westervelt, P.J. 1963. Parametric Acoustic Array. *J. Acoust. Soc. Am.*, **35**(4), 535–537.

Willshire, Jr. W. L., & Devilbiss, D.W. 1992. Preliminary results from the White Sands Missle Range sonic boom. *High-speed research: sonic boom*, **1**, 137–149.

Wright, W.M. 1983. Propagation in air of N-waves produced by sparks. *J. Acoust. Soc. Am.*, **73**(6), 1948–1955.

Wright, W.M., & McKittrick, J.L. 1967. Diffraction of spark-produced acoustic impulses. *Am. J. Phys.*, **35**(2), 124–128.

Wright, W.M., & Medendorp, N.W. 1968. Acoustic radiation from a finite line source with N-wave excitation. *J. Acoust. Soc. Am.*, **43**(5), 966–971.

Yuldashev, P., Karzova, M., Khokhlova, V., Ollivier, S., & Blanc-Benon, Ph. 2015. Mach-Zehnder interferometry method for acoustic shock wave measurements in air and broadband calibration of microphones. *J. Acoust. Soc. Am.*, **137**(6), 3314–3324.

Yuldashev, P.V., Averiyanov, M.V., Khokhlova, V.A., Sapozhnikov, O.A., Ollivier, S., & Blanc-Benon, P. 2008a. Nonlinear propagation of spark-generated N-waves in atmosphere: theoretical and experimental assessment of the shock front structure. *Pages 565–570 of: Proc. of Acoustics’08 Paris Congress, Paris, 27 June–4 July, 2008*.

Yuldashev, P.V., Aver’yanov, M.V., Khokhlova, V.A., Ollivier, S., & Blanc-Benon, P. 2008b. Nonlinear spherically divergent shock waves propagating in a relaxing medium. *Acoust. Phys.*, **54**(1), 32–41.

Yuldashev, P.V., Averiyanov, M.A., Khokhlova, V.A., Sapozhnikov, O.A., Ollivier, S., & Blanc-Benon, P. 2010a. Measurement of shock N-waves using optical methods. *In: 10ème Congrès Français d’Acoustique, 12-16 avril, 2010, Lyon, CD-ROM*.

Yuldashev, P.V., Ollivier, S., Averiyanov, M.V., Sapozhnikov, O.A., Khokhlova, V.A., & Blanc-Benon, P. 2010b. Nonlinear propagation of spark-generated N-waves in air: modeling and measurements using acoustical and optical methods. *J. Acoust. Soc. Am.*, **128**(6), 3321–3333.

Yuldashev P. 2011. *Nonlinear shock waves propagation in random media with inhomogeneities distributed in space or concentrated in a thin layer*. Ph.D. thesis, Moscow.

Zakharian, A.R., Brio, M., Hunter, J.K., & Webb, G.M. 2000. The von Neumann paradox in weak shock reflection. *J. Fluid Mech.*, **442**, 193–205.

dernière page de la thèse

AUTORISATION DE SOUTENANCE

Vu les dispositions de l'arrêté du 7 août 2006,

Vu la demande des Directeurs de Thèse

Monsieur P. BLANC-BENON et Madame V. KHOKHLOVA

et les rapports de

Monsieur R. CLEVELAND
Professeur - Department of Engineering Science - Oxford University - Parks Road - Oxford OX1 3PJ
ROYAUME-UNI

Et de

Monsieur V. PREOBRAJENSKI
Professeur - Institut d'Electronique de Micro-électronique et de Nanotechnologie
IEMN DOAE UMR CNRS 8520 - Ecole centrale de Lille - BP 48 - 59655 VILLENEUVE D'ASCQ cedex

Madame KARZOVA Maria

est autorisée à soutenir une thèse pour l'obtention du grade de **DOCTEUR**

Ecole doctorale MECANIQUE, ENERGETIQUE, GENIE CIVIL ET ACOUTIQUE

Fait à Ecully, le 8 mars 2016

P/Le directeur de l'E.C.L.
La directrice des Etudes

Service Scolarité

M-A. GALLAND